

ALMA MATER STUDIORUM — UNIVERSITÀ DI BOLOGNA

---

DOTTORATO DI RICERCA IN SCIENZE CHIMICHE

---

— CICLO XXVII —

Settore Concorsuale di Afferenza: 03/B1

Settore Scientifico Disciplinare: CHIM/03

---

# Photophysics of Carbon Nanotubes: from Dispersion to Supramolecular Systems

---

Presentata da: Eleonora Pavoni

**Coordinatore:**

Prof. Aldo Roda

**Relatore:**

Prof. ssa Paola Ceroni

**Correlatore:**

Dott. Nicola Armaroli

Esame finale anno 2015



— *E nell'istante in cui seppe, cessò di sapere.* —

Jack London



# Contents

<b>Prefazione</b>	<b>VII</b>
<b>Abstract</b>	<b>1</b>
<b>Introduction</b>	<b>3</b>
<b>1 Carbon Nanotubes</b>	<b>7</b>
1.1 Structure and electronic properties . . . . .	8
1.2 Optical properties . . . . .	16
1.3 Production Techniques . . . . .	19
1.3.1 Arc Discharge . . . . .	20
1.3.2 Laser Ablation . . . . .	20
1.3.3 Chemical Vapour Deposition . . . . .	21
1.4 Covalent and Non-Covalent Functionalization on SWCNTs . .	22
1.4.1 Covalent Functionalization of SWCNTs . . . . .	23
1.4.2 Non-covalent functionalization of SWCNTs . . . . .	26
<b>2 Dispersion of SWCNTs using RAFT copolymers</b>	<b>33</b>
2.1 Synthesis of the polymers . . . . .	34
2.2 Making a dispersion of SWCNTs . . . . .	37
2.3 Spectroscopic investigation . . . . .	38
2.4 Atomic force microscopy study . . . . .	45
2.5 Conclusion . . . . .	47
<b>3 SWCNTs enriched in (7,6) chirality and OPV systems</b>	<b>49</b>
3.1 Synthesis of the OPV molecules and SWCNTs (7,6) function- alization . . . . .	50

---

3.2	Spectroscopic investigation . . . . .	54
3.2.1	Optical properties of SWCNTs enriched in (7,6) chirality	54
3.2.2	Photophysical Characterization of SWCNTs_OPV systems . . . . .	57
3.3	Conclusion . . . . .	62
<b>4</b>	<b>Hybrid systems based on porphyrin, fullerene and DWCNTs</b>	<b>65</b>
4.1	Synthesis of the starting materials and of the hybrid systems . . . . .	67
4.2	Photophysical studies . . . . .	69
4.3	Conclusion . . . . .	79
<b>5</b>	<b>Ru(II) complexes with extended phenanthroline-based ligands</b>	<b>83</b>
5.1	Synthesis of ligands and respective Ru(II) complexes . . . . .	85
5.2	Electrochemistry . . . . .	86
5.3	Photophysical characterization and theoretical study . . . . .	91
5.3.1	PT series . . . . .	91
5.3.2	NT series . . . . .	100
5.4	Conclusion . . . . .	107
<b>6</b>	<b>Instrumentation</b>	<b>109</b>
6.1	Steady state absorption and luminescence measurements . . . . .	109
6.2	Time resolved emission measurements . . . . .	110
6.3	Atomic force microscopy measurements . . . . .	110
	<b>Acknowledgement</b>	<b>123</b>
	<b>List of publication and Poster presentation</b>	<b>125</b>

# Prefazione

Come può la Chimica far conseguire il titolo di Dottore in Philosophia? È questa la domanda che mi sono posta quando ho iniziato la stesura della mia tesi. L'etimologia del termine mi ha aiutato. È philosophia l'amore per il sapere, per le scoperte e per la conoscenza. Tutte le materie si accomunano quando è la passione a spingerle, anche materie apparentemente molto distanti. E così, in questi anni, è stata per me quasi una rivelazione scoprire le connessioni, a volte perfino strette, che nel corso della storia hanno legato la produzione letteraria al mondo della chimica. Mondi solo all'apparenza diversi e lontani. E se ogni volta era sorprendente individuare nuovi autori, anche estranei al mondo scientifico, che invadevano lo spazio chimico e positivistico con le loro opere narrative, lo stupore presto mi abbandonava. Bastava infatti che mi soffermassi a riflettere sulla "magia" della chimica e sull'incanto della vita e sulla coincidenza delle due speculazioni, della passione che entrambe le guida. È comunque philosophia, amore per il sapere. E di cosa altro si occupano in fondo gli scrittori e gli scienziati? Ero ancora sui banchi delle scuole medie, quando conobbi Trainor, il farmacista di Spoon River, freddo mescolatore di elementi chimici, concentrato nelle sue combinazioni e dimentico del mondo circostante. Trainor "il chimico" che ritrovo nel mondo di De Andrè con tutte le sue insicurezze. Espertissimo nel manipolare gli elementi, i fluidi ed i solidi, eppure mai, dice l'autore, gli riuscì di comprendere come gli uomini si combinassero attraverso l'amore "*affidando ad un gioco la gioia e il dolore*".

D'obbligo è il ricordo di Galileo Galilei, più specificatamente legato ai metodi razionali, resta pur sempre un gigante anche per la sua produzione letteraria e sarà sempre ricordato nella sua doppia veste di scrittore e di immenso scienziato, tanto da essere citato come il creatore della prosa scientifica italiana. La scienza moderna ha senz'altro preso da lui la volontà

di cercare la verità con la sperimentazione, cercando e trovando di volta in volta le soluzioni non più solo dai libri. Esempio di indipendenza e libertà di pensiero, restio ad accettare dogmi ed imposizioni precostituite, almeno fino alla forzata abiura (riflesso dell'oscurantismo dei tempi) che però non riuscì a piegare del tutto il suo spirito e la valenza universale della sua rivoluzione culturale.

Con un singolare salto temporale ripenso a Lucrezio, che duemila anni fa, ha affrontato il tema ragione/scienza con una potenza laicamente moderna e innovatrice e con una convergenza assoluta tra poesia e pensiero scientifico. Non è sbagliato affermare che per certi spunti è riuscito ad anticipare ed influenzare teorie e scoperte future svelando agli uomini la grammatica della natura. Il suo studio degli esseri viventi, della psiche, dei fenomeni fisici, in una parola "de rerum natura", la natura delle cose, ci lascia sbalorditi per la novità concettuale delle sue parole, anche perché figlie di un mondo ancora strenuamente legato agli Dei, agli altari, al terrore dei fenomeni naturali violenti ed ancorato alla religione ed alle superstizioni, che, dice Lucrezio imbrattano l'animo dell'uomo come "nera pece".

Sorprendente è il richiamo al mondo della scienza in un autore come Thomas Mann, che nel dialogo tra il letterato nichilista Naphta e il razionalista, cinico Settembrini della Montagna Incantata, trova il modo di parlarne con una scrittura quasi assoluta ed una modernità che ancora ci affascina. La concezione della scienza assume qui toni filosofici. La scienza è sinonimo di conoscenza, ma le verità in essa racchiuse non prescindono, secondo il gesuita Naphta, da una componente intenzionale. Il concetto di dimostrazione, ad esempio, racchiude un elemento fortemente volontario "*La scienza senza premesse è un mito. Esiste sempre una credenza, una concezione del mondo, un'idea; esiste a farla breve una volontà ed è compito della ragione spiegarla e dimostrarla*".

Concordo con Robert Musil quando afferma che sa "raccontare" bene la chimica chi è un po' scienziato e un po' scrittore. Dice infatti che "*un uomo che vuole la verità, diventa scienziato; un uomo che vuol lasciare libero gioco alla sua soggettività diventa magari scrittore, ma cosa deve fare un uomo che vuol fare qualcosa di intermedio tra i due?* ".

Naturale è il riferimento a Primo Levi che intitola la propria autobiografia "Il sistema periodico". Un chiaro riferimento al suo lavoro di chimico, che

---

non è per lui solo un mestiere, ma una passione di vita. Ogni fase della sua esistenza ne è contrassegnata in modo incisivo, tanto da essere ricondotta, via via, ad uno specifico elemento. Ecco quindi che nei ventuno racconti riaffiorano episodi legati all'Idrogeno, al Vanadio, al Piombo... che oltre ad essere stati, in alcuni casi, materia e argomento di lavoro, sono un'ottima metafora per descrivere situazioni e personaggi. Accomuna, ad esempio, il suo compagno di Auschwitz al Cerio, il suo amico taciturno al Ferro e la sua amica Giulia al Fosforo. L'ultimo capitolo della narrazione è dedicato alla storia di un singolo atomo di Carbonio. L'autore lo definisce come uno dei capitoli più belli da lui mai scritti e per chi, come me, ha passione per le scienze chimiche è, senza dubbio, uno dei racconti più belli da leggere. Queste, a proposito del carbonio, sono le sue parole: *“Potrei raccontare innumerevoli storie diverse, e sarebbero tutte vere: tutte letteralmente vere, nella natura dei trapassi, nel loro ordine e nella loro data. Il numero degli atomi è tanto grande che se ne troverebbe sempre uno la cui storia coincida con una qualsiasi storia inventata a capriccio. Potrei raccontare storie a non finire, di atomi di carbonio che si fanno colore o profumo nei fiori; di altri che da alghe minute a piccoli crostacei, a pesci via via più grossi, ritornano anidride carbonica nelle acque del mare, in un perpetuo spaventoso girotondo di vita e di morte, in cui ogni divoratore è immediatamente divorato; di altri che raggiungono invece una decorosa semi-eternità nelle pagine ingiallite di qualche documento d'archivio, o nella tela di un pittore famoso; di quelli a cui toccò il privilegio di far parte di un granello di polline, e lasciarono la loro impronta fossile nelle rocce per la nostra curiosità; di altri ancora che discesero a far parte dei misteriosi messaggeri di forma del genere umano, e parteciparono al sottile processo di scissione duplicazione e fusione da cui ognuno di noi è nato. Ne racconterò invece soltanto ancora una, la più segreta, e la racconterò con l'umiltà e il ritegno di chi sa fin dall'inizio che il suo tema è disperato, i mezzi fievoli, e il mestiere di rivestire i fatti con parole fallimentare per sua profonda essenza”*.

Primo Levi al momento della pubblicazione del libro nel 1975 non poteva sapere che di lì a pochi anni il Carbonio avrebbe mostrato un'altra delle sue forme allotropiche, aprendo la strada a mille altre sperimentazioni, ricerche e studi. Non poteva immaginare che tra le tante peripezie possibili per un singolo elemento ce ne fossero altre, ignote ai suoi giorni. I fullereni e poi i nanotubi di carbonio indicano che in chimica, la conoscenza, non si arresta

mai. Questa tesi è la mia storia e quella degli atomi di Carbonio che, in questi anni, ho avuto l'onore di manipolare e studiare per capirne, il comportamento, il come ed il perché ed i meandri più segreti e inesplorati. È bello pensare che questo antico elemento principio di vita, attuale ed eterno, così presente nelle mie giornate abbia prepotentemente invaso il mio pensiero.

# Abstract

The aim of this PhD thesis is the investigation of the photophysical properties of materials that can be exploited in solar energy conversion. In this context, my research was mainly focused on carbon nanotube-based materials and ruthenium complexes. The first part of the thesis is devoted to carbon nanotubes (CNT), which have unique physical and chemical properties, whose rational control is of substantial interest to widen their application perspectives in many fields. Our goals were (i) to develop novel procedures for supramolecular dispersion, using amphiphilic block-copolymers, (ii) to investigate the photophysics of CNT-based multicomponent hybrids and understand the nature of photoinduced interactions between CNT and selected molecular systems such as porphyrins, fullerenes and oligo (p-phenylenevinylenes). We established a new protocol for the dispersion of SWCNTs in aqueous media via non-covalent interactions and demonstrated that some CNT-based hybrids are suitable for testing in PV devices. The second part of the work is focussed on the study of homoleptic and heteroleptic Ru(II) complexes with bipyridine and extended phenanthroline ligands. Our studies demonstrated that these compounds are potentially useful as light harvesting systems for solar energy conversion. Both CNT materials and Ru(II) complexes have turned out to be remarkable examples of photoactive systems. The morphological and photophysical characterization of CNT-based multicomponent systems allowed a satisfactory rationalization of the photoinduced interactions between the individual units, despite several hurdles related to the intrinsic properties of CNTs that prevent, for instance, the utilization of laser spectroscopic techniques. Overall, this work may prompt the design and development of new functional materials for photovoltaic devices.



# Introduction

The amount of solar energy that strikes Earth in one hour is equivalent to the energy consumed by humans over an entire year; its exploitation is therefore of primary importance [1]. The huge flux of energy coming from the sun can be converted into electric energy with photovoltaic cells. Due to the impending energy crisis, the development of new generations of highly performing light-sensitive solar cells has become a key scientific and technological topic at the interface between chemistry, physics and engineering. Therefore, in order to foster research for new solar cells, the activity carried out during this Ph.D. is primarily based on the photophysical characterization of carbon nanotube (CNT) materials with the aim of obtaining useful platforms for photovoltaic applications. In particular, the research activity is framed within the project FIRB “SUPRACARBON” that is aimed at synthesizing and characterizing CNT-based materials in order to develop new photoactive devices. In this context, it is therefore essential to assess the basic photophysical features of the CNTs, and subsequently investigate photoinduced processes in properly functionalized nanotubes. The use of CNTs for solar energy conversion is currently a very important topic in the area of organic solar cells. They have quickly emerged thanks to their unique mechanical and electronic properties (described in more detail in 1.1) and they are now widely recognized as key materials in nanotechnology [2]. Carbon nanotubes consist of graphene sheets rolled to form cylindrical structures. Depending on the number of cylindrical layers, CNTs are divided into two main classes. When formed by a single layer of carbon atoms they are called single-walled carbon nanotubes (SWCNTs) while multi-walled carbon nanotubes (MWCNTs) are made up of several concentric tubes. Moreover, depending on the direction of the folding and on the arrangement of the hexagon rings along the tubular skeleton, CNTs can be metallic or semiconducting [3].

Until now, the use of CNT-based materials in the field of nanotechnology and materials science (*i.e.*, solar energy harvesting and optoelectronic devices) still remains poorly exploited. This is due to the production techniques that create CNTs without structural control of the final product. However, a rigid control of the structural properties, such as diameter and helicity is needed, for instance, to get semiconducting nanotubes with the same energy band gap. Another drawback of the otherwise unique structure of CNTs concerns their tendency to adhere to each other forming bundles. Pristine CNTs result insoluble in any solvents and only through covalent or non-covalent functionalization they can be dispersed in water or in organic media. Key-issues towards the realization of multifunctional CNTs-based nanohybrid systems concern the reliable control over the surface chemistry as well as the achievement of monodispersity in terms of length, diameter and, most importantly, chirality (*i.e.*, metallic or semiconducting CNTs).

In order to develop bulk-heterojunction photovoltaic devices based on CNTs, a few points need to be considered. First of all, the engineering of organic photovoltaic cells to convert sunlight into electrical energy requires the design of molecular donor-acceptor hybrids. In fact, these cells exploit a photoinduced electron transfer process occurring at the interface between two materials, an electron-donor (D) and an electron-acceptor (A) that are mixed to form an interpenetrating network at the nanometric level [4]. The mechanism that takes place at their contact surfaces, constitutes the analogue of inorganic semiconductor p-n junctions. The performances of these solar cells are dramatically dependent on the morphology of the manufactured photoactive layer. The low efficiency is primary due to the fact that only excitons generated close to the heterojunction are exploitable for electricity generation, because the average distance over which an exciton can diffuse (between its generation and its recombination) is quite short [5]. However, they result attractive for their cheap solution-based methods of fabrication and for their mechanical flexibility. This opens the way to low cost printing of large plastic photoactive surfaces. In the broader context of studying photoactive materials for sunlight exploitation, the research activity described in this thesis also focuses on coordination compounds. In particular, I have investigated homoleptic and heteroleptic Ruthenium(II) complexes with extended phenantroline ligands. Such complexes attract interest as light harvesting

materials for artificial photosynthesis and, more generally, for fundamental studies on their photochemical properties to deepen the knowledge on photoinduced energy and electron transfer processes [6].



# Chapter 1

## Carbon Nanotubes

Carbon is the first element of the fourth group of the periodic table. It is not abundant (approximately 0.032% of the Earth's crust), but widespread and of fundamental importance in biology. It is present in organic compounds in all living organisms, binds to calcium or magnesium to form carbonates and is ubiquitous, in the form of its gaseous oxide, in the atmosphere. Carbon has several allotropic forms: diamond and graphite, the most known, along with fullerenes, carbon nanotubes, lonsdaleite and amorphous carbon.

Carbon nanotubes (Figure 1.1), that are the predominant topics of this thesis, were discovered in 1991 by Iijima [7] who observed concentric layered tubules, made of carbon atoms, in the smut of arc discharge experiments. Since their discovery, the chemical and physical properties of carbon nanotubes have been intensively investigated.

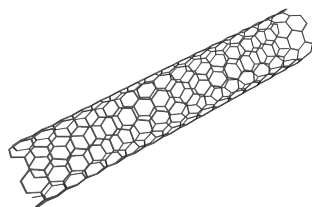


**Figure 1.1:** Schematic structure of Single walled carbon nanotube.

## 1.1 Structure and electronic properties

Carbon nanotubes (CNTs) are tubular nanostructures originated by the rolling up of graphene sheets. In particular, one or more overlapping sheets of graphite can be folded to form hollow cylindrical structures called, respectively, single-walled carbon nanotubes (SWCNTs) and multi-walled carbon nanotubes (MWCNTs). They are known for their unique mechanical, optical, and electrical properties that result from the strength of the carbon-carbon bond and the effects of quantum confinement dictated by the circumference of the nanotube. CNT are originated by graphene, a planar-hexagonal arrangement of carbon atoms distributed in a honeycomb lattice where each carbon atom has an  $sp^2$  hybridization. In particular, three of the valence electrons are involved in a covalent  $\sigma$ -type bond with other three adjacent carbon atoms and are positioned on a same plane with an angle of  $120^\circ$ . The fourth electron, not paired, is located in a  $\pi$ -orbital orthogonal to the plane of the graphene sheet and interacts with other electrons of the same type. The curvature on the structure of the carbon nanotubes changes the carbon hybridization and each  $\pi$ -orbital is more localized on a specific atom with respect to graphite. The curvature of the CNT leads to an appreciable change in pyramidalization angle ( $\theta_p$ ) and misalignment ( $\phi$ ) of the  $\pi$ -orbitals (Figure 1.2).

To understand the electronic properties of the CNTs, it is useful to start from the electronic structure of a graphene sheet. Due to a close relationship between the electrons and the related wavevectors, the electronic structure, in solid state physics, is treated in the reciprocal space (*i.e.*, the space of wavevectors). Such reciprocal space is connected to the real lattice space by specific relations of periodicity. In fact, the primitive cell on the reciprocal space (called Brillouin zone) of graphene can be derived from the unit vectors in real space  $\vec{a}_1$  and  $\vec{a}_2$  that generate the reciprocal space vectors  $\vec{b}_1$  and  $\vec{b}_2$  respectively (Figure 1.3).

The electronic structure is deduced starting from the consideration that the electrons of different carbon atoms are affected by the mutual presence as the interatomic distance is reduced. The wave functions of the valence electrons partially overlap, giving rise to hybrid states with different energy. These hybrid states are so close in energy that are no longer discrete but

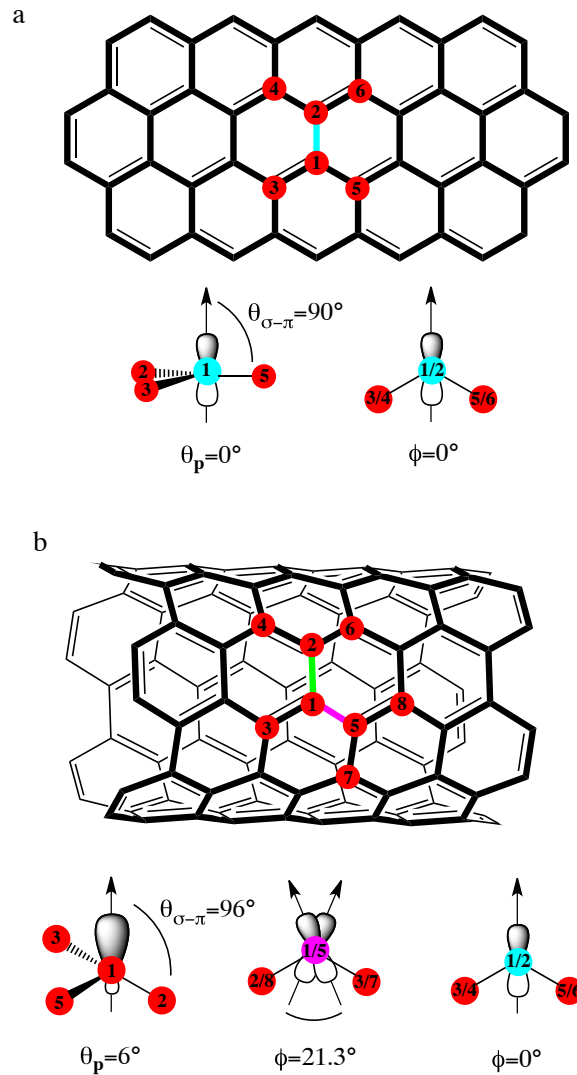


**Figure 1.2:** Pyramidalization ( $\theta_p$ ) and misalignment ( $\phi$ ) angles of graphene (a) and CNTs (b).

generate a band structure. There will be permitted bands, the valence and the conduction, separated by a forbidden band that dictated the energy gap between the others. Moreover, there is a level below which all states are occupied, and above which all states are empty called the Fermi level. The band structure is a good way to visualize the wavevector-dependence of the energy of the states, the band-gap, and the possible electronic transitions.

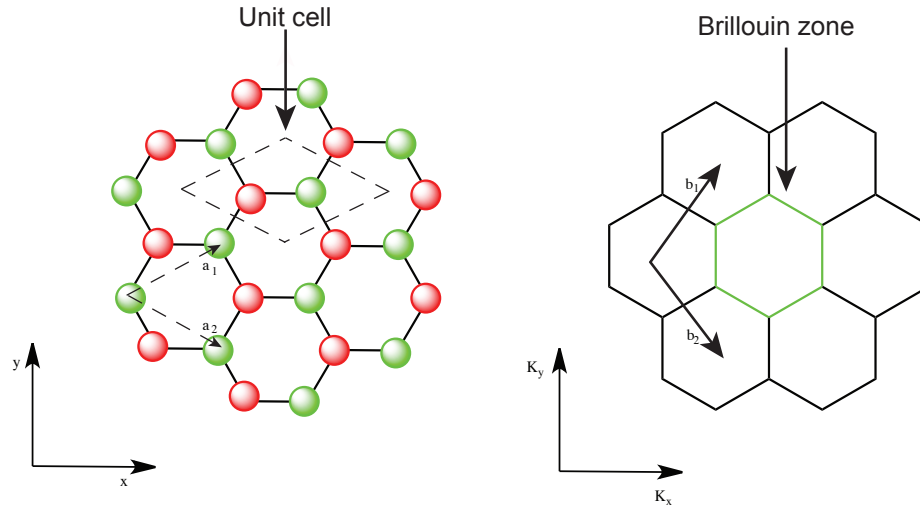


**Figure 1.3:** Schematic representation of the unit cell of graphene (left) and the 2D Brillouin zone of graphene where  $b_1$  and  $b_2$  are the reciprocal unit vector (right).

The  $\pi$ -bands in the electronic structure, which correspond to the van der Waals interactions between layers, are comparatively closer to the Fermi level than the  $\sigma$  bands, which are responsible of the strong covalent bond in the lattice plane. Therefore, the electronic energy dispersion for graphene is calculated for  $\pi$  and  $\pi^*$  bands in the first and extended Brillouin zones and can be represented as three-dimensional plot where the upper half of energy curve describes anti-bonding ( $\pi^*$ ) orbital, while the lower part describes the bonding ( $\pi$ ) orbital. In graphene,  $\pi$  and  $\pi^*$  bands are degenerate at the K-points in the Brillouin zone, where the Fermi level is crossed (Figure 1.4). Owing to symmetry constraints, two equivalent carbon atoms are present in the unit cell of the hexagonal lattice, making the graphene a zero band gap semiconductor (*i.e.*, zero gap at the K point) [8].

Carbon nanotubes exhibit different physical properties, compared to graphene, due to the folding process. In detail, the crystal structure of a nanotube depends on the axis along which the cylinder is formed from graphene, called chiral vector  $\vec{C}_h$  (1.1), and the axis that is parallel to it, called translational vector ( $\vec{T}$ ). The  $(n, m)$  indices, from which it is possible to define  $\vec{C}_h$ ,  $\vec{T}$  and  $\theta$  (chiral angle) (1.2), serve as identifiers of every SWCNT. For

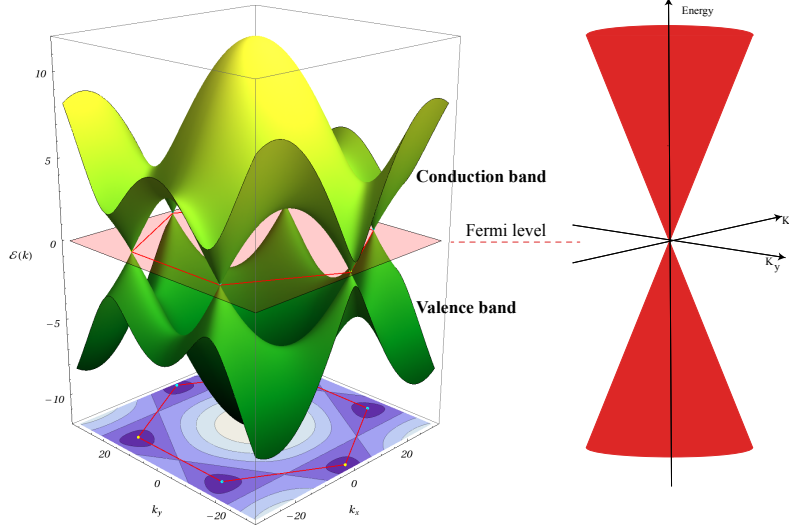


**Figure 1.4:** Graphene energy dispersion.

instance, considering the formation of a unit cell for a SWCNT (3,3) from a graphene sheet (Figure 1.5), the chiral vector is obtained through the vector addition of  $\vec{3a}_1$  and  $\vec{3a}_2$  while the translational vector is drawn perpendicular to it. The formulation of the two indices  $(n, m)$  enables the calculation of the chiral vector, the chiral angle and the diameter ( $d$ ) of the tube using the equations 1.1, 1.2 and 1.3 respectively.

$$\vec{C}_h = n\vec{a}_1 + m\vec{a}_2 = (n, m) \quad (1.1)$$

$$\theta = \tan^{-1} \frac{\sqrt{3}m}{(2n + m)} \quad (1.2)$$

$$d = \frac{|\vec{C}_h|}{\pi} \quad (1.3)$$

In order to understand the origin of the electronic bands in nanotube the reciprocal lattice space has to be considered. This latter is made by the reciprocal lattice vectors  $\vec{K}_1$  (circumferential direction) and  $\vec{K}_2$  (along the nanotube axis) that correspond, respectively, to the real space lattice vectors  $\vec{C}_h$  and  $\vec{T}$ . The electronic structure of carbon nanotubes can be obtained

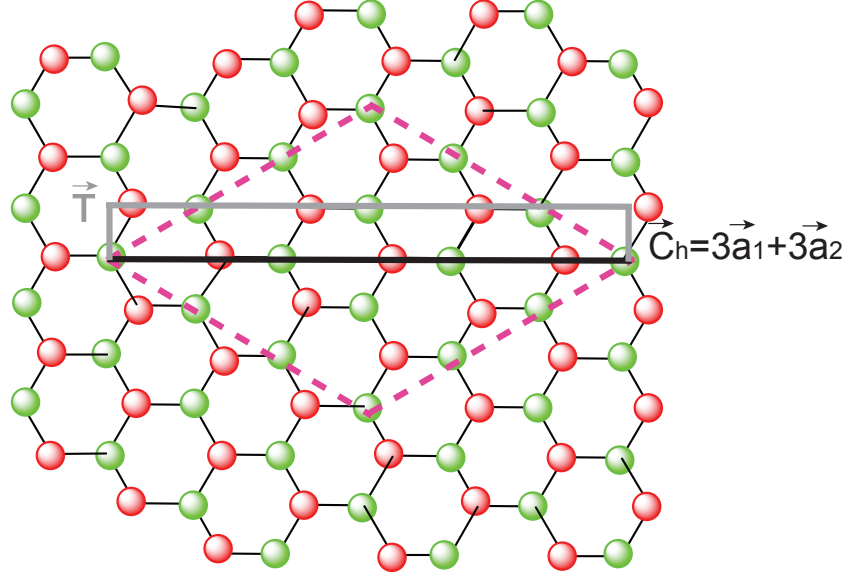


**Figure 1.5:** Formation of SWCNT (3,3) depicted on a graphene sheet.

from the energy dispersion of graphene by applying periodic limitation. In fact, the electronic wave functions of CNTs become quantized along  $\vec{C}_h$  as the circumferential length becomes comparable to the Fermi wavelength ( $\lambda_F$ ). Rolling up of graphene to form CNTs imposes on the system a periodic boundary limitation that consists on a quantization of the wavevector which can only adopt a discrete value. This concept can be used to calculate the one dimensional dispersion for carbon nanotubes (Equation 1.4) [9].

$$E_\mu(k) = E_{graphene}(k \frac{\vec{K}_1}{K_2} + \mu \vec{K}_1) \quad (1.4)$$

Where  $E_\mu(k)$  is the quantized energy,  $\vec{K}_1$  and  $\vec{K}_2$  are the reciprocal space vectors,  $\mu$  is an integer number ( $\mu = 1, 2, 3 \dots N - 1$ ),  $k$  is the wavevector and  $N$  is the number of hexagons in a single unit cell of SWCNTs. Since each unit cell contains  $2N$  carbon atoms, the final band structure of the nanotube possesses  $N$  bonding  $\pi$  and  $N$  anti-bonding  $\pi^*$  orbitals. As  $\vec{K}_2$  depends on

$n$  and  $m$ , the  $(n, m)$  indices determine the direction of the plane that will be “extracted” from the graphene energy dispersion. If the crossing plane passes through the high symmetry K-point, the nanotube will have a finite density of states at the Fermi level and will show metallic behavior. When, on the other and, the plane does not pass through the K-point, the resulting nanotube has a finite band gap and it behaves as a semiconductor (Figure 1.6).

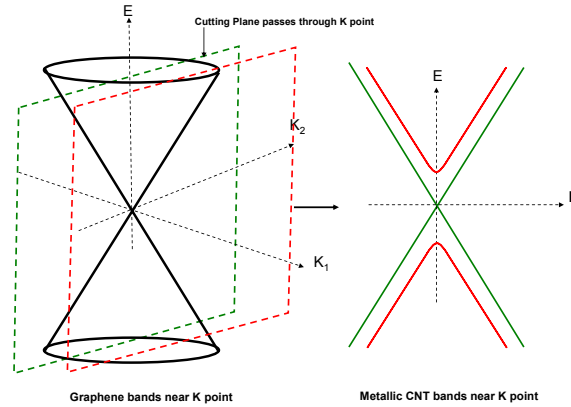


**Figure 1.6:** Linear dispersion of metallic (green) and semiconducting (red) SWCNTs.

Semiconducting and metallic SWCNTs can be directly identified using the chiral indices  $(n, m)$ . In general, if  $|n - m| = 3q$ , where  $q$  is a whole number the tube is metallic, else it is semiconducting. Moreover, on the basis of the indices  $(n, m)$  and the chiral angle ( $0^\circ < \theta < 30^\circ$ ), it is possible to divide the carbon nanotubes in three families: the *armchair* where  $n = m$  and  $\theta = 30^\circ$ , the *zig-zag* where  $m = 0$  and  $\theta = 0^\circ$  and the *chiral* where  $m \neq n$  and  $0^\circ < \theta < 30^\circ$  (Figure 1.7) [10].

In order to explore the peculiarities of metallic SWCNTs (m-SWCTNs) and semiconducting SWCNTs (s-SWCTNs) it is important to study the density of the electronic states (DOS) that describes the number of energy states, at each energy interval, which can be occupied by the electrons. In one-dimensional systems (1D) like SWCNTs, the density of the electronic states has a band structure called van-Hove singularities (Figure 1.8).

The DOS of carbon nanotubes are calculated from the  $\pi$  and  $\pi^*$  bands around the K-points of graphene involving the formation of van-Hove sin-

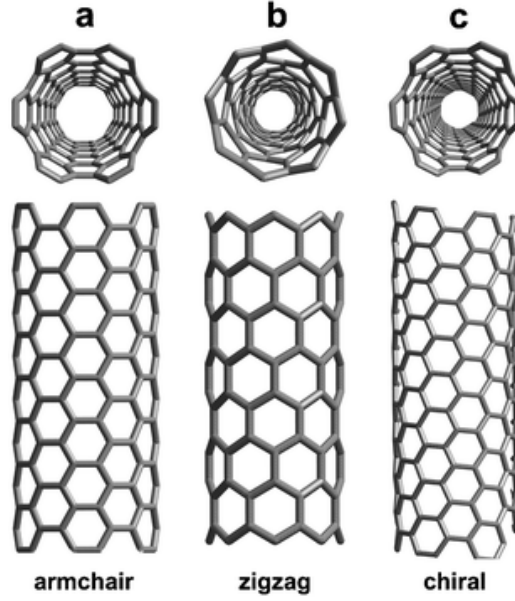


**Figure 1.7:** Molecular model for Single walled carbon nanotubes: a) armchair, b) zigzag c) chiral.

gularities of the valence ( $E_j^v$ ) and of the conduction bands ( $E_j^c$ ) (where  $j$  increases with the distance from the Fermi level). The difference in energy between the van-Hove singularities corresponds to the energy gap between different states  $E_{jj}$  ( $E_{11}$ ,  $E_{22}$ , etc.) given by Equation 1.5.

$$E_{jj} = \frac{2ja_{(C-C)}\gamma_0}{\sqrt{3}d} \quad (1.5)$$

Where  $j$  is the transition index,  $a_{(C-C)}$  is the distance between nearest neighbor carbon atoms,  $\gamma_0$  is the nearest neighbor carbon atoms interaction energy, and  $d$  is the diameter of the nanotube [11]. The energy difference ( $E_{jj}$ ) between equal pair of van-Hove singularities in the valence and the conduction bands can be assessed experimentally (*e.g.*, using absorption or photoluminescence spectroscopy) and are easily calculated for the m-SWCNTs ( $j = 3, 6, 9, \dots$ ) and for s-SWCNT ( $j = 1, 2, 4, \dots$ ) using Equation 1.6.

$$\begin{array}{ll} \text{For metallic SWNTs} & E_{11}^M = \frac{6a_{(C-C)}\gamma_0}{\sqrt{3}d} & E_{22}^M = \frac{12a_{(C-C)}\gamma_0}{\sqrt{3}d} \\ \text{For semiconducting SWNTs} & E_{11}^S = \frac{2a_{(C-C)}\gamma_0}{\sqrt{3}d} & E_{22}^S = \frac{4a_{(C-C)}\gamma_0}{\sqrt{3}d} \end{array} \quad (1.6)$$

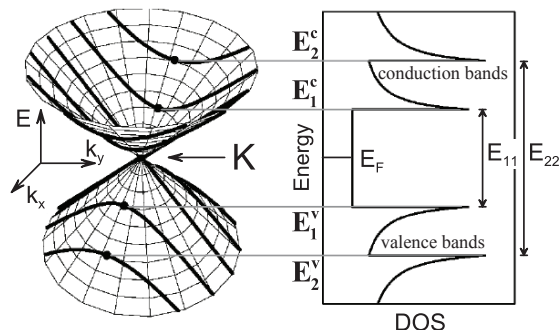


**Figure 1.8:** Representation of the density of the electronic states for a SWCNT calculated from the band structure of graphene around the K-points.

One of the most useful features of SWCNTs is the close relation between their electronic properties and the physical structure. Since the energy of the transition is inversely proportional to the diameter of a SWCNT, it is possible to build a diagram where the transition energy ( $E_{jj}$ ) is plotted as a function of the diameter ( $d$ ). This plot is called *Kataura plot* by Kataura and coworkers [12] that are the first who used this graphical representation. In figure Figure 1.9 is reported the theoretically calculated *Kataura plot*, where each dot corresponds to the energy transition  $E_{jj}(d)$  between equal pair valence and conduction bands. The energy position of the van Hove singularities has been calculated using the approximation of a linear dispersion around the K point that involves the energy bands of the graphene on the proximity of the Fermi level. The results of this treatment is that the van Hove singularities depend only on the diameter and not on the chirality. Kataura and coworkers showed that the energy differences between the van Hove singularities  $E_{jj}(d)$  have a width in energy for fixed diameter and this width increases moving away from the Fermi level. They also showed that the width of the peak positions at constant diameter was coherent with the experimental width of the peaks, determined by optical absorption spectra and Raman spectroscopy. They do not collapse on a single line due to the trigonal warping effect. The amplitude increases for decreasing diameter and increasing the  $j$ . Both evidences can be rationalized taking into account that

the approximation of a linear dispersion around the K point of graphene is only valid close to K, while the decrease of the diameter leads to a larger spacing between adjacent cutting lines (the spacing is equal to  $2/d$ ) and an increasing  $j$  corresponds to cutting lines further away from the Fermi level. The oscillating shape of every branch of the Kataura plot reflects the intrinsic strong dependence of the SWCNTs properties on the  $(n, m)$  indexes rather than on the diameter, as demonstrated by Saito and coworkers [9]. By this way, the origin of the width of the peaks can be explained by the so-called trigonal warping effect of the energy bands. For example,  $(10, 1)$  and  $(8, 3)$  tubes have almost the same diameter, but different properties: the former is metallic, the latter semiconducting. In this thesis the trigonal warping effect it is not taken into account. In fact, the linear energy dispersion around the K-point is a good approximation to rationalize the optical properties of CNTs.

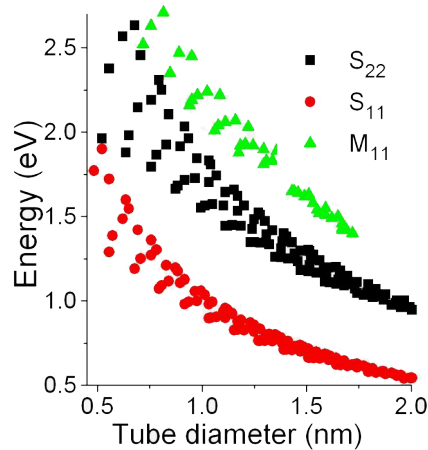


**Figure 1.9:** Kataura plot [12].

## 1.2 Optical properties

The spectroscopic methods utilized in the study of carbon nanotubes are, principally, Raman and Uv-vis-IR absorption and luminescence. Raman spectroscopy was the first to be applied to bulk amounts of SWCNTs in 1994 [13] as this method requires facile sample preparation. Absorption

and photoluminescence spectroscopy were introduced respectively in 1999 by Kataura *et al.* [12] and in 2002 by Bachilo *et al.* [14]. Photoluminescence of SWCNTs was first discovered almost 10 years after the discovery of SWCNTs, due to the low purity of nanotube materials in early preparative methods (*i.e.*, arc discharge methods [15]) and to the need to isolate SWCNTs. In fact, carbon nanotubes tend to form bundles in solution, due to high van der Waals binding energies of typically  $500 \text{ meV}/\text{\AA}$  [16]. The intermolecular interactions between tubes average out the optical characteristics of individual SWCNTs. The need to break up the bundles led to the use of surfactants and strong ultrasonic treatment, which are able to separate the tubes and to encapsulate them in micelles forming a dispersion. The most used surfactants are sodium dodecyl sulfate (SDS), sodium dodecyl benzylsulfonate (SDBS) and sodium cholate (SC).

When an incoming photon is absorbed, it creates an exciton (electron-hole pair) which then returns to the ground state in different ways depending on the nature of the SWCNT. In semiconducting CNTs the electron and hole recombine via a radiative process while in metallic species the excitons are deactivated non-radiatively. The allowed optical electronic transitions occur between the valence and the conduction bands with the same index  $v_1 \rightarrow c_1$  and  $v_2 \rightarrow c_2$  (Figure 1.10) while crossover transitions like  $v_1 \rightarrow c_2$  or  $v_2 \rightarrow c_1$  are dipole forbidden and it is possible to observe them only using cross-polarized optical geometry. Above 2 eV, the spectrum is relatively featureless and generally the transitions higher than  $v_3 - c_3$  are covered by the broad  $\pi$  resonance absorption (plasmonic region). At lower energies the absorption peaks are associated with the lowest allowed transitions. Despite the fact that SWCNTs have a sharply peaked density of states, the peaks found in the absorption spectra are broad. This is due to different factors such as the preparation of the sample (*i.e.*, the presence of the surfactant and the sonication treatment) and the spectral congestion due to the presence of numerous overlapping and closely spaced transitions [17]. However, the absorption spectra remain one of the simplest tools for the analysis of SWCNTs. In fact, it is possible to detect transitions arising both from s-SWCNTs and m-SWCNTs and to identify the various species thanks to the characteristic energy transition of each  $(n, m)$  chirality.

Photoluminescence from SWCNTs is detected in the near infrared region.

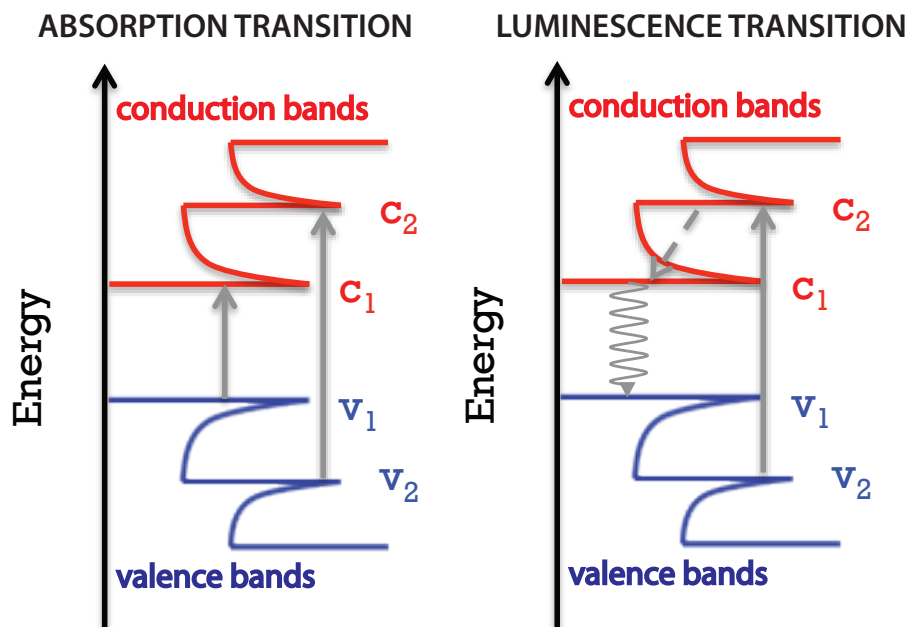


**Figure 1.10:** Representation of the permitted optical linear transitions in SWCNTs between the van Hove singularities.

The transitions occur between the first conduction band and the first valence band ( $c_1 \rightarrow v_1$ ). When a photon is absorbed, the exciton deactivates with a time of the order of 100 fs from  $c_1$  to  $c_2$  (Figure 1.10). However this process occurs only in semiconducting SWCNTs, in metallic tubes the exciton is free to go back to the valence band via non radiative processes thanks to the zero-band gap energy. Moreover, the photoluminescence is typically detectable only when s-SWCNTs are free of bundles in solution. Lauret *et al.* [18], found a relaxation time of 1 ps between conduction and valence bands in bundled SWCNTs while luminescence from the  $E_{11}$ , in individual SWCNTs, is associated with a recombination time of 20 - 180 ps (values that depend on temperature and tube diameter) [19]. Energy transfer process, between bundle tubes, occur faster by 1-2 orders of magnitude compared to the relaxation time. Considering bundles of semiconducting SWCNTs only, the energy transfer goes from the large gap donor (smallest diameter tubes)

to the smaller gap acceptor (larger diameter tubes) with a Förster Resonant Energy Transfer (FRET) mechanism [20, 21]. The presence of metallic SWCNTs provides an additional way of exciton deactivation. When the energy transfer occurs between a s-SWCNT to a m-SWCNT, the latter offers an efficient non-radiative decay channel and quenches the excitation. Then, photoluminescence spectroscopy is useful only for s-SWCNTs and requires stable dispersions of isolated tubes.

In order to identify the great variety of semiconducting species  $(n, m)$ , the photoluminescence mapping (PLM) is the most used approach. In the maps of the luminescence, the emission spectra are recorded while the excitation wavelength is changed. The resulting three dimensional plot shows the emission intensity as a function of the emission and excitation wavelengths and every emission region represents the signal from a single  $(n, m)$  species.

## 1.3 Production Techniques

Carbon nanotubes can be produced using several different techniques while new routes are continuously being developed. In this section the most common production approaches are briefly presented since improvements are always in progress and most of them go beyond the purpose of the following experimental section. The most common procedure are: arc discharge 1.3.1, laser ablation 1.3.2 and chemical vapor deposition 1.3.3 methods.

The arc discharge method was first used by Iijima [7] who successfully produced and discovered the carbon nanotubes. The arc discharge and the laser ablation techniques are the high temperature approaches in which the precursor materials (graphite and metal catalysts) are vaporized and CNTs start to nucleate on metal particles during the cooling phase. The arc discharge and the laser ablation techniques produce CNTs in relation to the carbon source (*i.e.*, the anode in arc-discharge and the target in laser ablation) and, in addition, several purification steps are required. Due to these limitations the development of a new methodology was necessary. Chemical vapor deposition is instead a low temperature synthesis technique. The chemical vapor deposition is a gas-phase technique in which the nanotubes are formed by the decomposition of a gas containing carbon. Using this approach the carbon source is continuously replaced by the flowing of the gas

and the degree of final purity allows minimization of the purification steps. Moreover, the lower temperature is more amenable of industrial implementation and mass production [22, 23].

### 1.3.1 Arc Discharge

The carbon arc discharge is probably one of the simplest methods for the production of nanotubes as well as fullerenes. The disadvantages of this technique are the strong dependence on parameters such as the atmosphere and the catalysts, and the simultaneous production of different morphologies that require several purification steps. In this method, an arc is generated between two graphite electrodes in an inert atmosphere -usually argon or helium- at reduced pressure, typically  $P \approx 500$  mbar. Without a catalyst, a mixture of fullerenes and MWCNTs are formed. The presence of graphite powder and a mixture of metal catalysts on the center of the anode favours the production of SWCNTs. In particular, when the discharge is ignited, the carbon evaporates from the anode, which is continuously eroded, and condensates on the cathode where SWCNTs are formed. The arc discharge reactor is represented in Figure 1.11 [24].

### 1.3.2 Laser Ablation

In the laser ablation method an intense pulsed laser flash is focused on a target made of graphite and catalyst. The target is located inside a furnace at  $T \approx 1200^\circ\text{C}$  under a flow of inert gas (at  $P \approx 500$  mbar) that cools the generated plume and carries the nanotubes out of the furnace where they can be collected. A schematic representation of the laser ablation system is reported in Figure 1.12. Moreover, the SWCNTs yield and diameter distributions can be varied by controlling some parameters. This technique is not suitable for mass production due to the severe working conditions. However the quality and the control on the diameter distributions obtained using the laser ablation technique make this method a useful choice to produce SWCNTs for fundamental studies [25, 26].

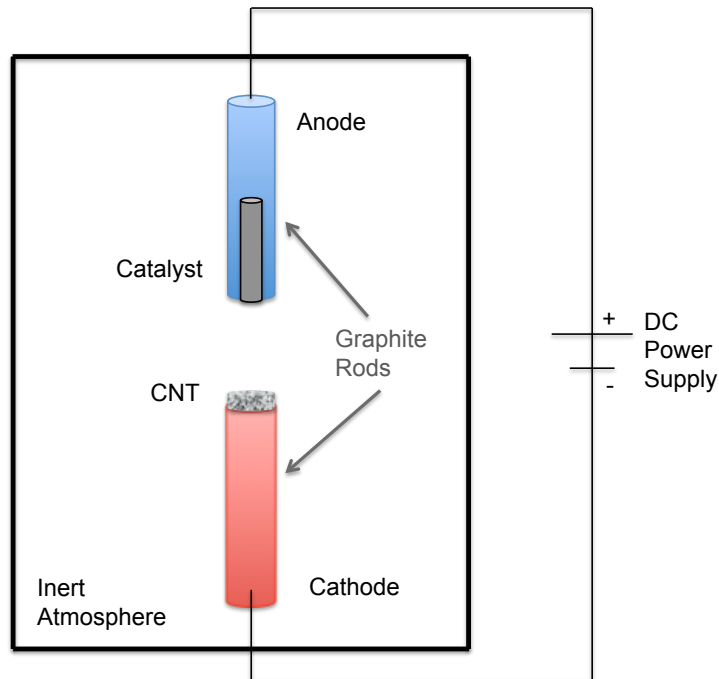


**Figure 1.11:** Schematic representation of an arc discharge system.

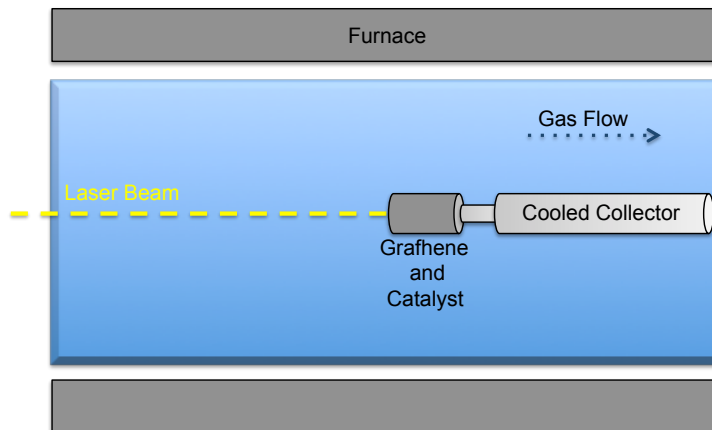


**Figure 1.12:** Schematic representation of the laser ablation for the preparation of CNTs.

### 1.3.3 Chemical Vapour Deposition

The chemical vapor deposition (CVD) method is a chemical process that uses a volatile precursor as a source of carbon, catalyst particles, and a rela-

tively low temperature ( $600\text{ }^\circ\text{C} < T < 1000\text{ }^\circ\text{C}$ ). The procedure entails the use of two gases into the reactor: a process gas (argon, hydrogen, ammonia or nitrogen) and a source of carbon in gaseous form (such as methane, ethanol, acetylene or ethylene) [27]. The CVD method is one of the most used processes in industrial production and can be divided in a large number of different variants under two main categories (i) thermochemical and (ii) plasma enhanced. The latter applies high temperature to excite the precursors while a plasma is generated using a strong electric field during the growth. The SWCNTs are grown along following the direction of the electric field [28]. The thermal CVD takes advantages of the presence of a floating or a supported catalyst. In particular, Smalley *et al.* [29] developed the HiPco process (High Pressure Carbon monoxide (CO)) in which the catalyst is floating and the carbon nanotubes grow in a flow of carbon monoxide at high pressure ( $P \approx 40\text{ bar}$ ) and temperature ( $T \approx 1000\text{ }^\circ\text{C}$ ). The catalysts are active iron clusters in the gas phase that are formed in situ from iron pentacarbonyl  $\text{Fe}(\text{CO})_5$  that decomposes due to the high temperatures in the reactor. SWCNTs are then cooled and removed from the reaction zone by a continuous gas flow. Size and diameter distributions of nanotubes can be selected by controlling the pressure of CO. In this way the raw material contains SWCNTs in a purity of up to 50 wt% and diameters between 0.7 and 1.1 nm. The chemical vapor deposition process is also used in the production of the CoMoCAT carbon nanotubes. The CoMOCAT method owes its name to the catalysts, cobalt and molybdenum, and is based on a CO disproportionation at temperature between  $700\text{ }^\circ\text{C}$  and  $950\text{ }^\circ\text{C}$  under a pressure in the range from 1-10 atm. During the SWCNTs production, cobalt is progressively reduced from the oxidized state to the metallic form and simultaneously molybdenum is converted into  $\text{Mo}_2\text{C}$  [30].

## 1.4 Covalent and Non-Covalent Functionalization on SWCNTs

Single walled carbon nanotubes are insoluble in organic and aqueous solvents due to strong van der Waals interactions ( $500\text{ meV}/\text{\AA}$ ) that cause the formation of ropes and bundles in solution. To overcome this problem they can be covalently modified or non-covalently attached by a great variety

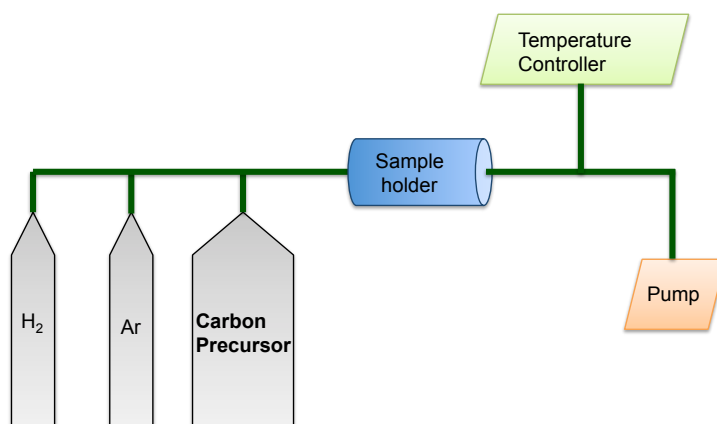


**Figure 1.13:** Schematic representation of the chemical vapor deposition for the preparation of CNTs.

of molecules that may allow the investigation and exploitation of the CNTs properties. The covalent modification is useful to enhance the solubility in various solvents but, on the other hand, the intrinsic physical properties turn out to be irremediably altered. The non-covalent functionalization, instead, involves the formation of supramolecular systems that preserve the electronic structure of the CNTs surface. Therefore, carbon nanotubes functionalization can be divided into two main categories with radically different properties of the final product.

#### 1.4.1 Covalent Functionalization of SWCNTs

The covalent functionalization of carbon nanotubes drastically affects their electronic structure due to a rehybridization from  $sp^2$  to  $sp^3$  with a resulting loss of conjugation. The reactivity of carbon nanotubes can be rationalized in terms of curvature-induced pyramidalization angle ( $\theta_p$ ) and misalignment ( $\phi$ ) of the  $\pi$ -orbitals (see 1.1) in comparison with the graphene structure. Graphene is chemically inert due to the planar, aromatic carbon structure and only few, very reactive compounds can be used for the functionalization; it has a pyramidalization angle  $\theta_p = 0^\circ$  and a misalignment  $\phi = 0^\circ$  thus in the structure there is no strain energy stored. Concerning a non-planar conjugated carbon structures, such as CNTs (mono-dimensionally curved) or Fullerenes (two-dimensionally curved), the pyramidalization an-

gles and the misalignment angles of the  $\pi$ -orbital deviate from the corresponding value of the graphene: in Fullerenes  $\theta_p = 11.6^\circ$  and  $\phi = 0^\circ$  while in carbon nanotubes  $\theta_p = 6^\circ$  and  $\phi = 21.3^\circ$  (considering the bond parallel to the nanotube axis). A carbon nanotube with the same radius as  $C_{60}$  exhibits a less distorted  $\pi$ -framework but a great deviation of the  $\pi$ -orbitals alignment. This misalignment is the origin of torsional strain in nanotubes and the driving force for chemical derivatization [31].

On the bases of the carbon nanotubes structure it is possible to find a correlation between tube diameter and reactivity. Both  $\theta_p$  and  $\phi$  are inversely proportional to the tube diameter, then smaller CNTs are expected to be more reactive than larger ones. In addition, Li and coworkers [32] and Kataura and coworkers [33, 34] demonstrated that the reactivity depends also on the CNTs chirality, considering SWCNTs with the same diameter: the zig-zag CNTs are more inert than armchairs that are less reactive than the chiral tubes.

As the physical properties of carbon nanotubes can be described within the terms of solid-state physics by using band structure representations in reciprocal space (K space), the chemical properties can be defined by the molecular orbital theory. As explained by Joselevich [35] pyramidalization and misalignment describe the localized electronic structure while the electron delocalization is not taken into account. The different reactivities of metallic and semiconducting SWCNTs can be interpreted and predicted by a classical HOMO-LUMO description and using the Hückel theory. Therefore, s-SWCNTs can be ideally associated with a very stable, thermodynamically and kinetic, aromatic molecule ( $4n + 2$  carbon atoms) with completely filled low-lying bonding orbitals and empty high-lying anti-bonding orbitals. In addition to this large resonance energy, they have a large HOMO-LUMO gap, which means that adding or extracting an electron has a relatively high energetic cost. On the contrary the m-SWCNTs have a pair of half-filled, degenerate, non-bonding orbitals which means that electrons can be added or extracted at relatively low energy cost.

The qualitative description of the reactivity of the carbon nanotubes can be tested by exploring their covalent functionalization. The chemical functionalization of carbon nanotubes has been intensively investigated for many years as reported in several reviews [36–38].

The two main strategies for the covalent functionalization are: amidation and esterification of oxidised SWCNTs and addition of organic moieties directly onto the nanotube sidewall. There are different strategies for the oxidation of pristine SWCNTs, for example using sonication in a mixture of nitric and sulfuric acid, or heating in sulfuric acid and hydrogenperoxide (Figure 1.14). In this way it is possible to obtain short opened tubes with oxygenated functions (carbonyl, carboxyl, hydroxyl, etc.). Further, they can react with alcohols or amines affording ester or amide derivatives.

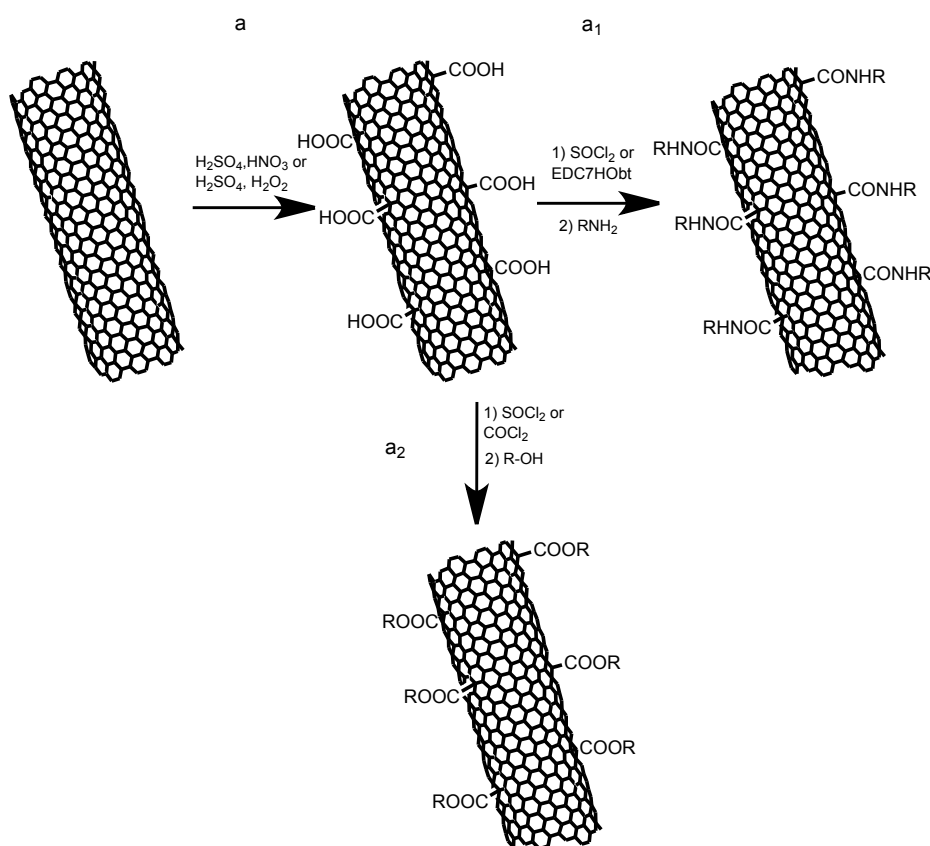


**Figure 1.14:** Schematic representation of oxidation process of SWCNTs (a) and (a<sub>1</sub>) amidation and (a<sub>2</sub>) esterification reactions.

The direct functionalization of pristine SWCNTs can be obtained via electrophilic, nucleophilic or radical additions using highly reactive species. These sidewall functionalization can be done both on pristine CNT and on oxidised species affording a great variety of addition reactions. An example

is the fluorination of carbon nanotubes using elemental fluorine at high temperature. This methodology enhances the reactivity of the sidewalls and is used to make further modifications (*e.g.*, using a Grignard reactive for the sidewall alkylation) [39]. Besides, the highly conjugated structure of SWCNTs make them good candidates of various cycloaddition reactions such as 1,3-dipolar cycloaddition reported for the first time by Prato and coworkers that achieved soluble functionalized CNTs through in-situ generation of azomethine ylides by thermal condensation of aldehydes and  $\alpha$ -aminoacids [40]. Regarding the [2+1] cycloaddition reaction it is possible to consider the addition of carbenes [41], using phenyl(bromodichloromethyl)-mercury as a source of dichlorocarbene, or the addition of nitrenes, using azido or alkyl azidoformates as precursors. A variety of organic functional groups, such as alkyl chains, dendrimers, and crown ethers, can be attached onto CNTs in this way [42]. Some representative examples are reported in Figure 1.15.

### 1.4.2 Non-covalent functionalization of SWCNTs

The non-covalent functionalization is an alternative strategy to isolate SWCNTs without affecting their intrinsic electronic and mechanical properties. This is essentially a physical modification that take advantages of van der Waals forces,  $\pi$ - $\pi$  stacking or electrostatic interactions that are established between the sidewall of the carbon nanotubes and the surrounding chemical species. As for the covalent modification (1.4.1), there is a wide literature in the field of non-covalent functionalization. The processes discussed in this paragraph are only some, representative examples and are classified on the basis of the chemicals that are used. The most representative methods will be presented, such as adsorption of surfactants, interaction with small organic molecules and polymers wrapping [38, 43]. The non-covalent dispersion of carbon nanotubes in such media is usually achieved through a series of sonication and centrifugation steps. The sonication led to the isolation of CNTs and, once some space between the tubes is made, the adsorption on the sidewall of nanotubes [44]. The centrifugation then removes the remaining larger CNT leaving individual nanotubes in the supernatant [45]. The most used techniques to evaluate the degree of debundling are electronic absorption and luminescence spectroscopy as well as microscopic techniques such as the electron transmission microscopy (TEM or cryogenic-TEM), the

## 1.4 Covalent and Non-Covalent Functionalization on SWCNTs 27

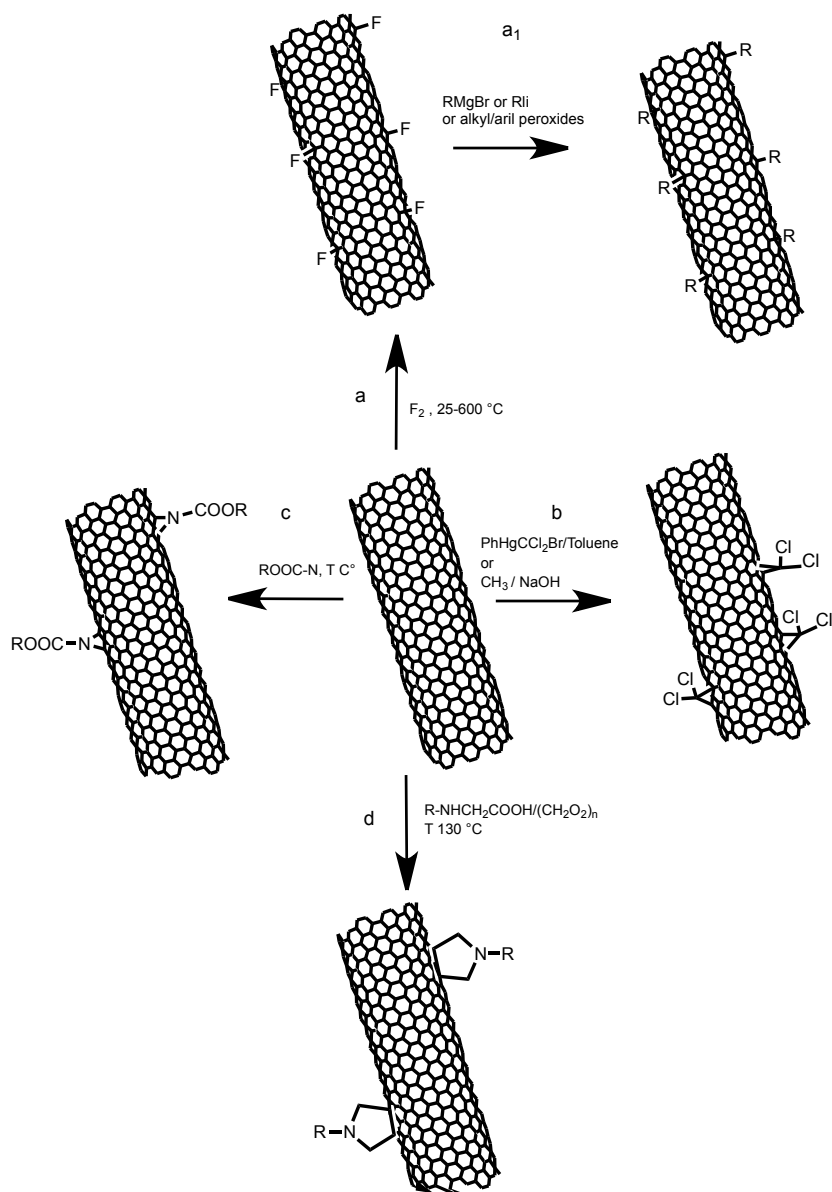


**Figure 1.15:** Schematic representation of selected reactions on SWCNTs sidewalls: (a) Fluorination and successive ( $a_1$ ) Alkylation; (b) Cycloaddition of in situ generated carbene; (c) Functionalization by nitrenes; (d) 1,3-dipolar cycloaddition azomethine ylides.

atomic force (AFM) or the scanning electron (SEM). Spectroscopic methods (in the UV-vis-NIR region) provide a simple and rapid assessment of the rel-

ative dispersion through analysis of the characteristic nanotube absorption and emission peaks (*e.g.*, van Hove singularities discussed in 1.2) that are detectable only when the SWCNTs occur as single tube in dispersion. The microscopic techniques are used in order to observe directly the extent of the dispersion thanks to the observation of the agent adsorbed on SWCNTs surface. For instance, AFM enables a three-dimensional reconstruction of the sample topography with atomic resolution and also allows to get information on the morphology of the nanomaterials.

One of the main approaches to disperse and exfoliate carbon nanotubes is based on the use of surfactants. The mechanism of dispersion is expected to be primarily due to a balance between hydrophobic and hydrophilic interactions: the hydrophobic portion of the surfactant is adsorbed on the surface of carbon nanotubes while the hydrophilic part is extended on the solvent (in most of the cases water). The assembly of the surfactant around a carbon nanotube often occur through encapsulation in cylindrical micelles (or hemimicelles) or through random adsorption. Recent simulations suggest that all of these conformations may occur depending on the surfactant concentration and on the diameter of the SWCNTs [46–49]. Generally, surfactants act as dispersants below their critical micelle concentration (CMC) [50]. However, it is possible to find cases where the performances are improved at concentrations above the CMC [51]. The most used surfactants are sodium dodecyl sulfonate (SDS) and the structurally related sodium dodecylbenzene sulfonate (SDBS); the latter possesses a phenyl ring that makes it more effective. Using AFM it has been found that the SDBS, even at high concentration of SWCNTs, can exfoliate more than 60% of the carbon materials [52]. Bile salts, like the sodium cholate (SCO), are also extremely efficient as exfoliating agents, this is due to the formation of very stable micelles around the sidewall of the carbon nanotubes [53]. The role of surfactants has been proved to be extremely important not only for debundling SWCNTs but also for the specific interaction with carbon nanotubes of different chirality. In the last decade, when the size separation of SWCNTs became crucial, one of the first separative techniques applied was the density gradient ultracentrifugation (DGU), which takes advantage of the different density of the dispersed material. It was found that for a specific combination of surfactant (1:4 SDS/SCO) the density of the dispersed carbon nanotubes

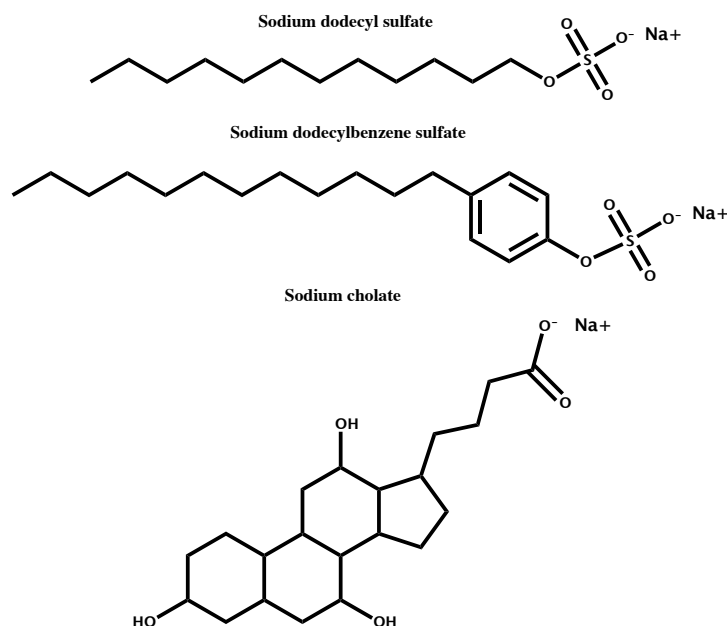


**Figure 1.16:** Surfactants used for the solubilization of SWCNTs.

depends on the electronic structure and allows the separation in metallic and semiconductive-SWCNTs [54]. The above mentioned surfactant are represented in Figure 1.16.

Thanks to the structural conformation, carbon nanotubes interact with small organic molecules opening the route to the photophysical investigation and some related potential applications. As an example, the combination of SWCNTs and porphyrins (free base or Zn-porphyrins) has proved to be an interesting donor-acceptor system for photovoltaic devices [55–57]. Other important nanohybrids are those established between SWCNTs and pyrene. The interactions are so strong that pyrene has been used to anchor various systems, such as biomolecules or nanostructures, for different applications [58, 59]. For instance, pyrene ensures the immobilization of a  $C_{60}$  unit on carbon nanotubes sidewall [60]. Pyrene is also used as a link between the carbon nanotube scaffold and porphyrin in an interesting system described by Prato *et al.* [61]. Here, a positively charged pyrene has a double function: it interacts with CNT trough  $\pi - \pi$  stacking, and is bound to a porphyrin via electrostatic interaction. These systems are depicted in Figure 1.17.

In addition, carbon nanotubes may host chromofore/luminofore via en-

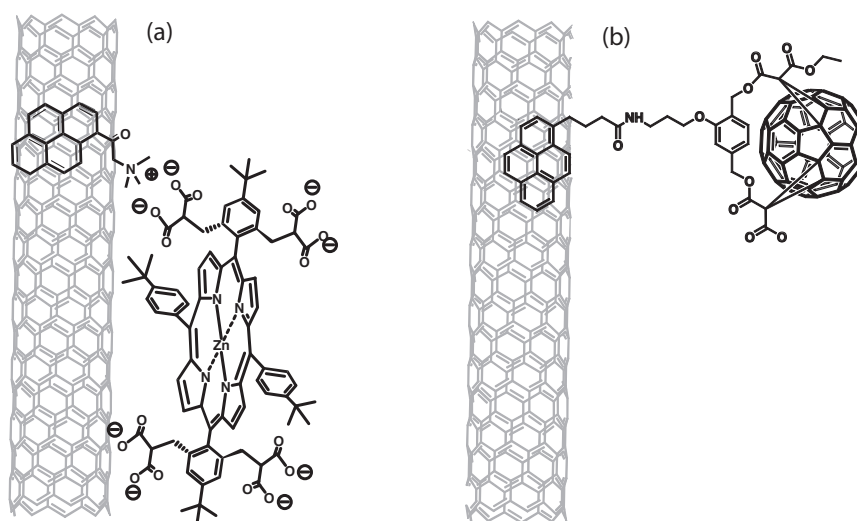


**Figure 1.17:** Examples of organic molecule used in connection with CNTs: (a) [61] (b) [60] respectively.

dohedral functionalization. The insertion of specific molecules inside the hollow space of the carbon tube has been explored as an alternative route to non-covalent functionalization [62]. The interaction between the host (confined molecules) and the guest (carbon nanotubes) led to strong electronic interaction as reported by Kataura and coworkers [63] where an encapsulated squarylium dye undergoes ultrafast energy transfer (within 190 fs) from the dye to the SWCNTs.

Finally, the physical modification of CNTs with polymers has been made with different classes of polymers interacting with CNTs in several ways (Figure 1.18). For instance, amphiphilic polymers such as poly(styrene)-*b*-poly(acrylic acid) (PS-*b*-PAA) (Figure 1.18) reported by Kang *et al.* [64] hold the SWCNTs within cross-linked, amphiphilic copolymer micelles. The micelle-encapsulated SWCNTs are compatible with a different solvent or polymer matrices, moreover, they can be used as an alternative starting material for the production CNTs composite materials. Similarly, Meuer *et al.* [65] synthesize different pyrene containing diblock copolymers based on poly(methyl methacrylate) and investigated their interactions with car-

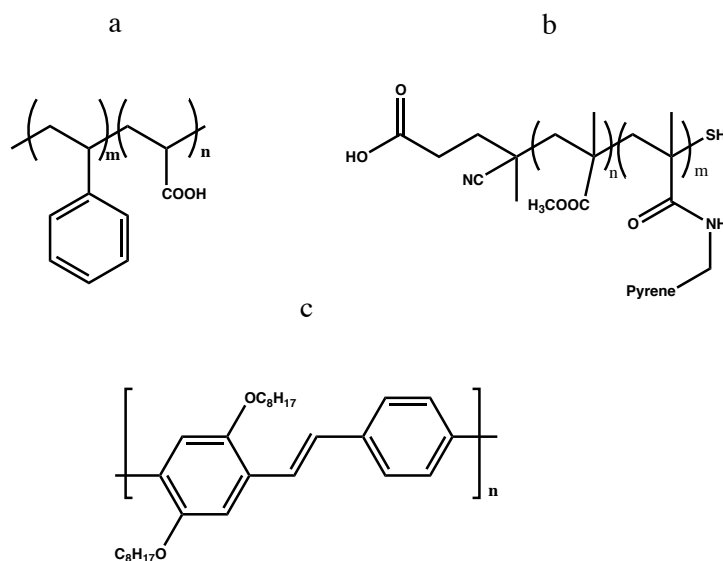


**Figure 1.18:** Examples of polymers used in connection with CNTs: (a) PS-*b*-PAA Figure 1.18, (b) Pyrene containing polymer P(MMA-*b*-C4-pyrene) [65], (c) PmPV Figure 1.18.

bon nanotubes. They showed that the molecular design is very important to tune the performance of the polymers it self; in particular the number of pyrene units that are present in the polymer are crucial. As in the previous case, polymer functionalized CNTs can be used as fillers for polymer films improving the mechanical and electrical performances.

Another interesting class is represented by conjugated polymers such as poly(phenylenevinylene) (PPV) and the related structure poly(*m*-phenylenevinylene-*co*-2,5-dioctoxy-*p*-phenylenevinylene) (PmPV) (Figure 1.18). It was found by Blau and coworkers [66] that, after the incorporation of CNT by the polymer, the electrical conductivity of the conjugated polymer film was increased of eight orders of magnitude while the luminescence properties were not affected. Because of the properties, the composite was used in the fabrication of optoelectronic memory devices [67].

Biological polymers are also used for the non-covalent functionalization of CNTs. One of the most representative examples is the structure formed by DNA and CNTs through the adsorption of the oligonucleotides on the nanotube surface. After a primary recognition between DNA and SWCNT,

a self-assembly process through rearrangement of the DNA occurs. The hybrids assume a large variety of morphologies and geometries depending on the sequences of DNA and on the nanotube diameter [68, 69]. The tunable DNA-SWCNTs hybrids open the way to medical and biological applications [70, 71]. In addition, the dispersion of SWCNTs obtained using the DNA is used to sort out CNTs by diameter using both chromatographic or ultracentrifugation techniques [72–74].

## Chapter 2

# Dispersion of SWCNTs using RAFT copolymers

Contemporary methods to obtain dispersions of carbon nanotubes take advantage of non-covalent modifications using different types of molecules. As already pointed out in 1.4.2, an increasing number of applications requires an easy access to SWCNTs dispersions, which are typically obtained by interactions between SWCNTs and surrounding materials. The debundling of SWCNTs in water as well as organic solvents has been accomplished with a variety of materials that wrap around the carbon scaffold through hydrophobic interactions [75–77]. However, a rational synthetic approach to assemble tailored amphiphilic molecules able to debundle SWCNTs in polar media through non-covalent interactions and provide them specific properties has been only rarely pursued [78]. In order to achieve more effective dispersion of SWCNTs, polymer wrapping represents one of easiest and most effective strategies, in particular through the use of amphiphilic polymers.

The reversible addition-fragmentation chain-transfer (RAFT) synthesis of poly(glycidyl methacrylate)-*b*-polystyrene (PGMA-*b*-PSt) and poly(glycidyl methacrylate)-*b*-poly(butyl acrylate) (PGMA-*b*-PBA) copolymers followed by the post-polymerisation treatment through morpholine permits the rational design of amphiphilic block copolymers that can separate single walled carbon nanotubes and disperse them in aqueous media. The van der Waals interactions and the  $\pi - \pi$  forces established between the copolymers and SWCNTs allow the preservation of the nanotube  $sp^2$  carbons structure and

hence the electronic properties of the carbon nanomaterial [79]. It is important to notice that RAFT polymers have been previously used in connection with SWCNTs for instance in the study of (i) CNT and RAFT polymers containing pyrene systems, [78] (ii) interaction between cholesterol-containing polymers and CNTs in apolar organic solvents, [80] (iii) polystyrene chains grafted on the surface of MWCNTs using a RAFT agent immobilized on the carbon nanotube sidewall [81].

In this chapter the polymers synthesis, the dispersion procedure and the following characterization by spectroscopy (Vis-NIR) and microscopy (AFM) of the obtained dispersion are discussed [82].

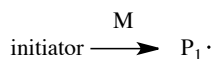
## 2.1 Synthesis of the polymers

The reversible-addition fragmentation chain-transfer (RAFT) procedure is a versatile and powerful tool to design polymers with specific structure and restricted distributions of molecular weights [83]. Furthermore, the post-polymerization modification represents a good strategy for obtaining the tailored amphiphilic block copolymers [84].

The RAFT process appeared in literature in the early 1970s [78] but the thiocarbonylthio compound, one of the most used RAFT agent, was introduced only in 1998 [85]. This technique makes use of a source of radicals (e.g., thermochemical initiator), selected monomers and a chain transfer agent (the thiocarbonylthio compound). The latter provides control over the generated molecular weight and polydispersity during the polymerization. To have an overview of the RAFT polymerization process it is important first to consider that radicals are neither formed nor destroyed during the RAFT process. As indicated by the name itself, RAFT is a chain reaction where chains are built via radical reactions of monomers and then stopped -by combination or disproportionation- when the propagating radicals react with each other (Figure 2.1 steps a, b and f). RAFT polymerization is a kind of living polymerization where all chains are created at the beginning and continue to growth until the monomers are consumed. Most of the chains are maintained inactive during the polymerization thanks to the RAFT agents that react with the propagating radicals by reversible chain transfer (Figure 2.1 steps c-e); the living character of a radical polymerization is given by

a restraint of all processes that terminate chains irreversibly.

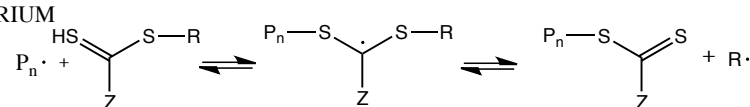
(a) INITIATION



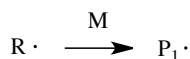
(b) PROPAGATION  
(CHAIN GROWN)



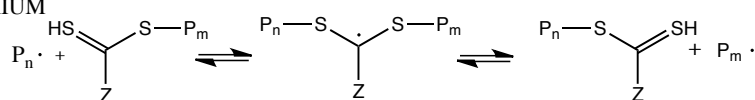
(c) RAFT PRE-EQUILIBRIUM



(d) REINITIATION



(e) RAFT MAIN-EQUILIBRIUM



(f) TERMINATION



**Figure 2.1:** Schematic representation of the polymerization via reversible-addition fragmentation chain-transfer.

In RAFT synthesis the molecular weight increases proportionally with the conversion degree and can be calculated using the equation 2.1 where  $[M]_0$  and  $[RAFTagent]_0$  are the initial concentration of the monomer and RAFT agent,  $[M]_t$  is the concentration of the monomer at time  $t$ , and  $m_M$  is the monomer molecular weight. Using the reversible addition fragmentation chain transfer reaction it is possible to obtain a narrow molecular distribution and complex molecular architectures [84].

$$\bar{M}_n(\text{calc}) \approx m_M \frac{[M]_0 - [M]_t}{[RAFT - agent]_0} \quad (2.1)$$

In this section, the synthesis of poly(glycidyl methacrylate)-*b*-polystyrene (PGMA-*b*-PSt) and poly(glycidyl methacrylate)-*b*-poly(butyl acrylate) (PGMA-*b*-PBA) and the successive conversion in amphiphilic block copoly-

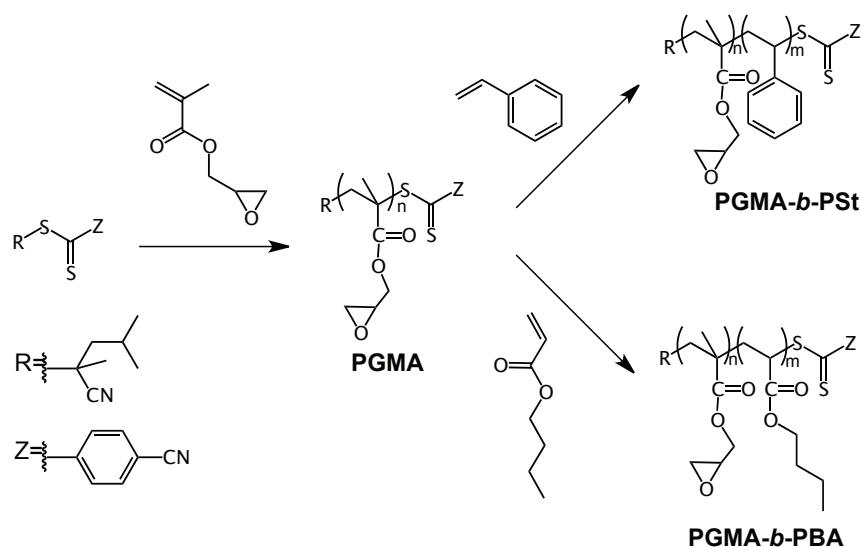


**Figure 2.2:** Schematic description of the synthesis of the block copolymers. (a) RAFT agent 2-cyano-4-methylpent-2-yl 4-cyanodithiobenzoate. (b) PGMA macro RAFT. (c) PGMA-*b*-PSt, (d) PGMA-*b*-PBA.

mers Poly(2-hydroxy-3-morpholinopropyl methacrylate)-*b*-polystyrene (PHMPMA-*b*-PSt) **1** and Poly(2-hydroxy-3-morpholinopropyl methacrylate)-*b*-poly(butyl acrylate) (PHMPMA-*b*-PBA) **2** is shown. PGMA-*b*-PSt and PGMA-*b*-PBA were synthesized as described by Benaglia *et al.* [84] starting from the poly(glycidyl methacrylate) (PGMA) macroRAFT and using as RAFT agent 2-cyano-4-methylpent-2-yl 4-cyanodithiobenzoate. The PGMA macroRAFT agent was then extended using as monomers styrene or butyl acrylate to create the PGMA-*b*-PSt and PGMA-*b*-PBA respectively (Figure 2.2).

Amphiphilicity is achieved upon treatment with morpholine, which makes the resulting polymers soluble in a wide range of solvents from chloroform to water. The post-polymerization treatment is a nucleophilic ring-opening reaction of the epoxy group that is carried out in DMSO at 80° with an excess of nucleophilic reagent (morpholine). A schematic representation of the synthesis of the block copolymer is described in Figure 2.3.

Solubility in organic polar solvents like dimethylformamide (DMF) allows the dispersion in water of the self-assembled material consisting of the

wrapped amphiphilic block copolymers and SWCNTs. The copolymer **1**, which contains the polystyrene component, results more effective in dispersing SWCNTs in water when compared to the copolymer analogue **2** that is private of the polystyrene fragments. In the latter case, the absence of aromatic moieties on the copolymer leads to weaker interactions with the carbon nanotube sidewalls.

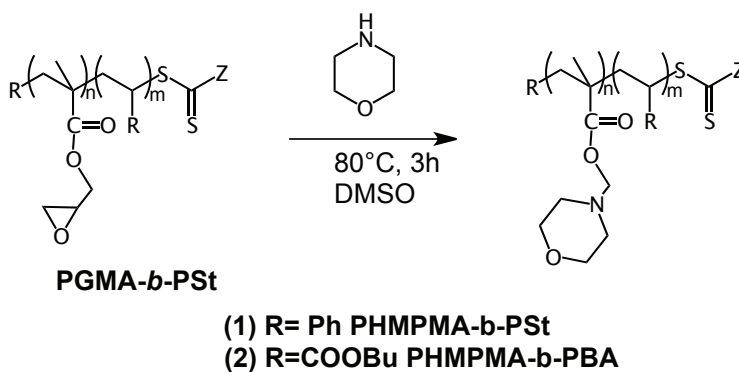


**Figure 2.3:** Schematic representation of the post-polymerization treatment of (a) (PHMPMA-*b*-PSt) **1** (b) (PHMPMA-*b*-PBA) **2**.

## 2.2 Making a dispersion of SWCNTs

The procedure for preparing a dispersion of SWCNTs is made by few simple steps. First the polymer (0.2 mg) and the SWCNTs (0.1 mg) are mixed together in 1 mL of DMF and then sonicated for 30 min. After this first stage, the sample looks as a transparent liquid with black solid material floating on top, due to the different solubilization properties of the two components: the polymer is completely solubilized in DMF while the CNTs are completely insoluble. Accordingly, during the first step no interactions occur between the carbon nanotubes and the polymer, even during the sonication process, however this treatment is of primary importance to ensure the complete solubilization of the polymer. In the second step, deionized water (1 mL) is added to the mixture at uniform dropwise rate (1 mL/min), followed by another sonication step of 30 min. The latter is repeated two more times to

increase the amount of water from 1 to 3 mL and get a DMF:water ratio of 1:3. As the amount of water is progressively increased, the lipophilic part of the polymer becomes insoluble and tends to form micelles [64]. If carbon nanotubes are present, the hydrophobic portion of the polymer interacts with the carbon scaffold while the hydrophilic part gets solubilized in water. Hence, the slow water addition leads to the formation of micellar particulate around the CNTs enabling, in this way, their dispersion.



**Figure 2.4:** Picture of **1.SWCNT** and **2.SWCNT** before filtration.

Eventually, the dispersion is filtered through cotton to remove the largest non-dispersed particles. The dispersions, hereafter mentioned to as **1.SWCNT** and **2.SWCNT**, are transparent but **1.SWCNT** is dark grey and **2.SWCNT** is light grey, a first indication of the different ability of the two polymers to disperse the carbon nanotubes (Figure 2.4) [86]. Finally, to remove the slightest non-dispersed residual, a centrifugation step is applied (2h, 20000 rpm) and the resultant supernatant is then collected. A schematic representation of the sample preparation procedure is reported in Figure 2.5.

## 2.3 Spectroscopic investigation

With the intention of demonstrating the presence of debundled SWCNTs obtained using the above described process and, therefore, to assess the degree of dispersion, the samples were investigated by absorption and luminescence spectroscopy in the visible and near-IR (Vis-NIR) regions. These

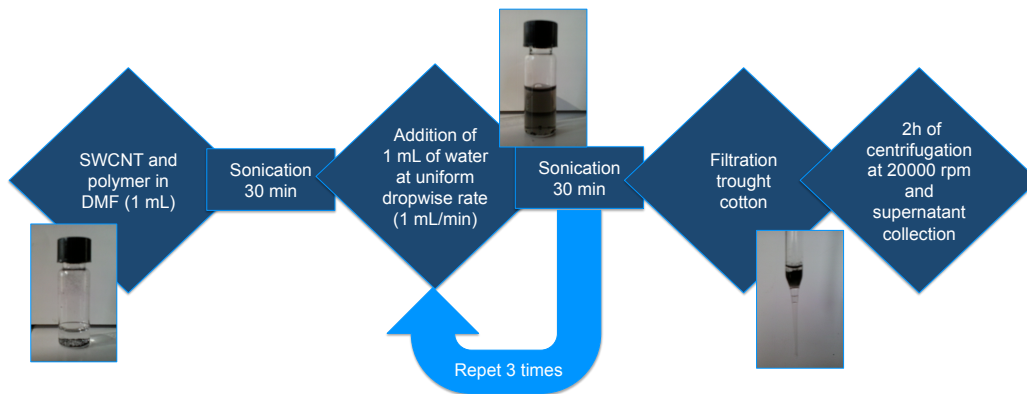


**Figure 2.5:** Schematic description of the sample preparation steps.

spectroscopic techniques are the simplest tools for the analysis of SWCNTs-based samples.

The optical absorption spectra in the Vis-NIR regions of SWCNTs are characterized by absorption bands originated from the transitions between the van Hove singularities within the density of states. In particular, each  $(n, m)$  carbon nanotube absorbs light proportionally to the energy difference between the equal pair valence and conduction bands. When no separation techniques are applied (*e.g.*, ultracentrifugation or chromatography), the absorption spectrum of SWCNTs is made by numerous absorption peaks due to the presence of several species: spectral features are poorly resolved and the closely spaced bands corresponding to the large variety (*i.e.*, diameters) of SWCNTs are often not clearly discernible. Such bands are also broadened by electronic coupling effects in the presence of aggregated particles. Moreover, a strong background originated from the nanometric particles light scattering and a high ratio of metallic tubes is characteristic of the absorption spectrum of the CNTs [17].

Luminescence spectroscopy, and in particular photoluminescence mapping (PLM), is used to characterize the different chirality  $(n, m)$  of s-SWCNTs present in the sample [14]. Furthermore, the PLM can be used to estimate the degree of dispersion because clear emission bands are obtained only when the tubes are well individualized. While the spectral position of the emission band can be used to identify the SWCNTs species and to evaluate the dispersion degree, it is not possible to correlate the emission intensity of the

SWCNTs to quantitative information because the intensity is influenced by different parameters (the specific composition, the presence of impurities) difficult to control [87].

The Vis-NIR absorption spectrum of the samples, before the final centrifugation step, shows different behavior depending on the polymer that has been used: in the case of **1.SWCNT**, several well-resolved and relatively intense bands are present, whereas the features of **2.SWCNT** are weaker and less resolved (Figure 2.6 a). Upon centrifugation, the samples exhibit different trend. In the case of **1.SWCNT**, the supernatant shows the same optical transitions observed for the uncentrifuged sample but, as expected, with a substantially weaker background (Figure 2.6 b). On the contrary, the spectra of **2.SWCNT** exhibit much less pronounced differences in terms of resolution and absorbance, between the uncentrifuged sample and the supernatant fraction of the centrifuged sample (Figure 2.6 b). This suggests that most of the SWCNTs remain bundled in the presence of the polymer **2** and so they are removed in the preliminary filtration step.

To show the enhanced dispersion power of **1**, the so-called resonant area of the absorption spectra of the two samples in the NIR region has been determined (Figure 2.7) [88]. The absorption spectra may provide a good tool to roughly assess the amount of SWCNTs that has been dispersed, even if a precise analytical quantification is not possible. In particular, the degree of individualized SWCNTs is obtained by determining the so-called dispersion efficiency and resonant ratio (RR). To estimate the dispersion efficiency, one has to consider the absorbance value at a selected wavelength; the value obtained can be related to the SWCNTs concentration by the Lambert-Beer law. This method is somewhat imprecise due to different and not controllable factors: (i) the uncertainties on the extinction coefficients of SWCNTs (ii) the difficult determination of the background level and (iii) the lack of information regarding the actual CNT species ( $n, m$ ) that are present in the sample. On the contrary, the resonant ratio aims at assessing the relative weight of the absorbance background, affording a rough estimation of the extent of debundling [77]. The resonant area is the ratio between the total area of the absorption spectrum and a linear area of the background (as exemplified in Figure 2.7 a). In particular, the RR is obtained by dividing the resonant area (Figure 2.7 a, in red) and the non resonant background

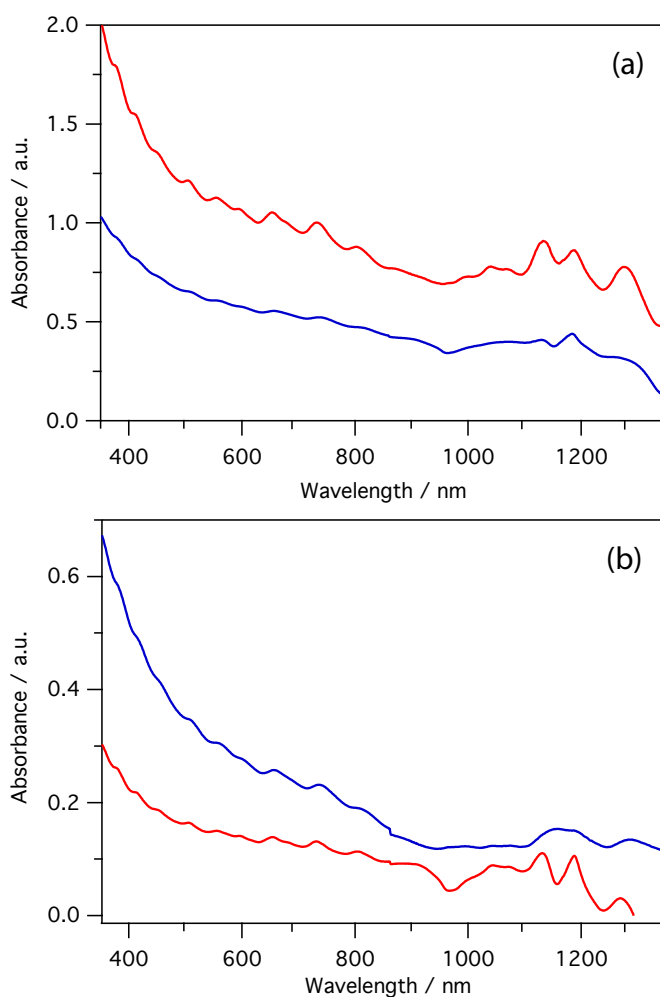


**Figure 2.6:** Absorption spectra of **1.SWCNT** (red) and **2.SWCNT** (blue) dispersed in DMF:water 1:3: (a) before centrifugation (b) after centrifugation (supernatant fraction).

area (Figure 2.7 a, in grey). In this way, the RR reflects, qualitatively, the ability of the polymer to disperse SWCNTs: high values of RR indicate a better dispersion capability, namely a higher signal-to-noise ratio of the overall spectral profile. The resonant ratio of **1.SWCNT** and **2.SWCNT** were calculated between 950 nm and 1340 nm (in order to evidence the  $E_{22}$  transition) and it is reported in the right panel of Figure 2.7. Such comparison supports the stronger capability of **1** to debundle SWCNTs compared to **2**.

To estimate RR, absorption spectra were recorded with samples prepared in parallel, following the procedure described previously.

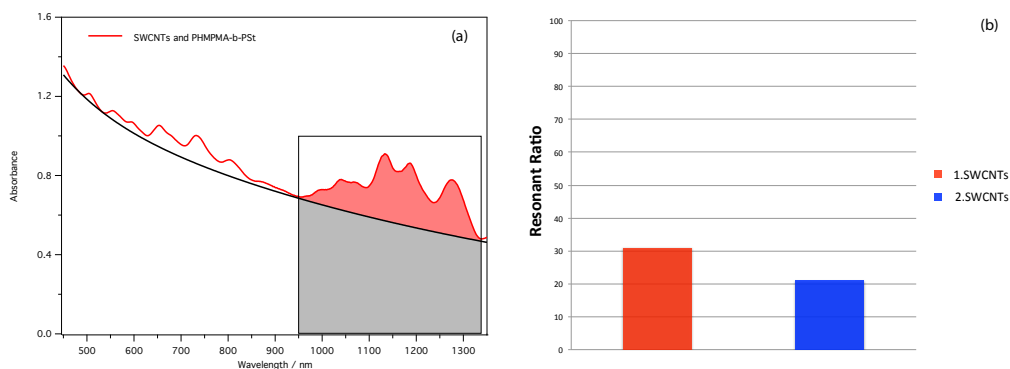


**Figure 2.7:** a) Absorption spectrum of **1.SWCNT** with the resonant area (red) and non-resonant background (gray); b) Comparison between the resonant ratio of **1.SWCNT** (red) and **2.SWCNT** (blue).

Luminescence studies on SWCNTs are reliable only after a debundling treatment that leads to the isolation of the tubes as dispersions. In fact, it is known that the fluorescence of semiconducting-SWCNTs is quenched by the non-emitting metallic analogues (m-SWCNTs) and can be reduced by exciton energy transfer to species with a lower band gap energy (larger diameter tubes) in the presence of bundles. Therefore, fluorescence spectroscopy is a powerful method to assess the extent of dispersion of SWCNTs [10, 14, 87, 89]. The comparison between the fluorescence maps of **1.SWCNT** and **2.SWCNT** recorded before the centrifugation step (Figure 2.8), shows that in the former case the luminescence peaks are more numerous, intense and resolved. In the dispersion obtained using the polymer **2**, only a limited number of weak emission bands are present with a high contribution of instrumental noise due to light scattering. The centrifuged fraction preserves the emission properties in the case of **1.SWCNT**, while only minor signals are detectable in the sample **2.SWCNT**, as shown in Figure 2.9.

The centrifugation step is useful to understand what is happening in the samples because, as demonstrated by the spectroscopic investigation, this step brings about peculiar changes for samples **1.SWCNT** and **2.SWCNT**. Only in the former case the supernatant persists as a stable dispersion for

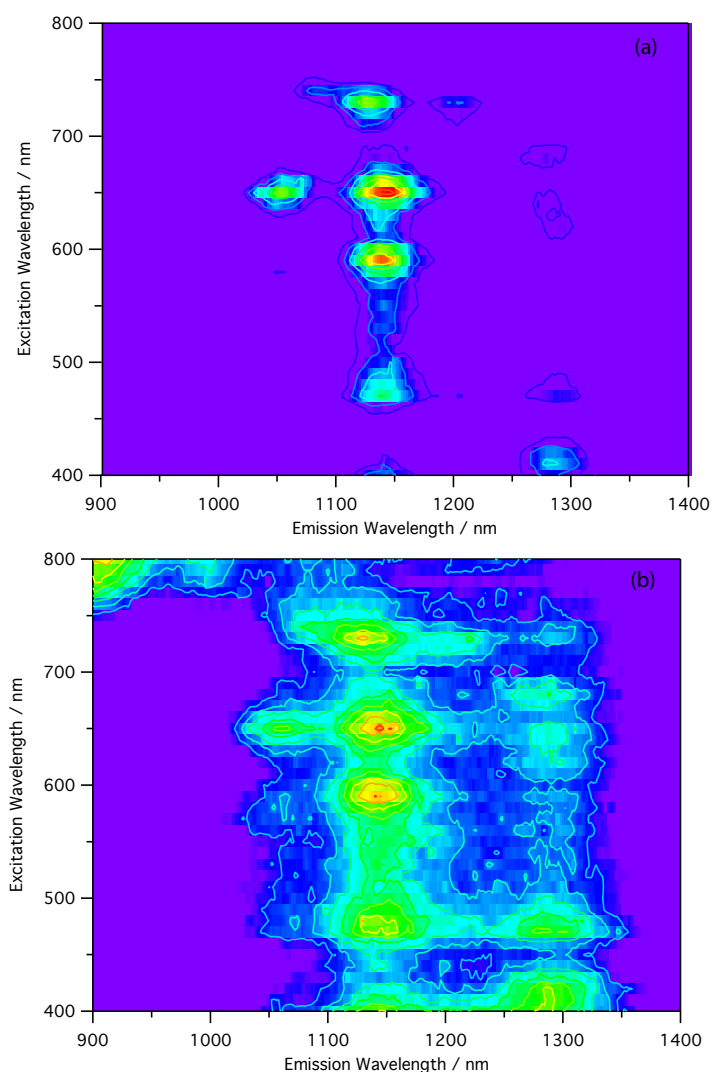


**Figure 2.8:** Photoluminescence map of uncentrifuged (a) **1.SWCNT** and (b) **2.SWCNT** in DMF:water 1:3.

several days, indicating the typical well resolved absorption and photoluminescence bands of highly dispersed samples (though of lower intensity if compared with an uncentrifuged sample, Figure 2.9). On the other hand, the precipitate of **1.SWCNT** requires a 30 min sonication step to re-disperse the SWCNTs contained in it. The sample thus obtained, however, is not stable for more than one day and the photophysical characterization affords poorly

resolved absorption and emission features (Figure 2.9 b-d); this suggests that the sample is primarily made of SWCNTs only, with negligible amounts of polymer. This trend is not observed with the sample **2.SWCNT**, because there are no relevant differences between the precipitate and supernatant of the centrifuged sample.

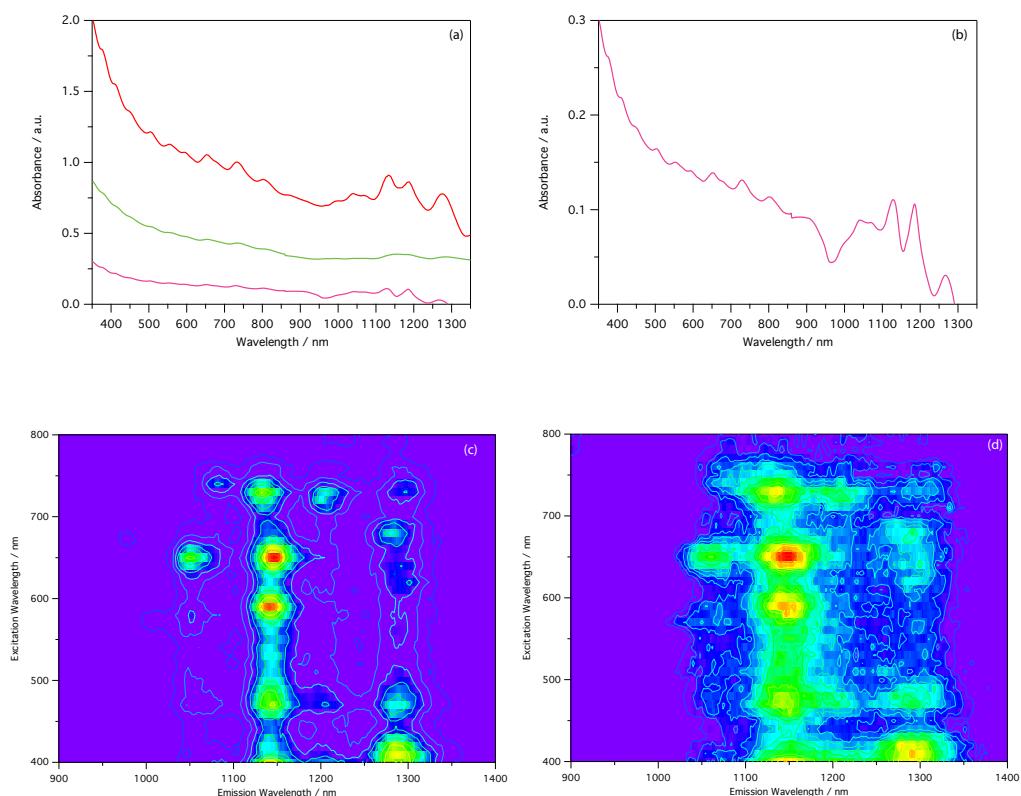


**Figure 2.9:** a) Comparison between the absorption spectra of **1.SWCNT** in DMF:water 1:3 as centrifuged and uncentrifuged (red) samples. For the latter are reported both the spectra of the supernatant (pink) and of the precipitate (green). b) Magnification of the highly resolved and background free absorption spectra of the supernatant. (c) and (d) are the photoluminescence maps of the centrifuged samples of **1.SWCNT** in as, respectively, supernatant and precipitate.

## 2.4 Atomic force microscopy study

The dispersion of polymer coated SWCNTs was then analyzed using atomic force microscopy (AFM), where the effective solubilization of the nanotubes with the polymer PHMPMA-*b*-PSt is compared to PHMPMA-*b*-PBA. Films of the dispersions of **1.SWCNT** and **2.SWCNT** were prepared via spin coating using as support a freshly cleaved mica surfaces. The samples were investigated at three different stages of preparation: a) before filtration, b) after filtration and c) after centrifugation (supernatant fraction).

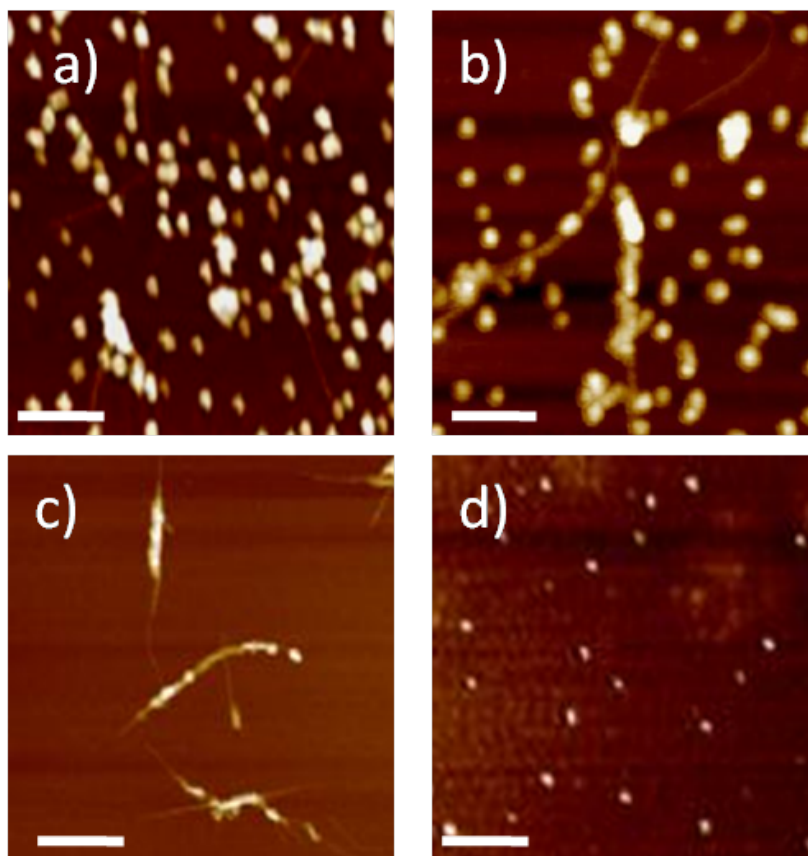


**Figure 2.10:** Atomic force microscopy (AFM) images showing **1.SWCNT** deposited on mica supports a) before filtration, b) after filtration, c) after centrifugation (supernatant fraction). Image d): **2.SWCNT** after filtration, deposited on mica showing no stabilised SWCNTs. Scale bars are 200 nm in length.

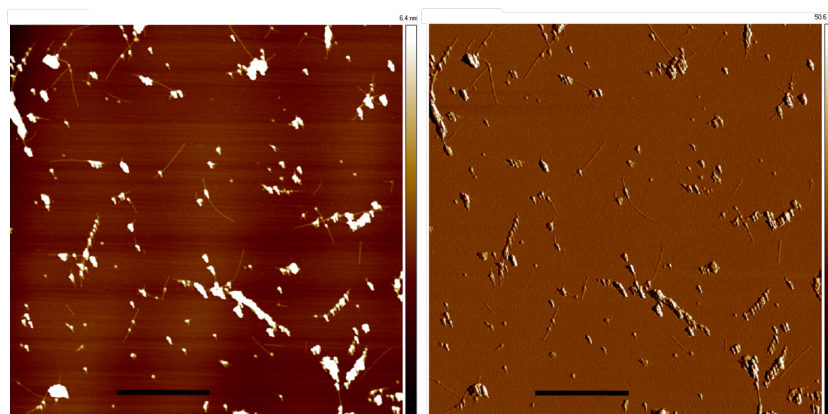


**Figure 2.11:** AFM peak force mode of height (left) and peak force error (right) images of **1.SWCNT** deposited on mica supports after centrifugation (supernatant fraction). Scale bars are 1  $\mu\text{m}$  in length.

The analysis of the dispersion before the filtration step reveals large micelles both for **1.SWCNT** and **2.SWCNT** (the former is shown in Figure 2.10 a) due to a large amount of polymer inside the dispersion. The investigation of the dispersions after filtration shows a remarkable difference between **1.SWCNT** (Figure 2.10 b) and **2.SWCNT** (Figure 2.10 d). When the polymer **1** is present, the stabilization of the SWCNTs is demonstrated by the presence of polymer wrapped along the length of the carbon nanotubes, while in the case of **2.SWCNT** only not interacting polymeric particles are present suggesting, as already seen in 2.3, that nanotubes bundles were removed during filtration. After the centrifugation, the sample **1.SWCNT** is formed by individualized carbon nanotubes coated by the polymer and, differently from what is shown after the filtration, only a negligible quantity of free polymer is present (Figure 2.10 c). In particular, Figure 2.10 c shows the wrapping of polymer **1** along the length of the carbon nanotubes enabling their dispersion.

In Figure 2.11 a 5-fold larger area is provided, in order to confirm the presence of many polymer wrapped SWCNTs on the AFM scanned surface.

## 2.5 Conclusion

In conclusion, this chapter shows a rational approach for the preparation of functional block-copolymers aimed at the dispersion of SWCNTs in aqueous media via non-covalent interactions. The photophysical study and AFM characterization have been used to follow each single preparation and manipulation step and to demonstrate the capability of the proposed dispersion procedure. This research shows that the combination of the versatile RAFT polymerization technique with the post-polymerization treatment of PGMA allows the preparation of a virtually unlimited library of polymers. Moreover, the non-covalent functionalization of the SWCNTs is a viable strategy to overtake the crucial solubilization problem. The above presented approach opens the way to a rational modification of carbon nanotubes surfaces, via non-covalent interaction, involving the dispersion in polar media. Notably, the biocompatibility of the polymers and the possibility of further functionalization, makes the proposed method potentially useful for biological applications [90].



## Chapter 3

# SWCNTs enriched in (7,6) chirality and OPV systems

Single walled carbon nanotubes are fascinating materials with interesting optical and mechanical properties. The interaction between SWCNTs and organic molecules has been explored to modify the electronic properties of the carbon nanotubes and then to obtain photoactive materials for different applications [91]. In particular, photoinduced processes attracted much interest because of their relevance to photovoltaics. For example, adducts of SWCNTs with pyrene or porphyrin exhibit fast electron transfer, leading to long-lived charge separated states [2, 92].

Until now, the research works published in literature are primarily based on carbon nanotubes with high polydispersity in terms of chirality. In fact, peculiarity of the carbon nanotubes is the presence of different species that differ each other by the length of the diameter and by the chiral angle. When properly treated and dispersed, the individual species are characterized by peculiar spectroscopic features (*i.e.*, absorption and emission bands) that allow identification.

In this chapter, SWCNTs enriched in a single chirality are used, in order to obtain an optimal matching between the electronic energy level of the donor and the acceptor units. New systems made of (i) electron-accepting single chirality enriched SWCNTs and (ii) electron-donating dimethylamino distyrylbenzene derivatives **1** and **10** have been designed (Figure 3.2). A new synthetic approach for the preparation of compound **1** has been developed.

Covalently functionalized SWCNTs have been prepared through an amidation reaction and characterized with TGA analysis and Raman spectroscopy. The positive outcome of the functionalization reaction has been confirmed by both techniques. Moreover, the photophysical properties of the hybrids have been investigated in order to evidence the photoinduced processes occurring between the individual entities and evaluate their applicability in photovoltaic devices.

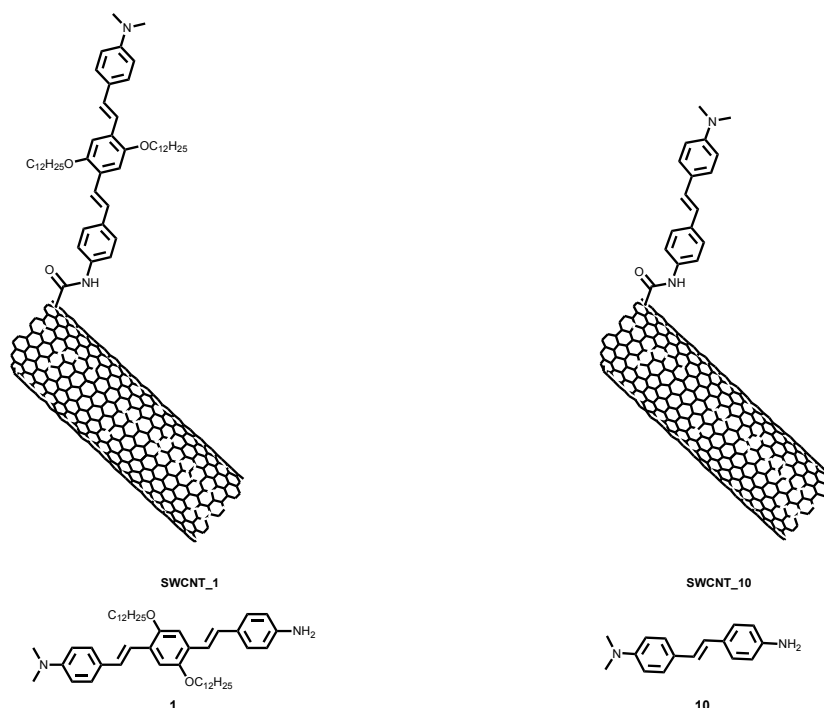


**Figure 3.1:** Representation of designed Acceptor-Donor systems. SWCNTs were functionalized with amino derivatives **1** and **10** to give final systems **SWCNT\_1** and **SWCNT\_10** respectively.

### 3.1 Synthesis of the OPV molecules and SWCNTs (7,6) functionalization

Herein, the synthesis of the oligo p-phenylene vinylene (OPV) and the final SWCNTs based systems are described.

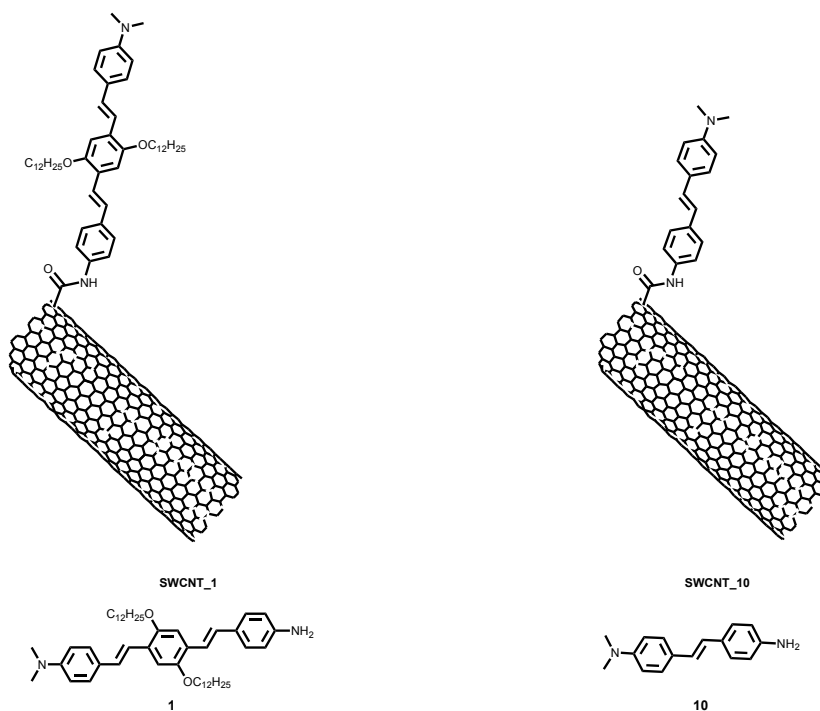


**Figure 3.2:** Schematic representation of the donor-acceptor systems. SWCNTs were functionalized with amino derivatives **1** and **10** to give final systems **SWCNT\_1** and **SWCNT\_10**, respectively.

Commercially available SWCNTs enriched in (7, 6) chirality, were functionalized with two different molecular short chromophores (**1** and **10**) to produce the hybrids complexes **SWCNT\_1** and **SWCNT\_10**, respectively (Figure 3.2). Among all possible covalent functionalizations of SWCNTs, amino bond has been exploited for the linkage of chromophoric derivatives to the SWCNTs [93].

The synthetic pathway adopted for the preparation of 4-((E)-4-((E)-4-aminostyryl)-2,5-bis(dodecyloxy)styryl)-N,N-dimethylaniline **1** is reported in Figure 3.3, whereas compound **SWCNT\_10** has been synthesized according to modified literature procedure [94].

The synthesis of the target compound **1** consisted of a six step protocol. The first bromomethylation reaction [97, 98] of 1,4-bis(dodecyloxy)benzene in the presence of a mixture of paraformaldehyde and HBr in acetic acid gave compound **3** in 63% yield. Subsequent Michaelis-Arbuzov reaction yielded

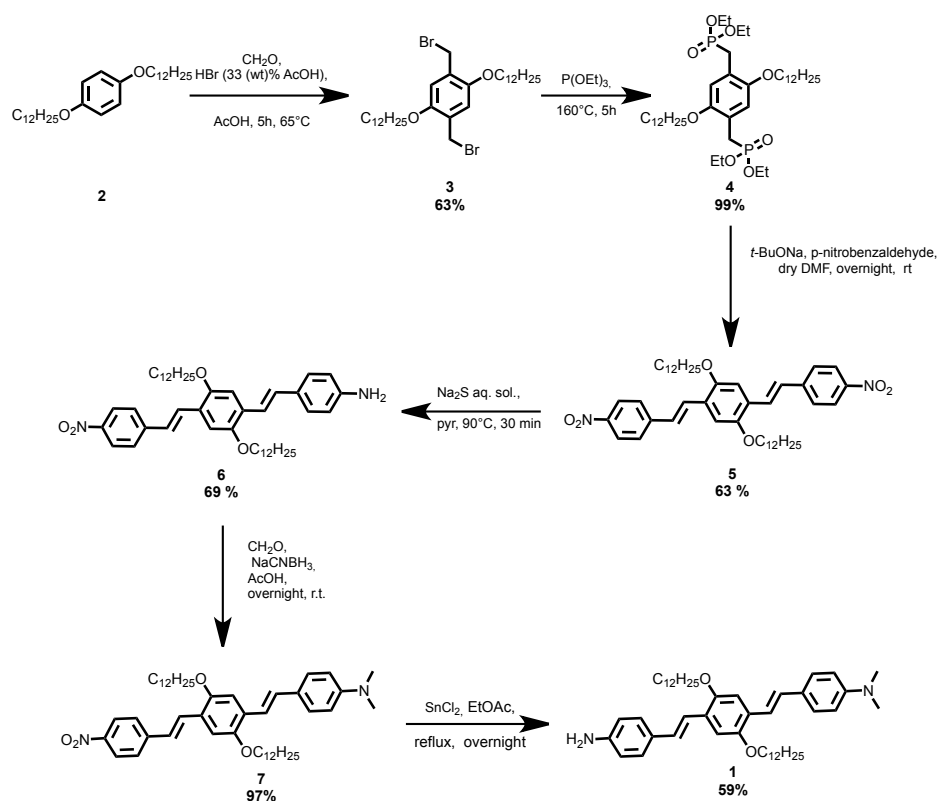


**Figure 3.3:** Synthetic pathway undertaken for the synthesis of target compound **1**. Compounds **3** [95] and **4** [96] were synthesized according to previously reported synthetic protocols.

compound **4** in quantitative yield. The latter was mixed with 2.5 equivalents of p-nitrobenzaldehyde in anhydrous DMF in the presence of *t*-BuONa to obtain dinitrobenzene derivative **5** in 63% of yield. Following mono-reduction reaction of compound **5** in presence of a  $\text{Na}_2\text{S}_2$  aq. sol. gave amino-nitro derivative **6** in 69% yield. Such reaction was obtained following a protocol reported in literature [99]. The synthesis of compound **6** shows that the mono-reduction reaction of a symmetric dinitro compound is very useful in the preparation of extended asymmetric p-conjugated chromophores, as it provides a nitro-amino compound that can be hereinafter selectively protected. To prepare compound **7**, compound **6** was treated with  $(\text{CHO})_n$  and  $\text{NaBH}_3\text{CN}$ , in AcOH [100] and the dimethylamino compound **7** was obtained in 97% yield. Final reduction of nitro group in presence of  $\text{SnCl}_2$  [101] in

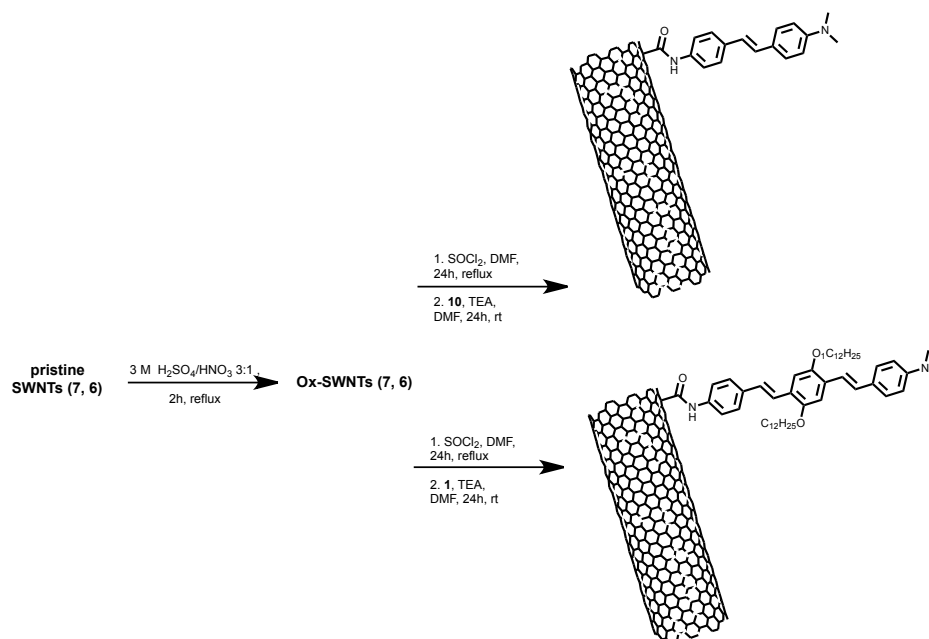


**Figure 3.4:** Synthetic procedure for the covalent functionalization of SWCNT\_1 and SWCNT\_10.

EtOAc gave the target amine **1** (59% yield).

The synthetic pathway adopted for the covalent functionalization of SWCNTs (7,6) with the two different short chromophores **1** and **10** to give complexes SWCNT\_1 and SWCNT\_10, respectively is schematized in Figure 3.4. SWCNTs were firstly oxidized and then functionalized via amidation reaction, one of the most extensively explored covalent modification of oxidized SWCNTs. Ox-SWCNTs were obtained by reaction of pristine CoMoCat SWCNTs (7, 6) with a 3:1 aq. solution of 3M H<sub>2</sub>SO<sub>4</sub> : 3M HNO<sub>3</sub> at 80° for 2 h, following a slightly modified protocol described in literature. The resulting oxidized material was treated with SOCl<sub>2</sub> to give a SWCNT-acid chloride intermediate [102] that was allowed to react with aminostyryl-N,N-dimethylaniline in presence of TEA in DMF to give aminostyryl-N,N-dimethylaniline functionalized SWCNTs enriched in (7, 6) chirality. Ox-SWCNTs as well as target compounds SWCNT\_1 and SWCNT\_10 were characterized by TGA and Raman spectroscopy.

## 3.2 Spectroscopic investigation

### 3.2.1 Optical properties of SWCNTs enriched in (7,6) chirality

Single walled carbon nanotubes are tubular materials formed by the rolling up of graphene sheets. As already seen, they are made of a great variety of chiralities that afford specific absorption and emission peaks. The optical absorption and luminescence spectra are among the most used tools to identify the great variety of semiconducting species (n,m) occurring in a sample. In particular, the photoluminescence mapping (PLM) provides emission spectra recorded as a function of the excitation wavelength. The resulting three-dimensional plot shows the emission intensity maps at a number of excitation wavelengths, all across the visible spectral range. Every region of the map represents the signal of a given (n,m) species. Therefore, the SWCNTs (7,6) were investigated by recording the absorption spectra and the photoluminescence maps, in order to verify the enrichment of this specific chirality. The sample preparation is one of the most important steps for a proper identification. In fact, the absorption spectrum gives information even in the presence of not perfectly dispersed nanotubes, while this is not the case for the photoluminescence maps. The emission data allow to identify the spectral features from the different species only when the nanotubes are in the form of individual entities; accordingly, they require an appropriate dispersion procedure. In our case, the sample preparation consists of a sonication step of 30 min in water, using SWCNTs (7,6) in the presence of a surfactant (sodium dodecil benzene sulfate).

The Vis-NIR optical absorption spectra of SWCNTs (7,6) dispersed in water with SDBS is characterized by absorption bands originated from the transitions between the van Hove singularities [103]. Each chiral (n,m) species absorbs light proportionally to the energy difference between the equal pair valence and conduction bands. The absorption spectrum, reported in Figure 3.5, is made by numerous absorption peaks due to the presence of other species: the sample is in fact only *enriched* in (7,6) chirality. The spectral features are not enough resolved and the closely spaced bands are often not clearly discernible. The peaks are also broadened by electronic coupling

effects due to the presence of aggregated tubes, while the strong background is originated from the light scattering of the nanometric particles [17]. From the data reported in literature [103], SWCNTs (7,6) have two absorption features at 1120 nm and 648 nm, corresponding to the transitions  $E_{11}$  and  $E_{22}$  respectively. From the absorption spectrum the peak at about 650 nm is clearly visible while the second transition, predicted around 1120 nm, is less evident. This is probably due to the overlapping of bands from other species that absorb light in the same region.

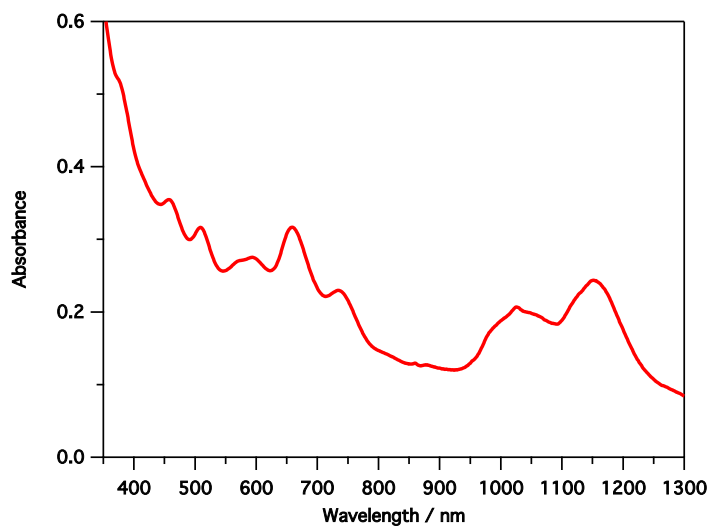


**Figure 3.5:** Absorption spectra of SWCNTs enriched in (7,6) chirality dispersed in water using SDBS as surfactant.

As already seen, the luminescence mapping is one of the most effective methods to characterize the different chiralities (n,m) in a sample of SWCNTs [14]. The emission peaks can be used to identify various SWCNTs species and to evaluate the dispersion degree, while it is not possible to correlate this parameter to quantitative or qualitative properties. This is due to the presence of agents (such as the residual catalyst particles) that may affect the intensity [87]. The PLM (Figure 3.6) shows some emission features with different intensity, the highest is found at 650 nm in excitation and 1120 nm in emission. This transition is unambiguously assigned to SWCNTs (7,6). In fact, the excitation wavelength correspond to the highest transition  $E_{22}$  while the emission maximum is centered at about 1120 nm, which is the

wavelength corresponds to the lowest energy transition  $E_{11}$ . As already seen in 1.2, the emission of the SWCNTs is the result of the transition from the lower energy conduction band to the higher energy valence band.

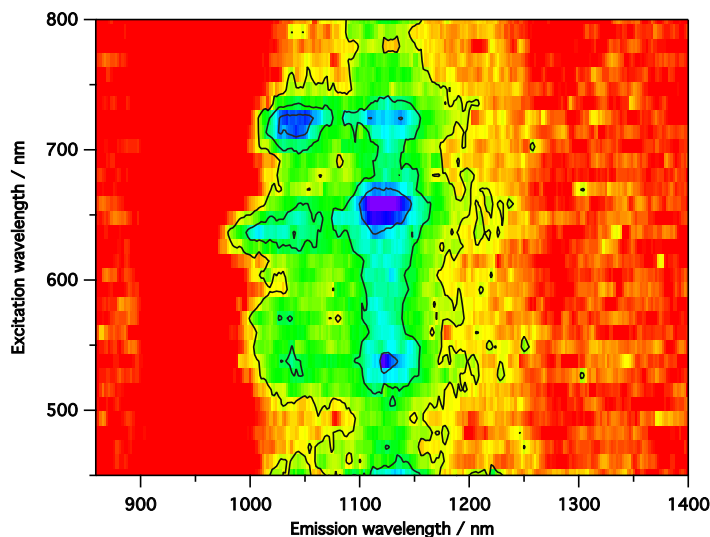


**Figure 3.6:** Photoluminescence mapping of SWCNTs enriched in (7,6) chirality dispersed in water using SDBS as surfactant.

The situation is completely different for the photophysical characterization of SWCNTs that undergo chemical treatment. After the oxidation reaction (described in 3.1) the electronic features of SWCNTs (7,6) are substantially altered due to a rehybridization from  $sp^2$  to  $sp^3$  leading to loss of conjugation. Accordingly, the sample of oxidized-SWCNTs (7,6), dispersed in DMF, are no longer luminescent. The attempts to record emission spectra are reported in Figure 3.7 both at different excitation wavelengths (a) and at always the same wavelength (b). The experimental data demonstrated that the observed peaks are ascribable to scattering effects and not to real optical transitions. In fact, using different excitation wavelengths the signals can not be correlated to the PLM recorded before acid treatment. Moreover, the experimental data recorded using multiple excitation at the same wavelength bring to irriproducibile spectral signal.

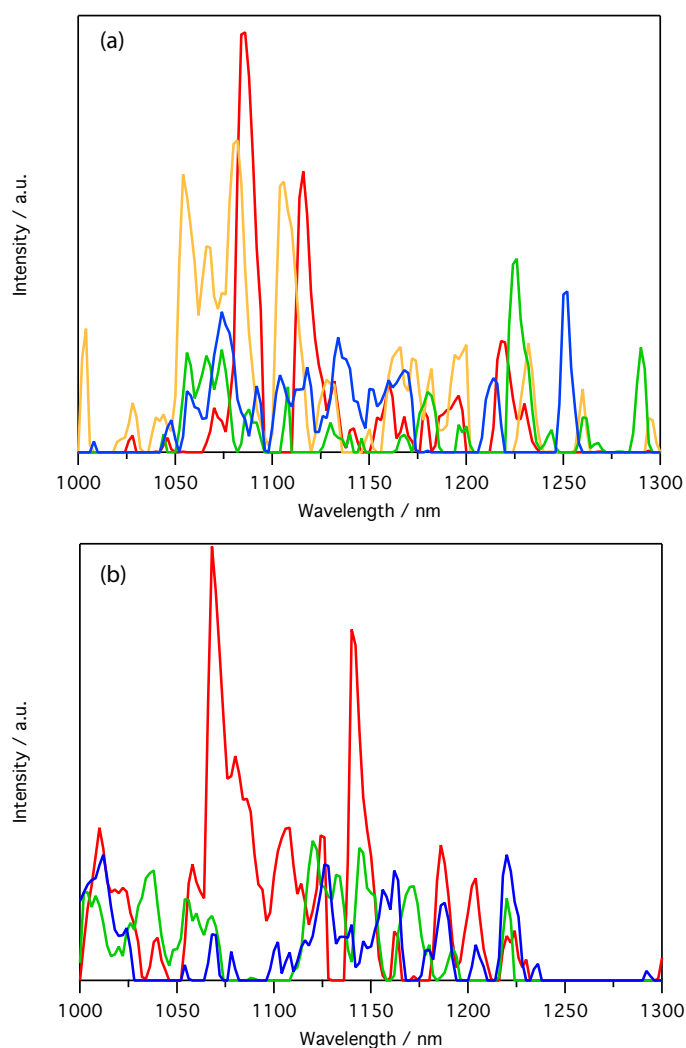


**Figure 3.7:** Attempts to record emission spectra of oxSWCNTs enriched in (7,6) chirality dispersed DMF. (a) Using  $\lambda_{ex}$  450 nm (red),  $\lambda_{ex}$  500 nm (yellow),  $\lambda_{ex}$  550 nm (green) and  $\lambda_{ex}$  600 nm (blue); (b) Using  $\lambda_{ex}$  650 nm for three consecutive experiments.

### 3.2.2 Photophysical Characterization of SWCNTs\_OPV systems

In order to understand the photophysical behavior of **SWCNT\_1** and **SWCNT\_10**, the UV-Vis-NIR absorption and luminescence spectra were

recorded and the excited state lifetimes have been measured. Due to solubilization problems, different solvents were used. For **SWCNT\_1** and its reference **1** DMF afforded the best solubility, while in the case of **SWCNT\_10** and **10** the best dispersion was obtained with the 1,2-dichlorobenzene (oDCB).

The electronic absorption spectra and related key data are reported in Figure 3.8 and Table 4.1. The molar extinction coefficients are calculated only for reference compounds **1** and **10** due to the nature of the carbon nanotubes samples that form dispersions and make it difficult to carry out a quantitative determination. The reference compound **1** absorbs light until 540 nm; its and the absorption spectrum is characterized by the presence of two maxima at 467 nm and 381 nm, respectively. The absorption spectrum of **10** is characterized by the presence of an absorption maximum at 363 nm with a shoulder on the high energy side.

The absorption spectra of **SWCNT\_1** and **SWCNT\_10** are featureless. In particular, it is not possible to distinguish the contribution of the reference molecules due to an overwhelming absorption of the oxSWCNTs in the same spectral region. In addition, the absence of features of SWCNTs is ascribable to a remarkable extent of functionalization. In fact, the electronic structure of SWCNTs is increasingly deteriorated by enhancing the covalent modification; only at low densities of covalent derivatization the  $E_{11}$  and  $E_{22}$  transitions can still be discerned [87, 104].

**Table 3.1:** Absorption maxima of the reference compounds **1** (DMF) and **10** (oDCB).

Sample	Absorption maxima $\lambda_{max}$ , nm ( $\epsilon \times 10^4$ , $M^{-1} \text{ cm}^{-1}$ )
<b>1</b>	467 (5.7), 381 (2.0)
<b>10</b>	363 (3.1)

In order to understand the photoinduced processes between **1** or **10** and SWCNTs the luminescence experiments have been carried out (Figure 3.9 and Table 3.2). All the data are recorded at room temperature in DMF for **1** and **SWCNT\_1** and in oDCB in the case of **10** and **SWCNT\_10**. A comparative method has been applied to calculate the emission quantum yield using  $[\text{Ru}(\text{bpy})_3]_2^+$  as standard.

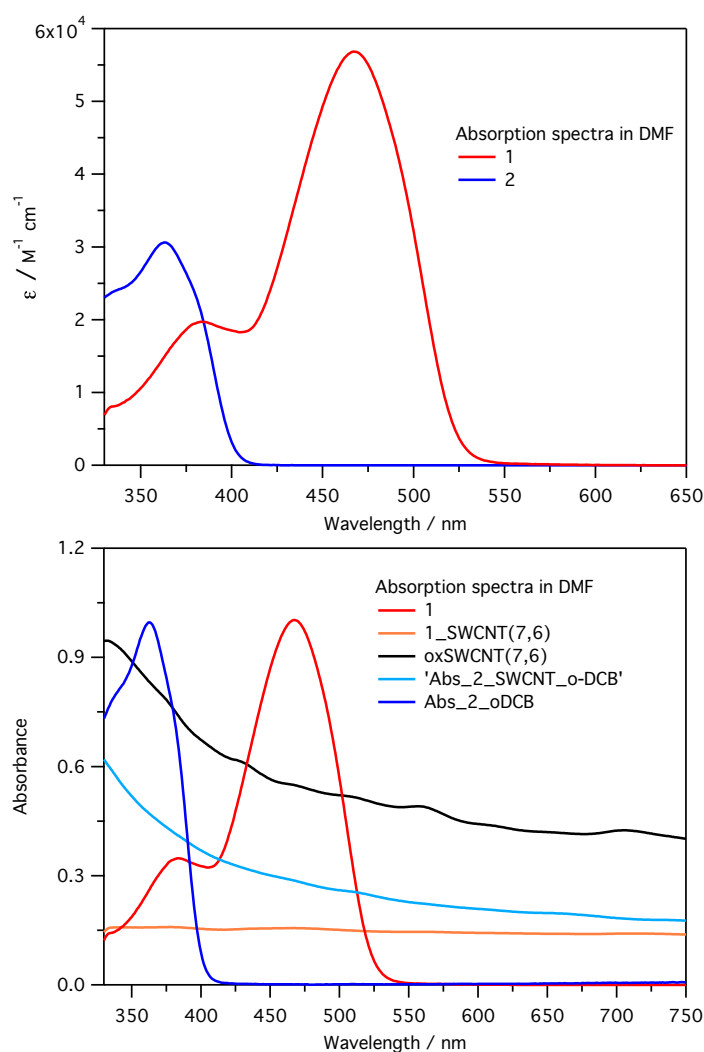


**Figure 3.8:** (a) Molar extinction coefficient of **1** (red) in DMF and **10** (blue) in oDCB ; (b) Absorption spectrum of **1** (red), **SWCNT\_1** (orange), oxSWCNT (7,6) (black) in DMF and of **10** (blue) and **SWCNT\_10** (light blue) in oDCB .

The reference compound **1** exhibits an emission spectrum with a maximum at 510 nm and a fluorescence quantum yield of 38.5%, while the spectrum of dyad **SWCNT\_1** is centered at 530 nm and the emission quantum yield is less than 0.1%. The lack of bathochromic shift, and the emission quenching (estimated to be over 99.7% in **SWCNT\_1** than compared to

the reference compound) indicates a strong electronic interaction between the SWCNTs and **1**. The reference compound **10** exhibits an emission spectrum with a maximum at 430 nm and a fluorescence quantum yield of 12.8%. The maximum of the fluorescence band of **10** in **SWCNT\_10** is substantially blue-shifted and the estimated fluorescence quantum yield is of less than 0.3%, indicating a quenching of almost 97.7% relative to the reference compound. The excitation spectrum of the dyad **SWCNT\_10** is blue shifted compared to **10**, in line with the emission findings. As already mentioned, the photophysical quantitative analysis of samples containing SWCNTs are affected by high uncertainty. The main reasons stem from: (i) in the nanometric nature of the SWCNTs that brings about extensive light scattering and (ii) their insolubility in any solvents and their tendency to form dispersions (when properly treated) that makes it impossible to determine the concentration. In the present case, the estimation of the emission quantum yields of **SWCNT\_1** and **SWCNT\_10** results particularly accurate, as these samples form stable and optical transparent dispersions. Moreover, fluorescence intensities of the reference compounds and the related dyads can be compared, since identical ground state optical densities at the excitation wavelength has been used for both samples.

The fluorescence decay profiles of **1** and **SWCNT\_1** are fitted mono-exponentially; the calculated lifetimes are 1.3 and 1.5 ns, respectively. The lifetime values indicate the presence of very small amounts of free reference compound in **SWCNT\_1**, whereas no other shorter lifetimes are detected. The time-resolved fluorescence lifetime measurements were made with the time-correlated single photon counting spectrometer, which has a time resolution of 40 ps. Therefore, intercomponent photoinduced processes (energy or electron transfer) must take place within 40 ps.

The fluorescence lifetime of **10** is mono-exponential (0.61 ns), while the emission decay of **SWCNT\_10** is bi-exponential with a predominant component of 0.68 ns (72%) and a minor contribution of 3.31 ns (28%). The former could be easily attributed to a small amount of free fluorophore in the dyad (approximately 1.7%). The longest lifetime is more difficult to assign. The most realistic hypothesis is that it is due to the interaction between very closely interacting fluorophores covalently bound to the surface of the SWCNT.

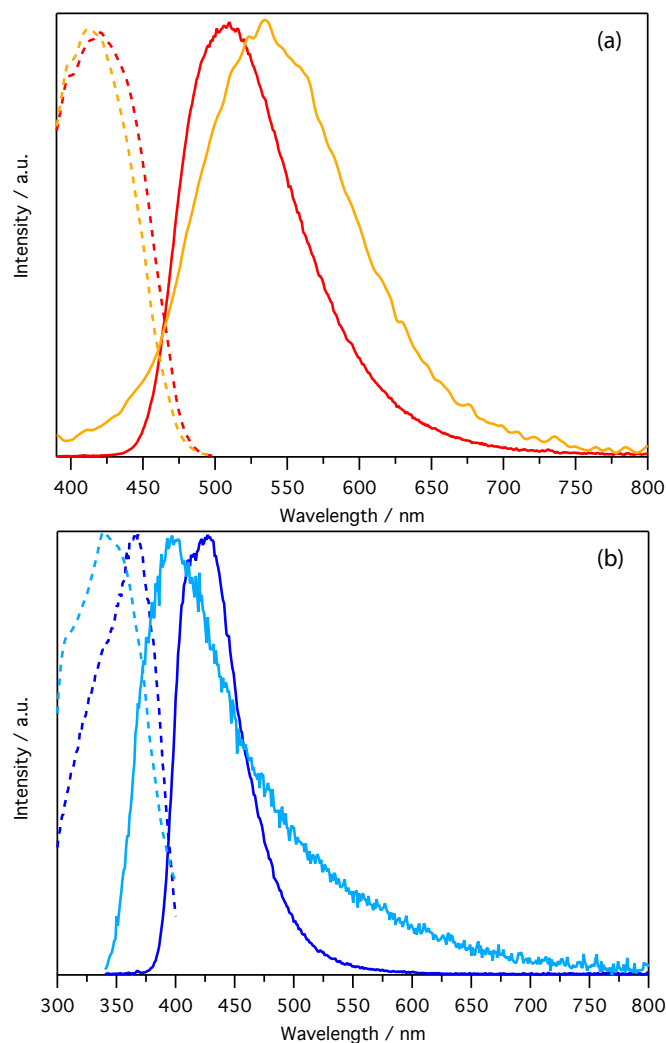


**Figure 3.9:** (a) Excitation spectra  $\lambda_{em}$  520 nm (dashed line) and emission spectra  $\lambda_{ex}$  350 nm (full line) of **1** (red) and **SWCNT\_1** (orange) in DMF; (b) Excitation spectra  $\lambda_{em}$  420 nm (dashed line) and emission spectra  $\lambda_{ex}$  330 nm (full line) of **10** (blue) and **SWCNT\_10** (light blue) in oDCB.

In both cases the samples **SWCNT\_1** and **SWCNT\_10** display a significant quenching of the fluorescence compared to the reference compound **1** and **10**, respectively. These observations must be rationalized taking into account several phenomena that may contribute to the reduction of the lu-

**Table 3.2:** Emission quantum yields and lifetimes.

Sample	$\Phi$ (%)	$\tau$ (ns)
<b>1</b>	38.5	1.37
<b>SWCNT_1</b>	$\leq 0.1\%$ (estimated)	1.51
<b>10</b>	12.8	0.61
<b>SWCNT_10</b>	$\leq 0.3\%$ (estimated)	0.68 (72%) 3.31 (28%)

minescence intensities: i) the light partitioning between the SWCNT and the chromophore units, which is not known with precision; ii) the light scattered by the nanometric dispersed particles; iii) the non-homogeneous functionalization degree (i.e., different fluorophore concentration) of the carbon nanotube scaffolds and iv) the photoinduced processes occurring between the two moieties. All in all, we can be highly confident that the latter phenomenon is the main responsible for the observed luminescence quenching. To elucidate with precision the intimate nature of the photoinduced processes, transient absorption spectroscopy need to be utilized.

### 3.3 Conclusion

This chapter focused on the preparation and physical characterization of the dyads **SWCNT\_1** and **SWCNT\_10** and the respective reference compounds **1** and **10**. In particular, the oxidized SWCNTs enriched in (7,6) chirality were produced by oxidative treatment and then covalently linked through amidation reaction to the dimethylamino distyrylbenzene derivatives **1** and **10**. A new synthetic approach for the preparation of compound **1** has been developed. The positive outcome of the functionalization reaction has been confirmed by TGA analysis and Raman spectroscopy. The references and the SWCNTs-based derivatives were investigated through steady state absorption and emission spectroscopy and through time resolved fluorescence. Photophysical characterization revealed strong electronic interactions between the different components in both dyads. Indeed, intramolecular photoinduced processes have been evidenced by steady-state and time-resolved

luminescence.

Eventually, no convincing proofs were observed to determine the occurring processes (*i.e.*, electron or energy transfer interactions). The formation of dispersions in organic solvents and the nanometric nature of the sample containing-SWCNTs make difficult the quantitative analysis and a more accurate assessment of the phenomena. However, thanks to the peculiarity of these systems to form stable and optical transparent dispersions, sub-picosecond time-resolved measurements will clarify the nature of the photoinduced processes and, in the case of electron transfer, they will evidence fingerprints of the OPV cation.



# Chapter 4

## Hybrid systems based on porphyrin, fullerene and DWCNTs

Fullerenes and carbon nanotubes (CNT) are characterized by similar electronic and mechanical properties. They emerged as materials for photovoltaic devices (PV) thanks to their high charge mobility, strong mechanical resistance as well as thermal and photochemical inertness. Very often attention has been directed to the preparation of multicomponent systems and nanohybrids through the covalent attachment of electron donors -such as ferrocene [105], phthalocyanines [106] or porphyrins [107]- to the nanocarbon scaffold. This approach is related to the strong tendency of CNT and fullerenes to serve as electrons acceptors and hence these materials can be used in PV devices.

Photovoltaic devices convert directly solar energy into electricity [1]. They can be divided into three main classes: inorganic (*e.g.*, silicon-based), organic (*e.g.*, bulk-heterojunction cells) and photoelectrochemical (*e.g.*, dye sensitized solar cells). Among these, organic photovoltaic devices (OPV) are characterized by low fabrication costs, ease of fabrication and mechanical flexibility [108, 109]. Significant results in printable, flexible and foldable photovoltaics can be achieved by employing active layers consisting of donor-acceptor molecular blends, that optimize exciton generation efficiency, dissociation and charge transport. The primary process occurring in OPV

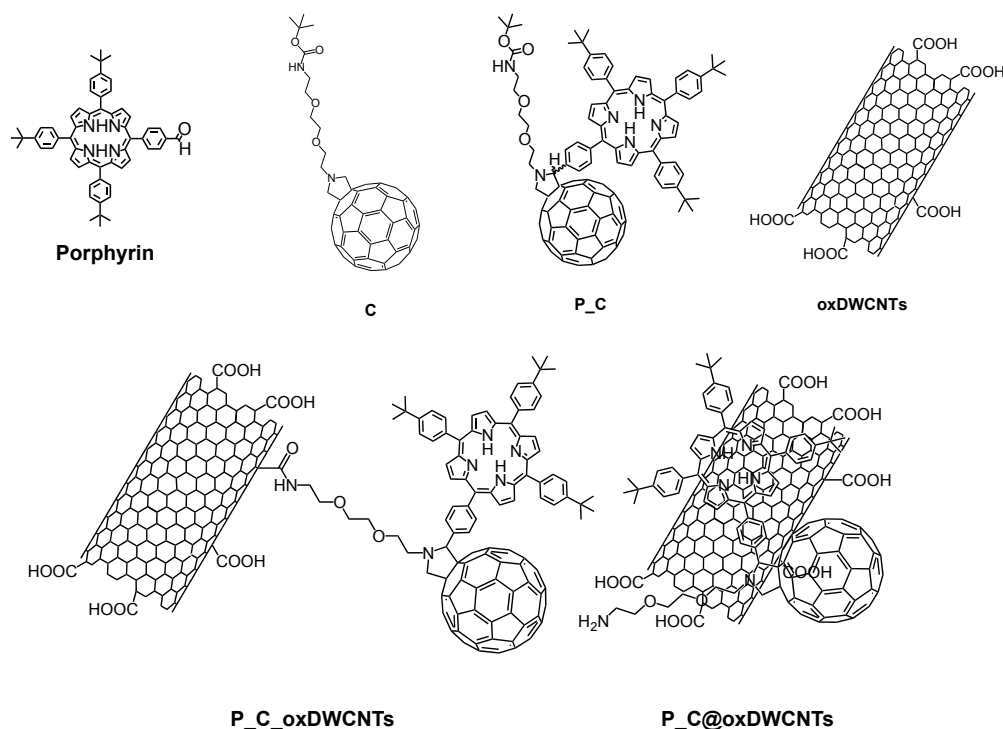


**Figure 4.1:** Schematic representation of the investigated systems: porphyrin (**P**), fullerene (**C**), porphyrin<sub>C<sub>60</sub></sub> (**P\_C**), oxidized-DWCNTs **oxDWCNTs** and porphyrin<sub>C<sub>60</sub></sub>-DWCNTs. In particular, DWCNTs can be covalently link or physisorbed to **P\_C**: **P\_C\_oxDWCNTs** and **P\_C@oxDWCNTs** respectively.

cells is photoinduced charge separation, which occurs at the interface between two distinct materials, an electron-donor (D) and an electron-acceptor (A), blended to form an interpenetrating phase network at the nanometric level [110].

In recent years, the integration of carbon nanotubes (CNTs) into OPV devices has been attempted as a strategy to improve the device performances [91]. However, in order to be embedded into optoelectronic devices, an appropriate chemical modification of the CNTs has to be accomplished, to make them dispersible and processable. For instance, the incorporation of photoactive antenna chromophores (displaying high extinction coefficient in the visible region of the solar spectrum) such as porphyrins [107, 111] is one of

## 4.1 Synthesis of the starting materials and of the hybrid system 67

---

the most popular routes to promote light harvesting and charge-separation and thus photovoltaic conversion in devices.

In this chapter are presented a series of carbon nanohybrids based on double walled carbon nanotubes (DWCNTs),  $C_{60}$  and porphyrins (Figure 4.1). With respect to single-wall counterparts, DWCNTs can be selectively functionalized at the external sidewall without disrupting the internal carbon layer, keeping unaltered the conductive CNT properties. The photophysical investigation of these systems represents the starting point to understand the fundamental photoinduced processes occurring between the involved moieties and to evaluate their potential applicability in organic PV cells [112–114].

### 4.1 Synthesis of the starting materials and of the hybrid systems

In this section, the synthesis of the starting materials and the final porphyrin,  $C_{60}$  and oxDWCNTs based hybrids are described.

The porphyrin derivative (**P**), is based on a tetrapyrrolic core differently substituted at the four *meso*-positions by three solubilizing 4-*tert*-butyl substituents and one benzyl hydroxyl function. The strategy that has been used for the preparation of the porphyrin derivatives is a condensation-type reaction reported in [115]. Therefore, a methyl ester porphyrin derivative has been prepared following the typical Lindsay-based procedure [116] using a 4:3:1 mixture of pyrrole, 4-*tert*-butylbenzaldehyde, and methyl 4-formylbenzoate in the presence of  $BF_3 \cdot OEt_2$ . Consecutive oxidation in presence of 2,3-dichloro-5,6-dicyano-1,4-benzoquinone (DDQ) (Figure 4.2 a) led to methyl ester porphyrin. Monosubstituted porphyrin **P** was then prepared from the precursor with  $LiAlH_4$  (Figure 4.2 b).

The fullerene derivative (**C**), is based on a fulleropyrrolidine where the pyrrolidine nitrogens is linked to the aminoacid based molecule. Aminoacid (2-((2-(2-(2-aminoethoxy)ethoxy)ethyl)amino)acetic acid, (AA) is endowed with long ether chain in order to increase the solubility of the  $C_{60}$  moiety in organic solvents and with a boc-protected amino function. The synthesis of the fulleropyrrolidine is obtained using a 1,3-dipolar cycloaddition to  $C_{60}$  and is schematized in Figure 4.3 [117].

The porphyrin **P** was then reacted with the fullerene and the amino acid

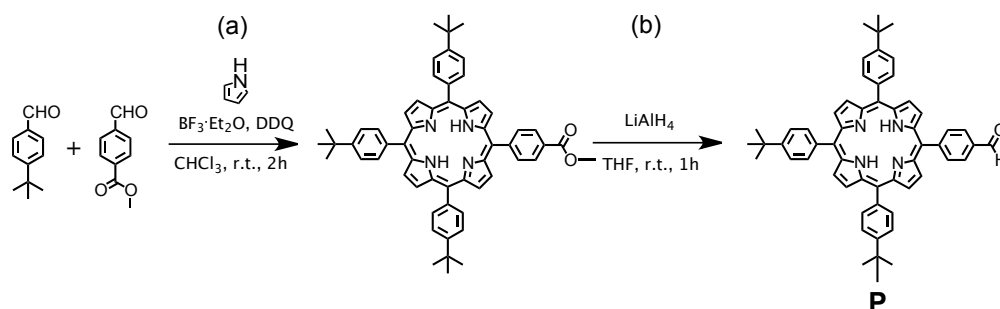


**Figure 4.2:** Synthetic procedure for the preparation of the porphyrin derivative (P).

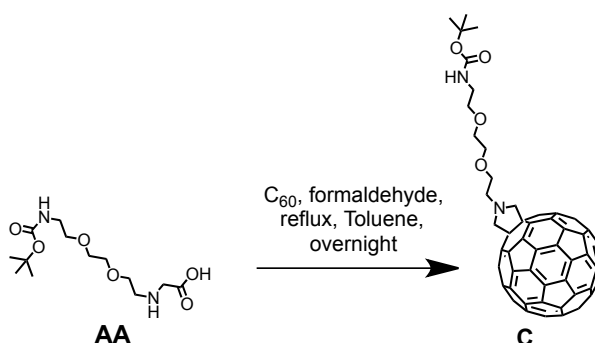


**Figure 4.3:** Schematic representation of the synthesis of the fullerene (C) unit.

(AA) in a 1,3-dipolar cycloaddition-type reaction affording the desired dyad (P\_C) (Figure 4.4). The porphyrin\_C<sub>60</sub> was subsequently deprotected in the presence of trifluoroacetic acid (TFA) and isolated as a greenish-black salt (in 84% yield). The final porphyrin\_C<sub>60</sub>-Amide was then synthesized in order to mimic the amidation reaction on oxDWCNTs. Therefore, the amino function on the porphyrin\_C<sub>60</sub>-Salt was freed in the presence of diisopropylamine (DIPA) and dropped into a solution of O-Benzotriazole-N,N,N',N'-tetramethyl-uronium-hexafluoro-phosphate (HBTU) and acetic acid. The final porphyrin\_C<sub>60</sub>-Amide compound was isolated with an overall yield of

86%.

To obtain the oxidized-DWCNTs (**oxDWCNTs**) the pristine DWCNTs were sonicated for 5 min in an aqueous solution of  $\text{H}_2\text{O}_2$  (15%) and then heated at  $100^\circ$  to open the CNT tips and shorten their length by oxidative attack [118]. Eventually, the resulting material was heated at  $450^\circ$  for 45 min under an external air flux to remove the amorphous carbonaceous materials, decreasing the carbon-coating of the metallic impurities and maximize the tips destruction. A final treatment of 1 h with a 3:1 ratio mixture of aqueous  $\text{H}_2\text{SO}_4$  (95%) and  $\text{HNO}_3$  (65%) solution leads to the final **oxDWCNTs**. This step was performed to increase the number of carboxylic acid functionalities and to remove residues of metallic catalyst. The synthetic procedure is schematized in Figure 4.5.

The synthesis of the **P\_C\_oxDWCNTs** conjugate and of its non-covalent analogous **P\_C@oxDWCNTs** are reported in Figure 4.6. The chosen strategy to covalently graft **P\_C** adducts onto the external walls of carbon nanotubes involved an amidation reaction between the porphyrin\_ $\text{C}_{60}$ -Salt and the oxidized-DWCNTs. Therefore, ox-DWCNTs were mixed in DMF with porphyrin\_ $\text{C}_{60}$ -Salt in the presence of HBTU, affording the covalent **P\_C\_oxDWCNTs** conjugate (Figure 4.6 a). Similar conditions were employed to prepare the non-covalent **P\_C@oxDWCNTs** conjugate, used as reference derivative. In this case, ox-DWCNTs dispersed in DMF were reacted with porphyrin\_ $\text{C}_{60}$ -Salt without the presence of HBTU (Figure 4.6 b).

## 4.2 Photophysical studies

UV-Vis absorption, luminescence and excited state lifetimes data have been obtained at room temperature in two solvents of different polarity (*i.e.*, toluene and benzonitrile). Electronic absorption spectra and related key data are reported in Figure 4.7 and Table 4.1. The absorption spectrum of pristine **P** is extended over the entire visible region and is characterized by the presence of the Soret band, centered at 422 nm, and the weaker Q-bands from 515 nm up to about 750 nm. The absorption **C** is predominantly localized in the UV portion of the spectrum, in particular the fullerene absorbs light from about 450 nm to smaller wavelength. The dyad **P\_C** is characterized

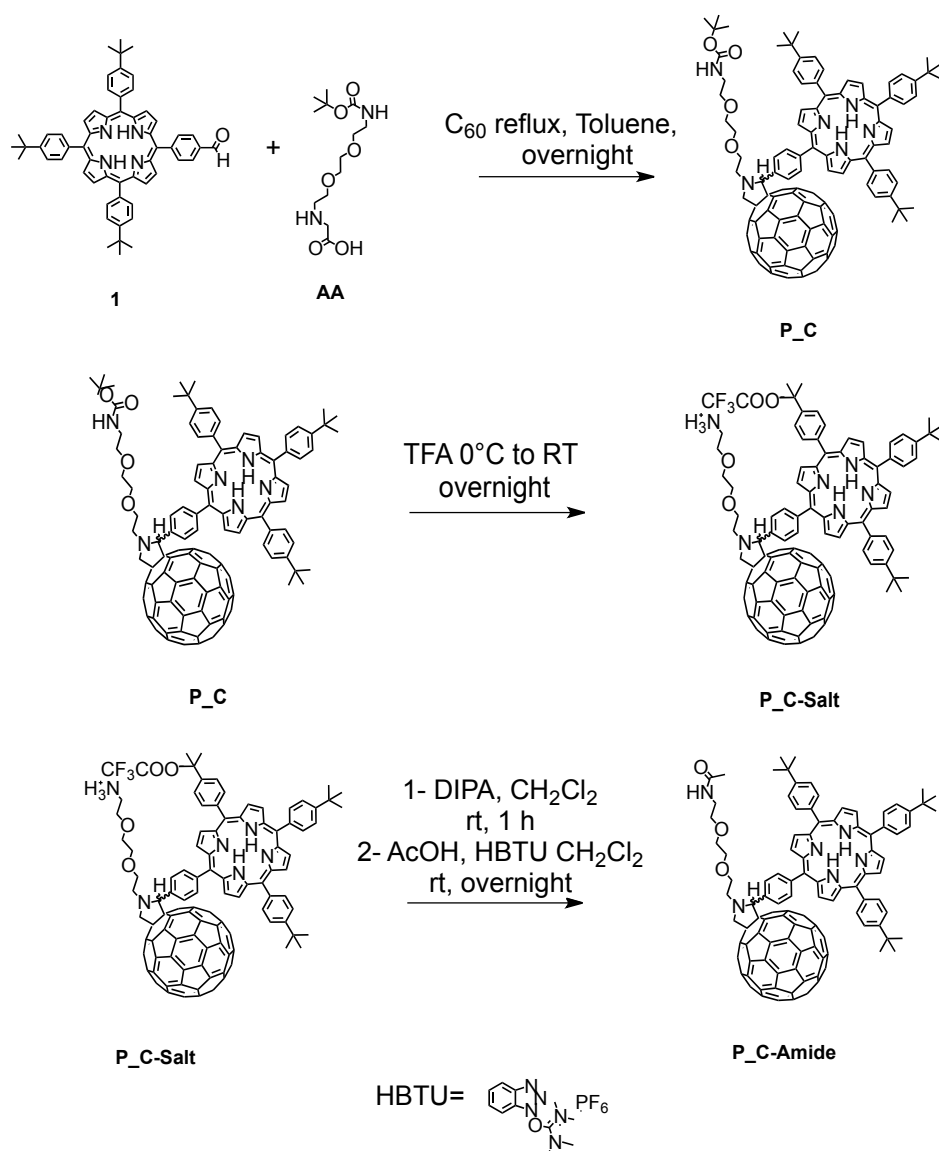


**Figure 4.4:** Synthetic procedure for the preparation of the porphyrin<sub>C<sub>60</sub></sub> derivative (P\_C).

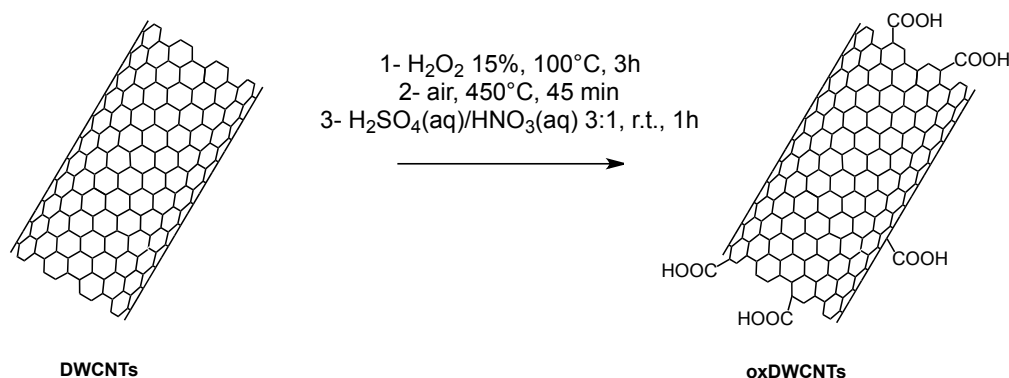


**Figure 4.5:** Synthetic procedure for the oxidation of DWCNTs **oxDWCNTs**.

by an absorption spectrum that spans from 300 nm to over 750 nm. In particular, the features of the porphyrin unit (*i.e.*, Soret band at 422 nm and the Q-bands at lower energy) are observed between 390 and 750 nm. On the other hand, in the UV region, the absorption is mostly attributable to the fulleropyrrolidine moiety. It is important to emphasize that the absorption spectrum of the dyad is exactly the sum of the individual components **P** and **C**, indicating negligible electronic interactions between the C<sub>60</sub> and the porphyrin in the ground state.

The samples containing the oxDWCNTs exhibit absorption spectra that are extended from the UV to the NIR region; both hybrid materials **P\_C\_oxDWCNTs** and **P\_C@oxDWCNTs** show the porphyrin Soret band at 422 nm, whereas the weaker Q-bands are not discernible due to the overwhelming absorption of oxDWCNTs. The absorption coefficients are calculated only for the samples without the oxDWCNT moiety, due to the tendency of the carbon nanotubes to form dispersions and prevent a quantitative assessment (Figure 4.7 a).

The fluorescence spectra, recorded with excitation at 400 nm, are reported in Figure 4.8. The porphyrin exhibits an emission band with maxima at 658 and 724 nm and a fluorescence quantum yield of 7.1% and 8.1% in toluene and benzonitrile respectively, as determined by the comparative method with [Ru(bpy)<sub>3</sub>]<sub>2</sub><sup>+</sup> as standard. The **C** sample has a fluorescence maximum at 715 nm with a quantum yield of 0.04% in toluene and 0.08% in

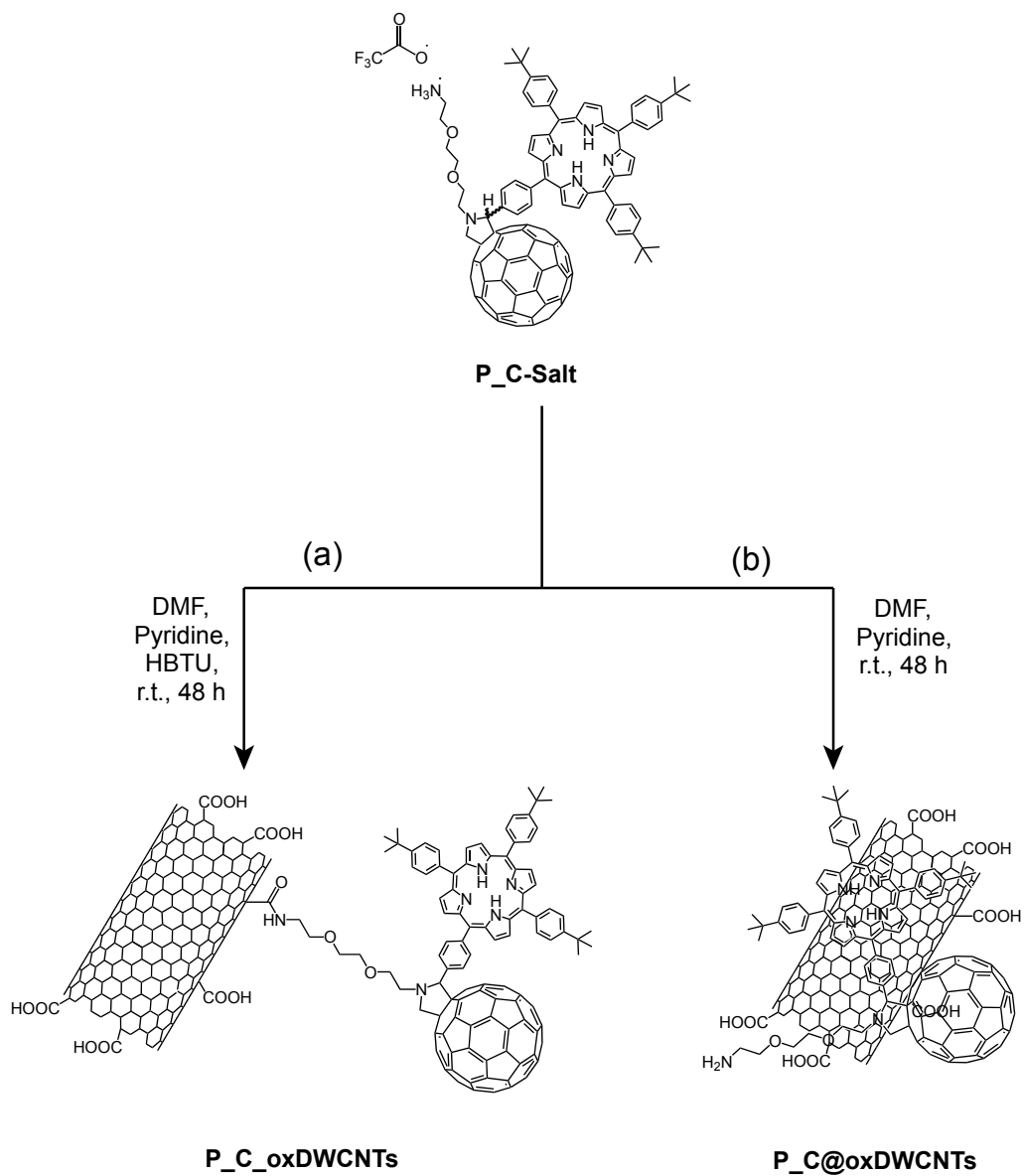


**Figure 4.6:** Synthetic procedure for the preparation of the porphyrin, fullerene and DWCNTs derivative: **P\_C\_oxDWCNTs** and **P\_C@oxDWCNTs**.

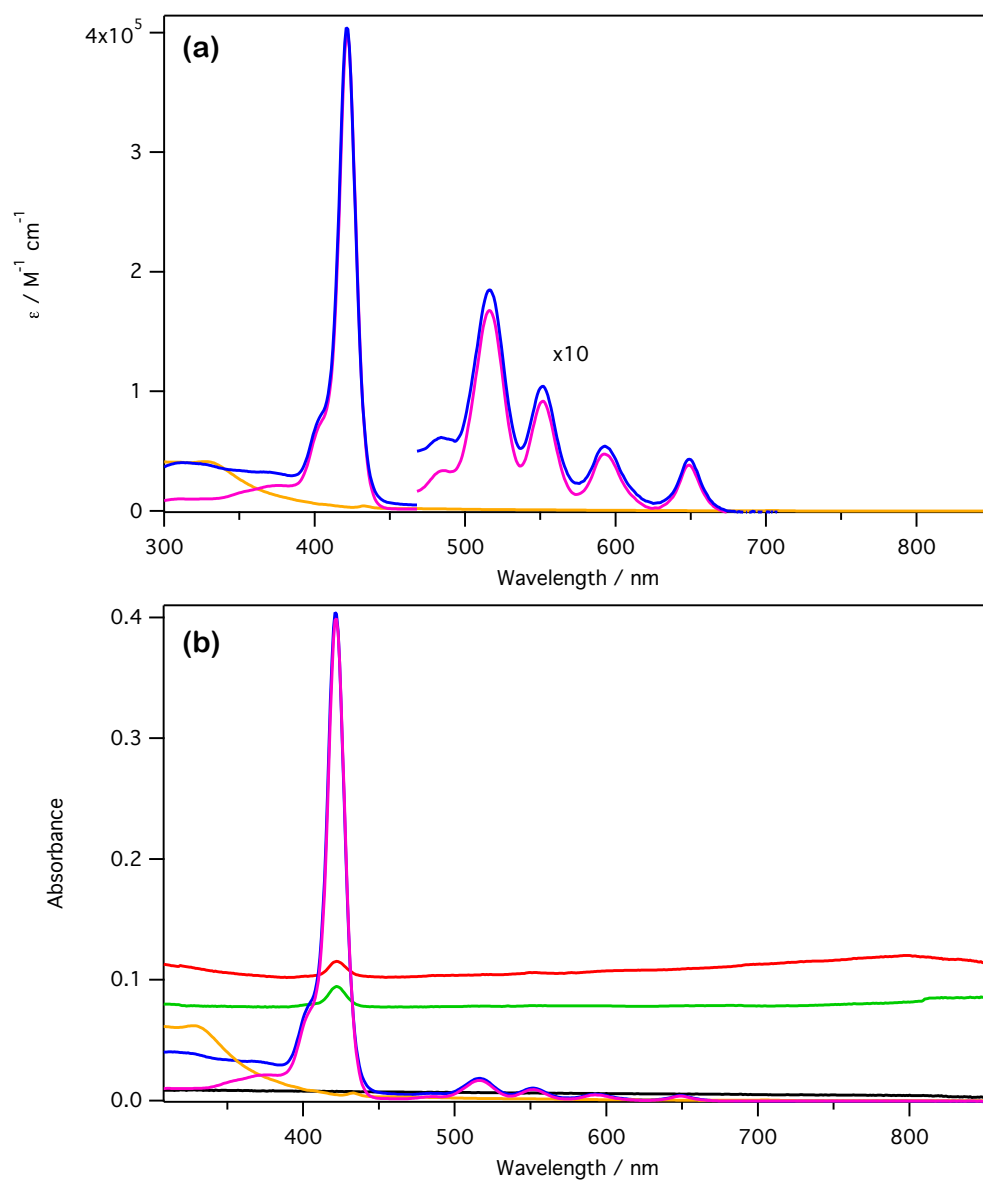


**Figure 4.7:** (a) Molar extinction coefficient calculated for **P** (magenta), **C** (orange), **P\_C** (blue); (b) Absorption spectra of **P** (magenta), **C** (orange), **P\_C** (blue), **oxDWCNTs** (black), **P\_C\_oxDWCNTs** (red) and **P\_C@oxDWCNTs** (green) in toluene.

**Table 4.1:** Absorption maxima ( $\lambda_{max}$ ) of the reference compounds **P** and **C**, and the hybrids **P\_C**, **P\_C\_oxDWCNTs** and **P\_C@oxDWCNTs** in Toluene.

Sample	Absorption maxima $\lambda_{max}$ , nm ( $\epsilon \times 10^5$ , $M^{-1} cm^{-1}$ )
<b>P</b>	422 (4.0), 517 (0.2), 522 (0.1), 594 (0.05), 649 (0.04)
<b>C</b>	433 (0.4)
<b>P_C</b>	422 (4.0), 517 (0.2), 522 (0.1), 594 (0.05), 649 (0.04)
<b>P_C_oxDWCNTs</b>	422
<b>P_C@oxDWCNTs</b>	422

benzonitrile. Since the emission band of the fullerene extends beyond the instrumental limit of the UV-Vis detector, the IR detector was also used. The entire luminescence spectrum of the fullerene molecule extends from 700 nm to over 900 nm as shown in Figure 4.9.

The dyad exhibits a fluorescence band that is totally superimposable in shape to that of the porphyrin in both solvents (Figure 4.8) while it is not possible to detect a signal from the fullerene unit. This is not surprising as the fluorescence quantum yield of the fullerene is two orders of magnitude lower than that of the porphyrin and its luminescence band is largely superimposed to the emission band of the porphyrin. In the dyad, the porphyrin fluorescence intensity is quenched (by about 96% when compared to the porphyrin reference alone in both solvents (Table 5.3); even in the presence of a quenched porphyrin the signal from the fullerene is not present.

The hybrid systems **P\_C\_oxDWCNTs** and **P\_C@oxDWCNTs** exhibit a fluorescence band identical in shape to that of the porphyrin reference compound. The emission quantum yield could not be evaluated quantitatively due to the presence of the CNT units that absorb and scatter the exciting light. However, the emission spectra recorded with identical absorbance at the excitation wavelength display an intensity similar to the **P\_C** dyad. Moreover, the excitation spectra of all the compounds recorded at 650 nm in the spectral interval between 300 and 600 nm unambiguously show the porphyrin spectral features (Figure 4.10).

The excited state lifetimes in toluene of **P** and **C** are 9.40 ns and 1.48

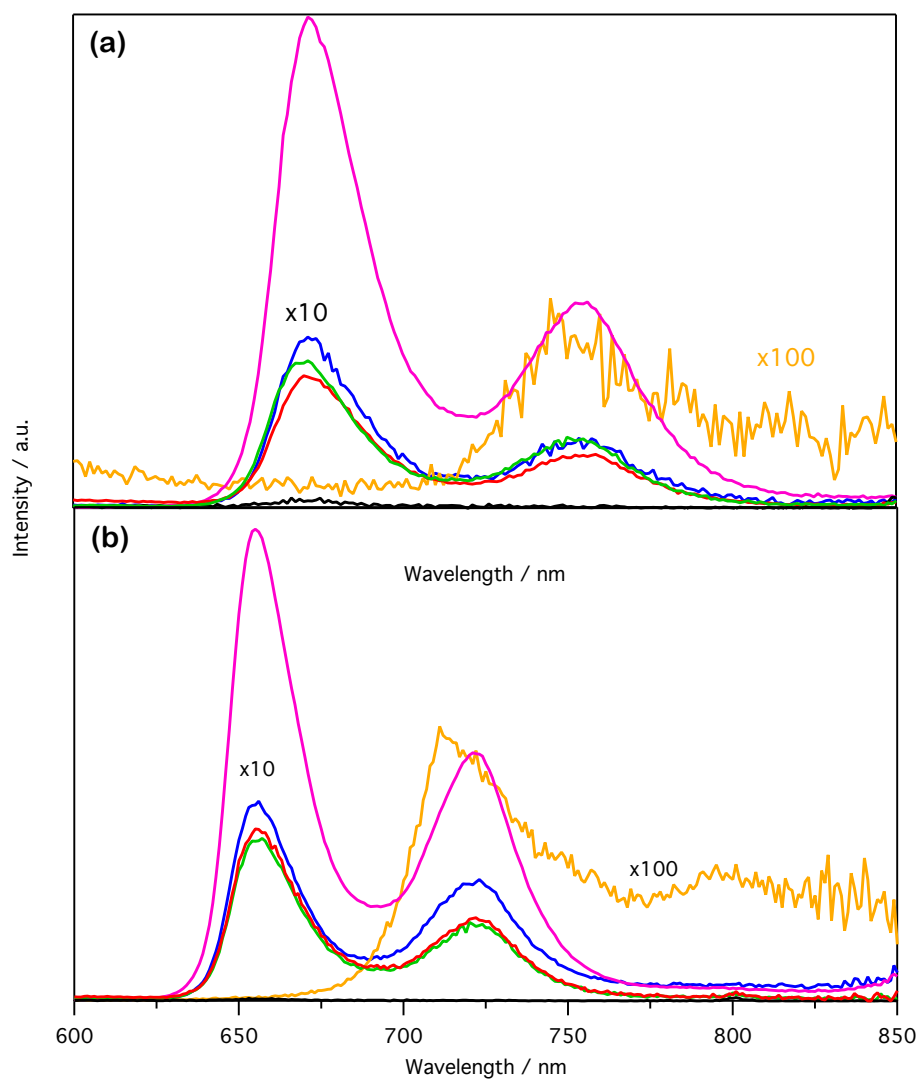


**Figure 4.8:** Emission spectra recorded at  $\lambda_{ex}$  420 nm of **P** (magenta), **C** (orange), **P\_C** (blue), **oxDWCNTs** (black), **P\_C\_oxDWCNTs** (red) and **P\_C@oxDWCNTs** (green) (a) in toluene and (b) in benzonitrile at 298 K.

ns respectively, whereas in the dyad **P\_C** three lifetimes are determined in both solvents. The longest one (7.73 ns in toluene) is largely prevailing (> 50%) and is somewhat similar to that of the free porphyrin while the other two lifetimes are about 1 ns and <100 ps, the latter being attributable to

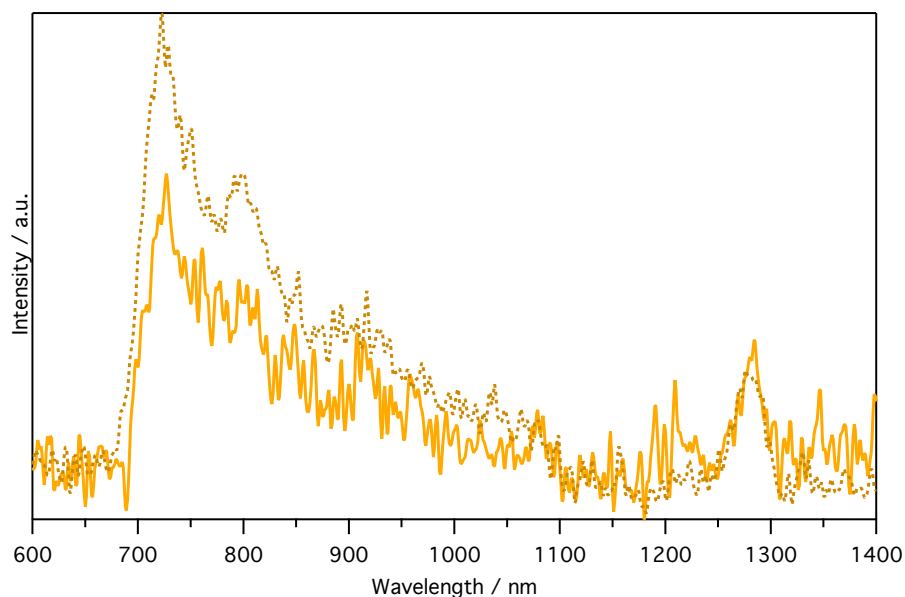


**Figure 4.9:** Emission spectra of **C** in benzonitrile (full line) and toluene (dotted line); recorded using  $\lambda_{ex}$  330 nm; NIR sensitive detector.

the quenched porphyrin.

The hybrids **P\_C\_oxDWCNTs** and **P\_C@oxDWCNTs** show different behavior depending on the solvent: in toluene the decay profiles are mono-exponential and the lifetime values are similar to those of the porphyrin reference compound. In benzonitrile, the decays are fitted as bi-exponential and the values obtained are comparable to the lifetime of the porphyrin and a fullerene references respectively. The emission lifetime values are collected in Table 5.3.

The reduction of the porphyrin fluorescence intensity that is experimentally observed in **P\_C\_oxDWCNTs** and **P\_C@oxDWCNTs** taking into account different aspects: i) light partitioning between the three units (porphyrin, fullerene and ox-DWCNTs), with a remarkable portion of the incoming photons likely captured by the carbon nanotube; ii) light scattering (excitation and/or emission) due to the presence of nanometric particles; iii) different functionalization degree (*i.e.*, different porphyrin concentration) of the hybrids and iv) photoinduced quenching processes occurring between the moieties. All of the above factors can explain the observed reduction of the

luminescence intensities.

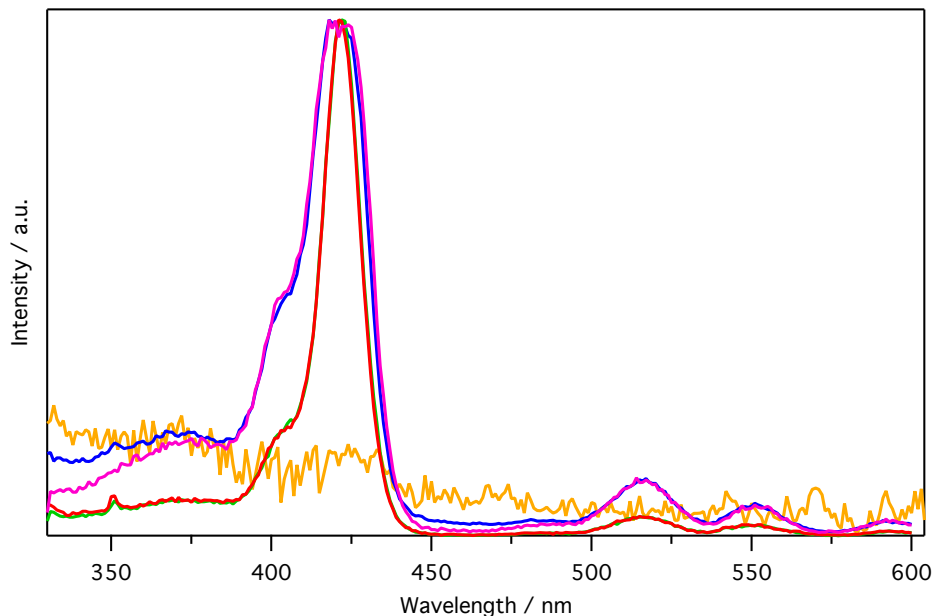
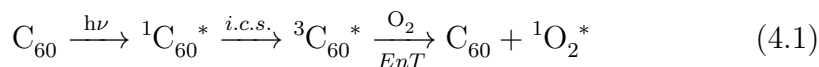


**Figure 4.10:** Normalized excitation spectra at  $\lambda_{em}$  650 nm in toluene of **P** (magenta), **C** (orange), **P\_C** (blue), **P\_C\_oxDWCNTs** (red) and **P\_C@oxDWCNTs** (green).

To get some more insight into the nature of the photoinduced processes the formation of the triplet excited states can be traced. The formation of porphyrin and/or fullerene triplets can be observed by detecting the presence of sensitized singlet oxygen ( $^1\text{O}_2^*$ ) luminescence at 1270 nm. Upon light irradiation, fullerene and porphyrin generate excited singlet molecular oxygen  $\text{O}_2$  ( $^1\Delta_g$ ) with high efficiency. The sensitization occurs through triplet-singlet electron-exchange energy transfer [119]. The singlet-triplet transitions are typically spin forbidden, but the triplet nature of the ground state of the molecular oxygen makes them allowed. Upon photoexcitation of the sensitizer (porphyrin or fullerene) the lowest singlet excited state produces the triplet excited state via intersystem crossing (i.c.s.). The triplet state reacts with the singlet oxygen that deactivates back to the ground state giving rise to NIR-emission [119]. The signal at 1270 nm is one of the most powerful tools to monitor the photosensitization process. A schematic representation of the singlet oxygen sensitization process is reported in 4.1.

**Table 4.2:** Emission quantum yields and excited state lifetimes in toluene and benzonitrile solutions at 298 K.

Sample	Toluene		Benzonitrile	
	$\Phi$ (%)	$\tau$ (ns)	$\Phi$ (%)	$\tau$ (ns)
<b>P</b>	7.10	9.40	8.11	10.0
<b>C</b>	0.04	1.48	0.08	1.48
<b>P_C</b>	0.23	1.11 (30%)	0.28	0.93 (14%)
		7.73 (53%)		8.63 (70%)
		0.07 (17%)		0.06 (16%)
<b>P_C_oxDWCNTs</b>	N.C.	8.82	N.C.	0.98 (47%)
				9.56 (53%)
<b>P_C@oxDWCNTs</b>	N.C.	8.94	N.C.	0.97 (46%)
				8.53 (54%)



By monitoring the singlet oxygen formation, it is possible to obtain an indirect estimation of the triplet state generated by the porphyrin and/or fullerene in the dyads and in the hybrids. Experimentally, all the samples were prepared matching the absorbance values at the excitation wavelength and keeping constant all the experimental parameters in order to compare directly the amount of sensitized singlet oxygen. Notably, the singlet oxygen formation in **P\_C** dyad is dramatically solvent dependent [119] and relative comparisons can be made only in the same medium. In toluene (Figure 4.11 a), both in the references and the examined samples, the singlet-oxygen sensitization is quantitative, suggesting that the final sinks of intercomponent processes upon photoexcitation are the triplet states. By contrast, in benzonitrile (Figure 4.11 b), the oxygen sensitization in **P\_C** is lower if compared to the reference systems (*i.e.*, pristine porphyrin and  $\text{C}_{60}$ ), suggesting the population of other excited states, presumably charge-separated states. In the oxDWCNTs-based samples no singlet oxygen sensitization is detected in both solvents (see Figure 4.11 c and d); this observation is probably due to the same reasons as listed to rationalize the quenching of the fluorescence

(see above).

## 4.3 Conclusion

In this chapter, systems based on porphyrin, fullerene and DWCNTs are presented. The synthetic procedures of all the compounds are described, along with an extensive photophysical characterization.

The dyad shows a solvent dependent behavior: in toluene the porphyrin quenching is attributable to an energy transfer process to the fullerene sub-unit while in benzonitrile occurrence of electron transfer is evidenced. As already demonstrated for similar compounds [120, 121], a non-polar protic solvent such as toluene promotes energy transfer. In our case the experimental data evidence a reduction of the porphyrin fluorescence quantum yield and the detection of a three-exponential decay associated to the quenched porphyrin, the sensitized fullerene, and to a small percentage of free porphyrin impurities ( $\leq 1.5\%$ ). The singlet oxygen sensitization measurements clearly show that there are no differences in the amount of singlet oxygen that has been sensitized by the porphyrin, the fullerene and the dyad in toluene, while in benzonitrile the **P\_C** system no longer shows a quantitative sensitization, suggesting electron transfer. The photophysical characterization of the compounds containing the oxDWCNTs can be only qualitative, as the presence of suspended nanotubes inside the dispersion prevents a reliable quantitative characterization with optical spectroscopy. The data collected show that the porphyrin unit is quenched and the associated lifetimes are mono-exponential in toluene and bi-exponential in benzonitrile. In toluene, the observed lifetime is attributable to some free porphyrin, while in benzonitrile the bi-exponential trend is associated to the decays of the porphyrin and the fullerene. Singlet oxygen sensitization in samples with nanotubes cannot be quantified due to the massive occurrence of light scattering. Moreover, the formation of not perfectly transparent dispersions and the presence of free porphyrin, hampers the investigation through laser transient absorption spectroscopy due to both light scattering and the prominence of the spectroscopic fingerprints of porphyrin and fullerene units that are expected to mask any possible signal that may indicate intercomponent interaction. However, the only experimental measurements that can be consistently carried out

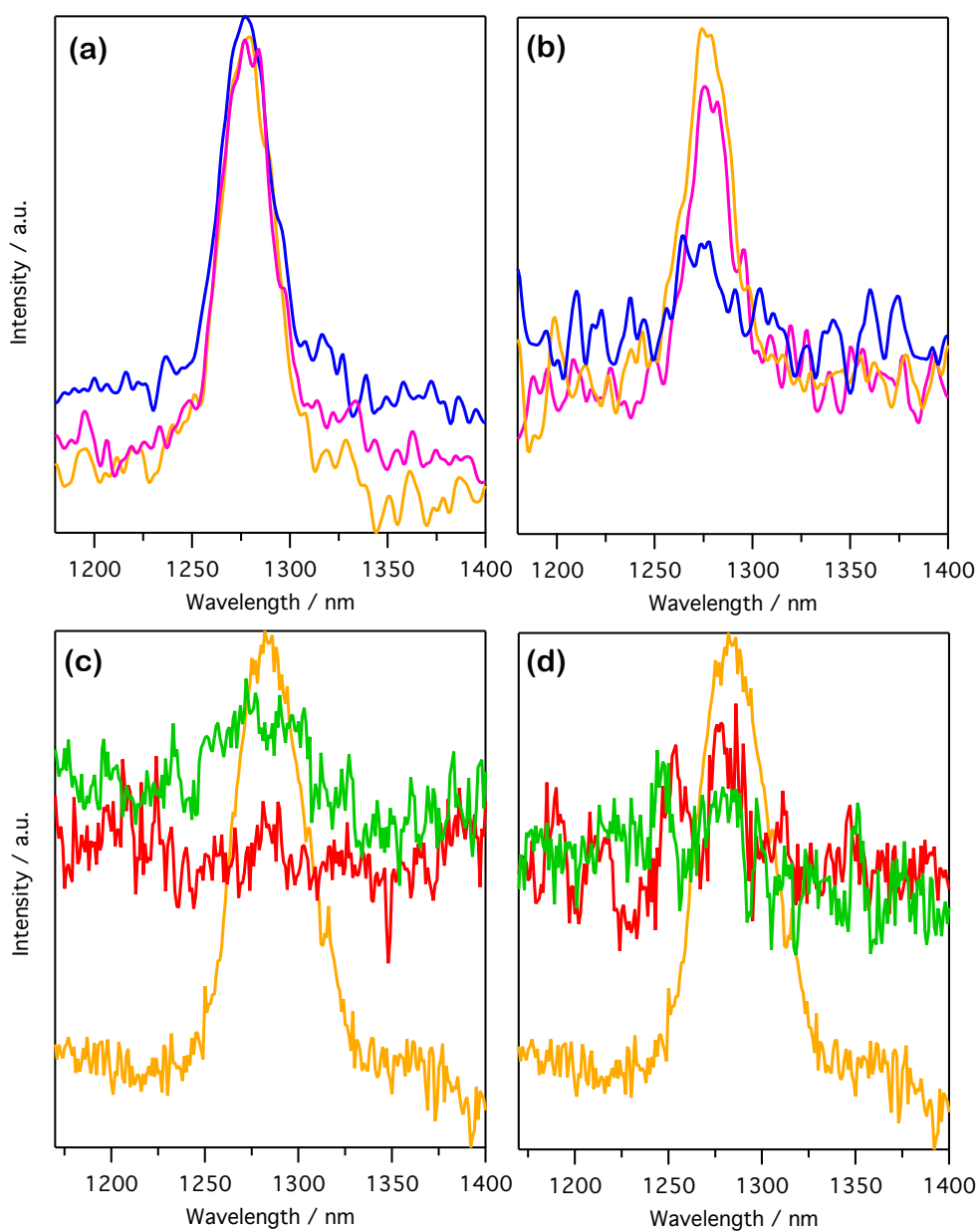


**Figure 4.11:** Sensitized singlet oxygen luminescence spectra recorded at  $\lambda_{ex}$  420 nm. **P** (magenta), **C** (orange), **P\_C** (blue) (a) in toluene and (b) in benzonitrile. **C** (orange), **P\_C\_oxDWCNTs** (red), **P\_C@oxDWCNTs** (green) (c) in toluene and (d) in benzonitrile.

---

-essentially the emission spectra- do not evidence significant differences between the behavior of the dyads covalently linked or physioadsorbed to the oxDWCNTs. Moreover, no significant differences are observed between the hybrids containing the oxDWCNTs and the individual **P\_C** dyad. In order to evaluate the potential properties of the porphyrin-fullerene-DWCNT derivatives they will be tested in photovoltaic devices. They could behave like versatile, interpenetrating unidimensional hole-extracting materials as well as electron accepting units and conductive networks.



## Chapter 5

# Homoleptic and heteroleptic Ru(II) complexes with extended phenanthroline-based ligands

In this chapter, four Ru(II) complexes of general formula  $[\text{Ru}(\text{PT})_3]_2^+$ ,  $[\text{Ru}(\text{NT})_3]_2^+$ ,  $[\text{Ru}(\text{PT})(\text{bpy})_2]_2^+$  and  $[\text{Ru}(\text{NT})(\text{bpy})_2]_2^+$ , where **PT** is 10,13-bis((triisopropylsilyl)ethynyl) dipyrido[3,2-*a*:2',3'-*c*]phenazine, **NT** is 10,15-bis((triisopropylsilyl)ethynyl) benzo[*i*]dipyrido[3,2-*a*:2',3'-*c*] phenazine and bpy is 2,2'-bipyridine (the ligands, the homoleptic and the heteroleptic complexes are reported in Figure 5.1) are presented [122]. The electrochemical and photophysical properties with the aid of DFT and TD-DFT theoretical methods have been studied, in order to evaluate their potential for applications on solar energy conversion systems [123]. Additionally, photophysical data for Ru(II) homoleptic complexes with extended ligands have been explored [124].

1,10-Phenanthroline exhibits peculiar chemical properties and, along with its many derivatives, it constitutes an extensively studied family of molecules both in the area of organic and inorganic chemistry [1,2]. Without a rational functionalization, 1,10-phenanthroline results poorly luminescent but, using substituents at specific ring positions or extending  $\pi$ -delocalization, it is possible to prepare a large number of highly luminescent phenanthroline

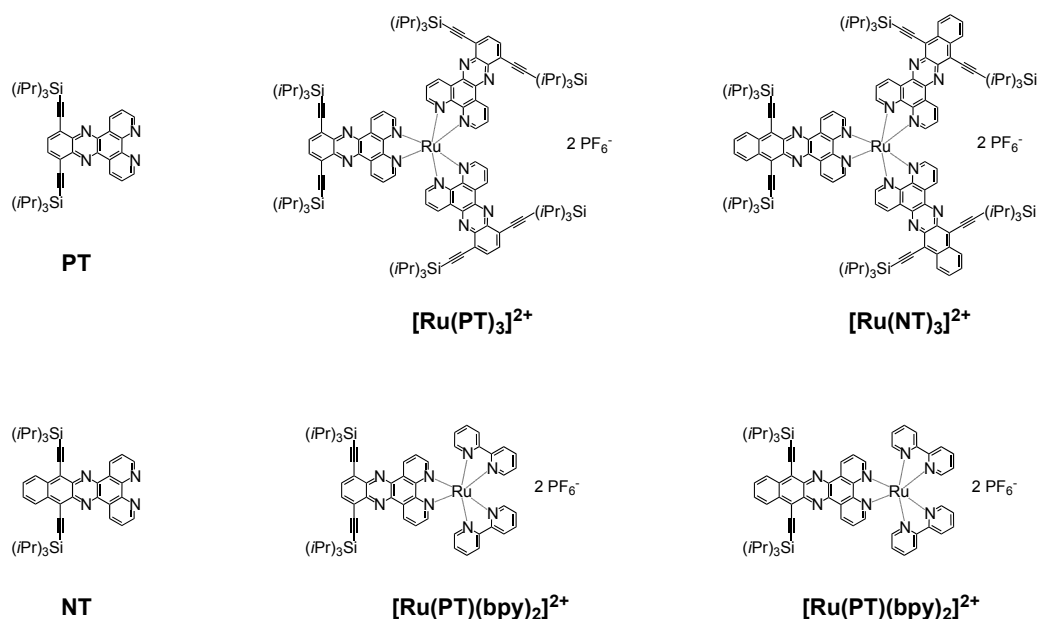


**Figure 5.1:** Schematic representation of the Ru(II) complexes and the ligands.

derivatives [2-5]. A further possibility is provided by the simple protonation of phenanthroline ligands in solution, which enables facile and reversible tuning of luminescence [3,8,9]. Moreover, taking advantage of chelating character, 1,10-phenanthroline has been utilized to prepare numerous luminescent complexes with transition metals (*e.g.*,  $\text{Zn}^{2+}$ ,  $\text{Cu}^+$ ,  $\text{Re}^+$ ,  $\text{Ru}^{2+}$ ,  $\text{Os}^{2+}$ ,  $\text{Ir}^{3+}$ ) and lanthanide ions (*e.g.*,  $\text{Eu}^{3+}$ ,  $\text{Tb}^{3+}$ ). [6,7]

**PT** and **NT** are alkynyl derivatives [125] of dipyrido[3,2-*a*:2',3'-*c*]phenazine (dppz) and benzo[*i*]-dipyrido[3,2-*a*:2',3'-*c*]phenazine (dppn), respectively, two extended phenanthroline-based ligands that have been previously utilized for the preparation of Ru(II) complexes, and then used in correlation with DNA [126–132] or carbon nanotubes [133], due to their tendency to form  $\pi$ -stacking interactions. Such complexes were found to exhibit low-lying electronic levels of both metal-to-ligand charge transfer (MLCT) and ligand-centered nature (LC) [134]. They are usually poor emitters, but luminescence data reported in literature are scattered [129, 130]. The purpose of this chapter is (i) to illustrate the photophysical peculiarities of the homoleptic and heteroleptic Ru(II) complexes involving extended phenanthroline ligands through the

support of DFT and TD-DFT calculations; (ii) to provide exhaustive photo-physical data for Ru(II) homoleptic complexes with **PT** and **NT** ligands, a relatively elusive topic in current literature; (iii) to evaluate the applicability of these complexes for applications related to solar energy conversion.

## 5.1 Synthesis of the ligands and the respective Ru(II) complexes

The preparation of the ligands and of the corresponding Ru(II) complexes is reported in Figure 5.2.

The synthesis started with the preparation of both ligands, in particular the oxidation reaction of 1,10-phenanthroline is obtained using potassium bromate to provide Phendione. The two aromatic o-diamines, namely PhTIPS [135] and NQTIPS [136], were synthesized by following procedures of Bunz et al.. The dipyrrophenazine **PT** is obtained as a bright yellow solid in 66% yield through a condensation reaction of PhTIPS with Phendione, whereas NQTIPS afforded benzodipyrrophenazine **NT** as a bright red solid in 82% yield. Both ligands precipitated from the ethanol solutions and were simply filtered and washed using ethanol upon cooling to room temperature.

Eventually, both ligands were utilized for the synthesis of the respective heteroleptic complexes  $[\text{Ru}(\text{PT})(\text{bpy})_2]_2^+$  and  $[\text{Ru}(\text{NT})(\text{bpy})_2]_2^+$  with cis-bis(2,2-bipyridine)dichlororuthenium(II) hydrate. Accordingly, an equimolar amount of **PT** or **NT** with  $\text{Ru}(\text{bpy})_2(\text{Cl})_2$  was kept at gentle reflux for 24 h in a 1:1 mixture of ethanol and water. After the counter ion exchange with  $[\text{PF}_6]^-$ , the complexes were purified using first a column chromatography and then a gel permeation chromatography to provide  $[\text{Ru}(\text{PT})(\text{bpy})_2]_2^+$  as orange-brown glassy solid in 61% yield and  $[\text{Ru}(\text{NT})(\text{bpy})_2]_2^+$  as dark red glassy solid in 67% yield.

Next, the homoleptic complexes  $[\text{Ru}(\text{PT})_3]_2^+$  and  $[\text{Ru}(\text{NT})_3]_2^+$  were prepared, which are characterized by the presence of three extended phenanthroline-derived ligands surrounding the ruthenium ion. For this purpose,  $\text{Ru}(\text{DMSO})_4\text{Cl}_2$  [137] has been heated at reflux with **PT** or **NT** for 20 h in ethanol. The purification procedure of the crude products is made by a flash column and a gel permeation chromatography.  $[\text{Ru}(\text{PT})_3]_2^+$  has been obtained as an orange-brown glassy solid in 88% yield and  $[\text{Ru}(\text{NT})_3]_2^+$  as a dark red

## 86 Ru(II) complexes with extended phenanthroline-based ligands

glassy solid in 92% yield. Both ligands and their respective heteroleptic and homoleptic Ru(II) complexes were unambiguously characterized by  $^1\text{H}$  and  $^{13}\text{C}$  NMR, MALDI-TOF mass spectrometry, IR, and elemental analysis.

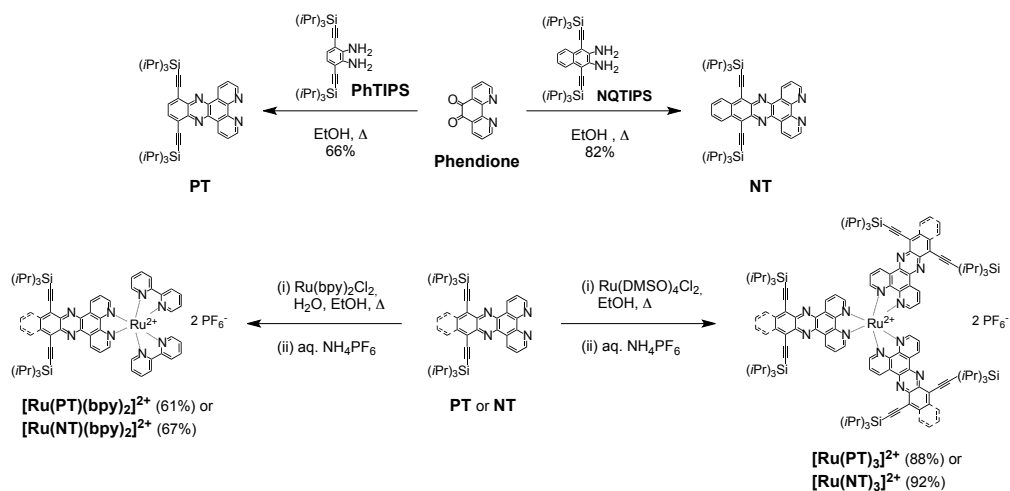


**Figure 5.2:** Synthesis of the Ru(II) and of of the phenanthroline-based ligands.

## 5.2 Electrochemistry

The electrochemical properties of both ligands **PT** and **NT** and the related complexes  $[\text{Ru}(\text{PT})_3]_2^+$ ,  $[\text{Ru}(\text{NT})_3]_2^+$ ,  $[\text{Ru}(\text{PT})(\text{bpy})_2]_2^+$  and  $[\text{Ru}(\text{NT})(\text{bpy})_2]_2^+$  were determined by cyclic voltammetry (CV) and Osteryoung Square Wave Voltammetry (OSWV). The experiments were performed at room temperature using  $\text{CH}_2\text{Cl}_2$  as solvent, tetra-*n*-butylammonium tetrafluoroborate (0.1 M) as supporting electrolyte, a Pt wire as the working electrode and a saturated calomel electrode (SCE) as a reference. Potential data for all of the compounds are collected in Table 5.1, while the more representative experimental curves are depicted in Figure 5.3 and Figure 5.4. The ligands show two successive one-electron reduction processes in the cathodic region, the reduction of **NT** is observed at lower potentials then compared to **PT** due to the extended conjugation of the former, in particular the energy differences are  $\Delta E = 300$  mV for the first reduction process and  $\Delta E = 310$

mV for the second one. A clear oxidation potential is not observed for ligand PT, under the experimental conditions, while NT shows an oxidation process at +1.78 V vs. SCE.

**Table 5.1:** Electrochemical data of samples **PT**, **NT** and their Ru(II) complexes (as hexafluorophosphate salts) [ $8 \cdot 10^{-4}$  M] determined by OSWV on a Pt working electrode in  $\text{CH}_2\text{Cl}_2$  +0.1 M n-Bu<sub>4</sub>NBF<sub>4</sub> at room temperature. Ferrocene is used as internal reference.

Sample	Oxidation		Reduction			
	$E_2$	$E_1$	$E_1$	$E_2$	$E_3$	$E_4$
<b>PT</b>	—	— <sup>a</sup>	-0.98	-1.55	—	—
[Ru(PT) <sub>3</sub> ] <sub>2</sub> <sup>+</sup>	— <sup>b</sup>	+1.64	-0.66	-1.35	—	—
[Ru(PT)(bpy) <sub>2</sub> ] <sub>2</sub> <sup>+</sup>	— <sup>b</sup>	+1.54 <sup>*,c</sup>	-0.67 <sup>*</sup>	-1.24	-1.40	-1.62
<b>NT</b>	—	+1.78 <sup>d</sup>	-0.68 <sup>*</sup>	-1.24	-1.59 <sup>e</sup>	—
[Ru(NT) <sub>3</sub> ] <sub>2</sub> <sup>+</sup>	—	+1.72	-0.45	-1.06	-1.60	—
[Ru(NT)(bpy) <sub>2</sub> ] <sub>2</sub> <sup>+</sup>	+1.73	+1.54	-0.45 <sup>*</sup>	-1.02 <sup>f</sup>	-1.30 <sup>f</sup>	-1.60

<sup>\*</sup>quasi-reversible process (VC experiments).

<sup>a</sup>Oxidation process > 1.7 V increases gradually.

<sup>b</sup>No oxidation process clearly detectable.

<sup>c</sup>Additional oxidation process at 0.82 V with very weak intensity.

<sup>d</sup>An additional oxidation process at 1.62V with weaker intensity is observed.

<sup>e</sup>Very weak intensity.

<sup>f</sup>Appears as quasi-reversible at 200 mVs<sup>-1</sup>.

While for the Ru(II) complexes, the first oxidation process is normally centered onto the metal [138], in the present case the oxidation process could involve both the Ru(II) metal center and the phenanthroline ligands. Trough the support of DFT calculations, carried out for all the complexes in their singlet ground state, it is possible to deduce that the HOMO is always localized on the **PT** or **NT** ligands and that oxidation processes can be centered on them. Spin unrestricted calculations considering the oxidized complexes (*i.e.*, simulated by removing one electron from the molecules) indicate that the spin density distribution is centered on the metal. Moreover, the spin density topology of the oxidized complexes are different then com-

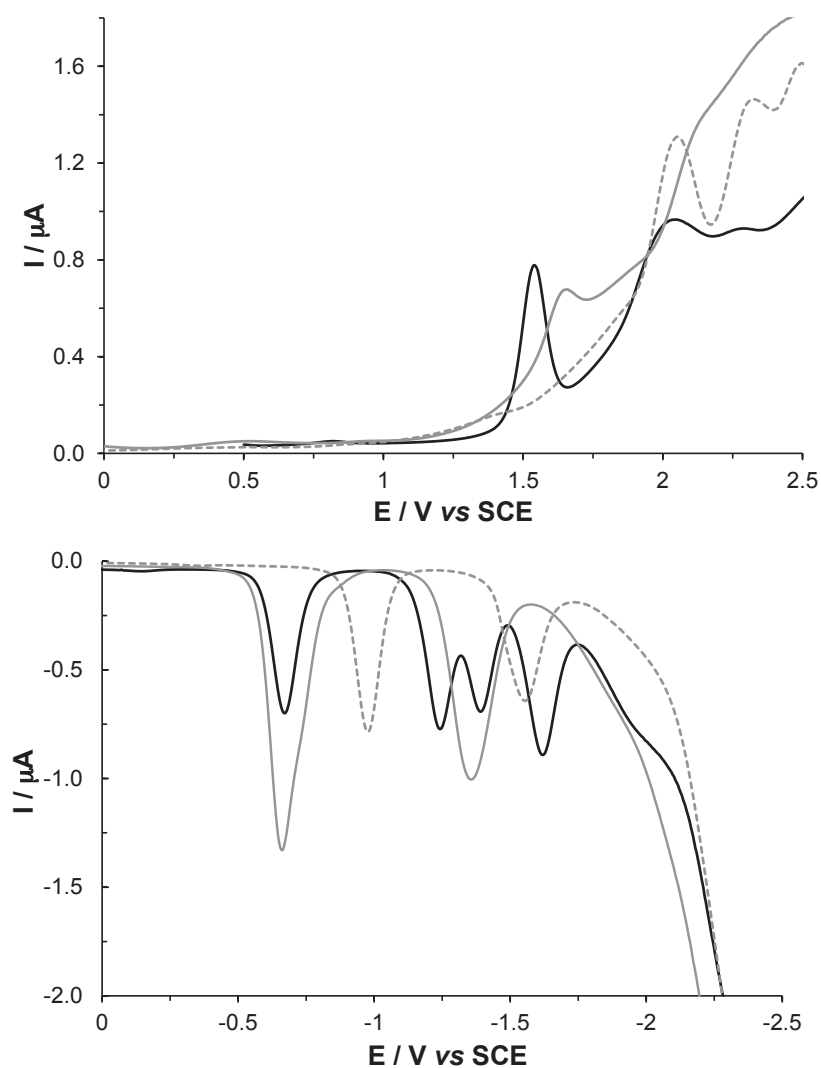


**Figure 5.3:** OSWVs (top: anodic scan; bottom: cathodic scan) of compounds **PT** (dashed grey line),  $[\text{Ru}(\text{PT})_3]_2^+$  (grey line) and  $[\text{Ru}(\text{PT})(\text{bpy})_2]_2^+$  (black line),  $[8 \cdot 10^{-4} \text{ M}]$  on a Pt working electrode in  $\text{CH}_2\text{Cl}_2 + 0.1 \text{ M n-Bu}_4\text{NBF}_4$  at room temperature using a sweep width of 20 mV, a frequency of 10 Hz, and a step potential of 5 mV;  $\text{Fc}/\text{Fc}^+$  is observed at  $+0.55 \pm 0.01 \text{ V}$  under these conditions.

pared to the HOMO of the pristine (see for example  $[\text{Ru}(\text{PT})(\text{bpy})_2]_2^+$  in Figure 5.5). It is evident that the spin density of  $[\text{Ru}(\text{PT})(\text{bpy})_2]_3^+$  in its doublet ground state has a different geometry relative to the HOMO

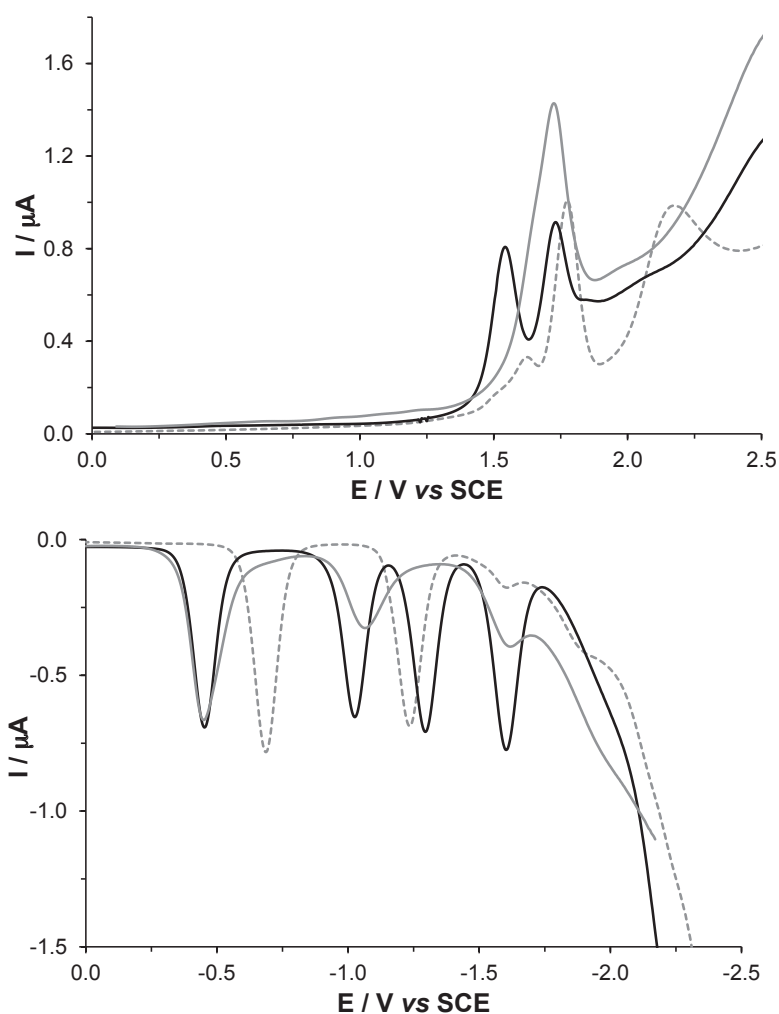


**Figure 5.4:** OSWVs (top: anodic scan; bottom: cathodic scan) of compounds **NT** (dashed grey line),  $[\text{Ru}(\text{NT})_3]_2^+$  (grey line) and  $[\text{Ru}(\text{NT})(\text{bpy})_2]_2^+$  (black line),  $[8 \cdot 10^{-4} \text{ M}]$  on a Pt working electrode in  $\text{CH}_2\text{Cl}_2 + 0.1 \text{ M } n\text{-Bu}_4\text{NBF}_4$  at room temperature using a sweep width of 20 mV, a frequency of 10 Hz, and a step potential of 5 mV; Fc/Fc+ is observed at  $+0.55 \pm 0.01 \text{ V}$  under these conditions.

of pristine  $[\text{Ru}(\text{PT})(\text{bpy})_2]_2^+$ . This observation suggests that the oxidation process cannot be just seen as an electron removal from the HOMO of  $[\text{Ru}(\text{PT})(\text{bpy})_2]_2^+$ .

The enhancement of the oxidation potential when going from

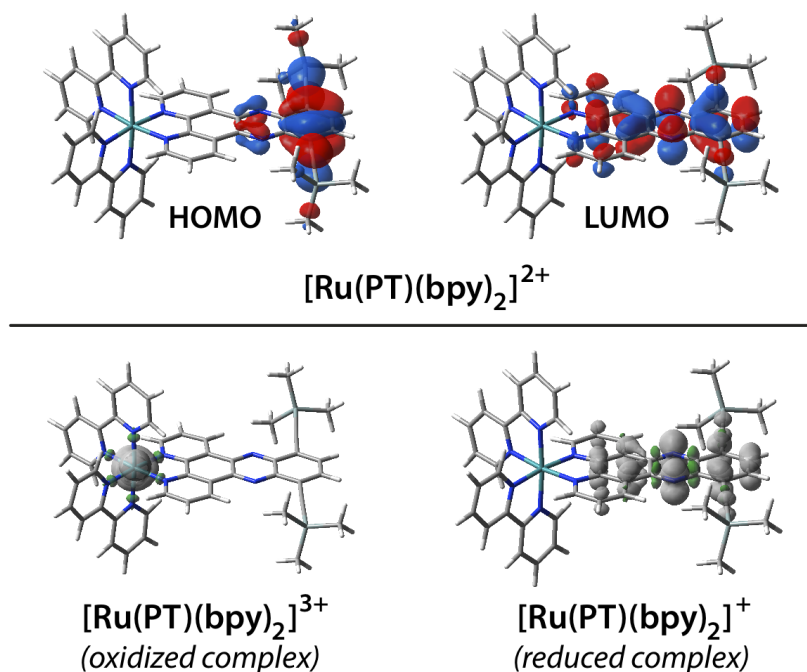


**Figure 5.5:** (Top) Frontier molecular orbitals of  $[\text{Ru}(\text{PT})(\text{bpy})_2]_2^+$  calculated at the PBE0/6-31G(d)&LanL2DZ(Si,Ru) level of theory, using PCM. (Bottom) Spin density distributions for the oxidized and reduced counterparts calculated at the same level of theory (unrestricted calculations with doublet spin multiplicity).

$[\text{Ru}(\text{PT})(\text{bpy})_2]_2^+$  to  $[\text{Ru}(\text{PT})_3]_2^+$ , ( $\Delta E = 100$  mV) is due to the increased electron-deficient character of the **PT** when compared to the **bpy** ligand. A similar but stronger effect is also observed when going from  $[\text{Ru}(\text{NT})(\text{bpy})_2]_2^+$  to  $[\text{Ru}(\text{NT})_3]_2^+$  ( $\Delta E = 180$  mV). This observation is supported by the fact that the first oxidation potential is lower for  $[\text{Ru}(\text{PT})_3]_2^+$  than for  $[\text{Ru}(\text{NT})_3]_2^+$ , as a matter of fact, the more electron-deficient ligand **NT** reduces the electronic density of the molecule and disfavor the oxidation. In the cathodic region, the two first reduction processes of **NT** and **PT** are also observed in  $[\text{Ru}(\text{PT})_3]_2^+$  and  $[\text{Ru}(\text{NT})_3]_2^+$  but these transitions are significantly moved toward anodic potentials due to the coordination to the Ru(II) center. The two characteristic ligand-centered reduction processes of the both extended ligands are also kept in the heteroleptic com-

plexes,  $[\text{Ru}(\text{PT})(\text{bpy})_2]_2^+$  and  $[\text{Ru}(\text{NT})(\text{bpy})_2]_2^+$ . This attribution is validated by DFT calculations carried out on reduced complexes (*i.e.*, simulated by adding one electron to the molecule), as reported in Figure 5.5 for  $[\text{Ru}(\text{PT})(\text{bpy})_2]_2^+$ . Considering the spin density of reduced  $[\text{Ru}(\text{PT})(\text{bpy})_2]_2^+$  in its doublet ground state (Figure 5.5, bottom right) is localized on the extended phenanthroline ligand and it has the same topology of the LUMO orbital of pristine  $[\text{Ru}(\text{PT})(\text{bpy})_2]_2^+$  (Figure 5.5, top). In both the heteroleptic complexes, two other reduction processes localized on the bpy ligands are observed, probably there is also a contribution from NT centered reduction for the last cathodic process at -1.60 V for the latter complex.

## 5.3 Photophysical characterization and theoretical study

In this section the photophysical characterization of all the complexes and the related ligands is described. In particular, in Table 5.2 are collected the absorption data while in Table 5.3 are reported the emission band maxima, luminescence quantum yields and excited lifetimes of the free ligands **PT** and **NT** and of the corresponding homoleptic  $[\text{Ru}(\text{PT})_3]_2^+$ ,  $[\text{Ru}(\text{NT})_3]_2^+$  and heteroleptic  $[\text{Ru}(\text{PT})(\text{bpy})_2]_2^+$ ,  $[\text{Ru}(\text{NT})(\text{bpy})_2]_2^+$  complexes in THF, a solvent that gives excellent solubility for all of the compounds. Therefore, also density functional theory (DFT) [139] and time-dependent DFT (TD-DFT) calculations were made using the polarizable continuum model (PCM), in order to simulate the presence of THF.

### 5.3.1 PT series

The absorption spectrum of the **PT** ligand extends until 450 nm (Figure 5.6); the bands in the low-energy region (*i.e.*, between 350 and 450 nm) result from the lowest three singlet electronic transitions (Figure 5.7 and Figure 5.8 a). As for all the  $n - \pi^*$  transitions, that are formally forbidden by the selection rules, the  $S_0 \rightarrow S_2$  excitation gives a negligible contribution to the experimental absorption spectrum due to its nature (from the lone pairs of the pyrazine moiety to LUMO), in fact, as results from the theoretical calculation, it has a very low oscillator strength ( $f = 0.002$ ). On the other

## 92 Ru(II) complexes with extended phenanthroline-based ligands

**Table 5.2:** Absorption maxima of **PT**,  $[\text{Ru}(\text{PT})_3]_2^+$ ,  $[\text{Ru}(\text{PT})(\text{bpy})_2]_2^+$ , **NT**,  $[\text{Ru}(\text{NT})_3]_2^+$  and  $[\text{Ru}(\text{PT})(\text{bpy})_2]_2^+$ , in THF.

Sample	Absorption maxima $\lambda_{max}$ , nm ( $\epsilon \times 10^4$ , $M^{-1} \text{ cm}^{-1}$ )
<b>PT</b>	247 (5.1), 292 (6.3), 373 (1.5), 392 (2.0)
$[\text{Ru}(\text{PT})_3]_2^+$	265 (15.1), 278 (16.3), 291 (19.0), 321 (15.8), 383 (5.1), 429 (5.4)
$[\text{Ru}(\text{PT})(\text{bpy})_2]_2^+$	247 (6.2), 290 (10.8), 383 (1.7), 437 (2.5)
<b>NT</b>	252 (7.0), 320 (10.7), 334 (12.6), 409 (1.7), 432 (2.6)
$[\text{Ru}(\text{NT})_3]_2^+$	265 (16.7), 345 (22.8), 404 (4.6), 429 (5.2)
$[\text{Ru}(\text{NT})(\text{bpy})_2]_2^+$	286 (10.0), 342 (9.6), 429 (2.8)

hand, both  $S_0 \rightarrow S_1$  and  $S_0 \rightarrow S_3$  belong to  $\pi - \pi^*$  transitions and are quite intense ( $f \sim 0.25$ ).  $S_0 \rightarrow S_1$  can be considered as a simple HOMO $\rightarrow$ LUMO monoexcitation (contribution  $> 98\%$ ), while  $S_0 \rightarrow S_3$  as a HOMO-1 $\rightarrow$ LUMO transition, as depicted in Figure 5.7. The spectral region above 325 nm shows quite intense absorption bands ( $\epsilon_{max} = 63,000 \text{ M}^{-1}\text{cm}^{-1}$  at 292 nm) and is characterized by highly structured profile (Figure 5.6). The electronic transitions that originate the intense absorptions at about 300 nm are  $S_0 \rightarrow S_8$  and  $S_0 \rightarrow S_{12}$ , which involve the displacement of one electron from the HOMO to the LUMO+1 and to the LUMO+3, respectively (Figure 5.8 a). Both transitions have  $\pi - \pi^*$  nature but, the latter is principally centered on the alkynyl moieties, while the former has a stronger CT character, involving also the  $\pi^*$  orbitals of the phenanthroline-type moiety.

The absorption spectrum of **PT** can be associated to the UV portion of the spectrum of  $[\text{Ru}(\text{PT})_3]_2^+$ , which is related to ligand-centered transitions [140] even if the spectrum of the complex is slightly more structured. Moreover, the presence of the peaks at 291 and 393 nm, that are exactly three times higher than that of the corresponding features of **PT**, demonstrate a perfect spectral additivity of the three ligands within the complex (Table 5.2). On the other hand, the spectrum of  $[\text{Ru}(\text{PT})_3]_2^+$  results more extended to higher wavelengths, underpinning the presence of the typical spin permitted singlet metal-to-ligand charge transfer absorption bands ( $^1\text{MLCT}$ )

**Table 5.3:** Emission maxima, quantum yield and excited state lifetime at 298 K and 77 K, in THF.

Sample	298 K Emission <sup>a</sup>			77 K Emission <sup>b</sup>	
	$\lambda^c$ nm	$\tau^{d,f}$ (ns)	$\Phi^{e,f}$ (%)	$\lambda^b$ nm	$\tau^e$ (ns)
<b>PT</b>	480	0.7 (0.8)	3.4 (3.4)	480	0.7
<b>[Ru(PT)<sub>3</sub>]<sub>2</sub><sup>+</sup></b>	700	-	-	(658, 725) <sup>g</sup>	29 ms <sup>g</sup>
<b>[Ru(PT)(bpy)<sub>2</sub>]<sub>2</sub><sup>+</sup></b>	730	-	-	685,750	767
<b>NT</b>	570,610	26.5 (17.9)	62.1 (47.3)	570	19.6
<b>[Ru(NT)<sub>3</sub>]<sub>2</sub><sup>+</sup></b>	570, 610	26.5 (19.1)	0.4 (0.3)	580	21.3
<b>[Ru(NT)(bpy)<sub>2</sub>]<sub>2</sub><sup>+</sup></b>	570, 610	26.3 (18.2)	0.2 (0.1)	590	20.8

<sup>a</sup>Tetrahydrofuran solution.<sup>b</sup>Butyronitrile glass.<sup>c</sup>Highest energy feature of the luminescence bands.<sup>d</sup>Excited state lifetime values, estimated error  $\pm 8\%$ .<sup>e</sup>Luminescence quantum yield, estimated error  $\pm 20\%$ .<sup>f</sup>Oxygen free solution, air equilibrated data in bracket.<sup>g</sup>Phosphorescence emission.

of Ru(II) complexes. Then, comparing the absorption spectrum of the free ligand **PT** to the wide absorption band at 429 nm of **[Ru(PT)<sub>3</sub>]<sub>2</sub><sup>+</sup>** it is possible to deduce that the latter entails the contribution of both ligand-centered (LC) and MLCT transitions. TD-DFT calculations analyze the nature of the electronic transitions which provide this broad absorption band. Since **[Ru(PT)<sub>3</sub>]<sub>2</sub><sup>+</sup>** has a pseudo D<sub>3</sub> symmetry, the theoretical vertical excitations looks in triplets of quasi-degenerate electronic transitions. Therefore, the lowest energy singlet vertical excitation is actually a cluster of three pseudo-degenerate transitions located at 477 nm ( $S_{1,2,3}$   $f \sim 0.16$ , Figure 5.8 b), each of which is centered on an individual **PT** moiety and have essentially the same nature. In particular, this cluster of pseudo-degenerate transitions is

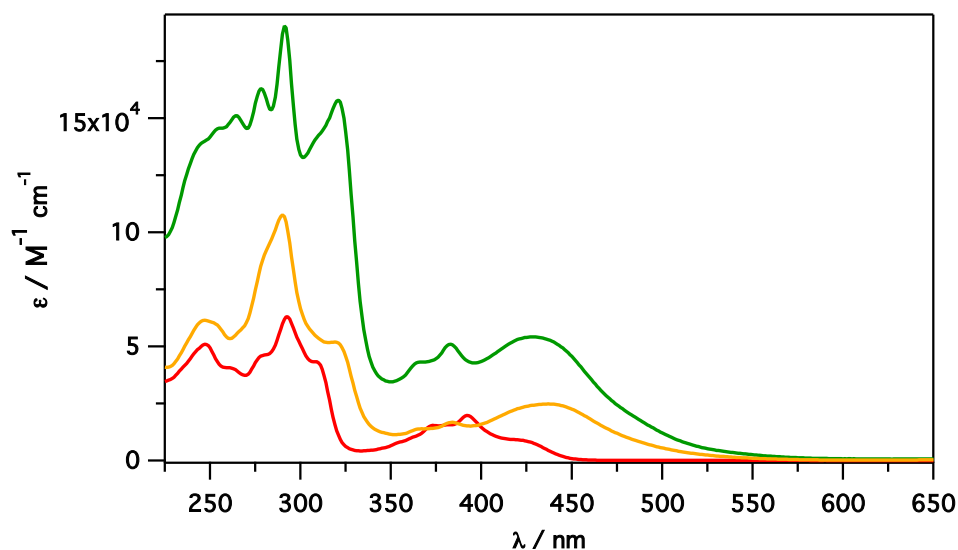


**Figure 5.6:** Absorption spectra of **PT** (red),  $[\text{Ru}(\text{PT})_3]_2^+$  (green) and  $[\text{Ru}(\text{PT})(\text{bpy})_2]_2^+$  (orange) in THF.

similar to the lowest vertical excitation of the **PT** ligand with an only difference being the associated excitation energy that, in the case of the complex, is 0.28 eV lower than the free ligand, in line with experimental results. Other ligand centered transitions are also observed at about 430 nm, but in this case with a lower oscillator strengths ( $S_{7,8,9} f \sim 0.005$ , Figure 5.8 b) leading an irrelevant contribution in the absorption spectrum of the homoleptic complex. However, also two different sets of metal-to-ligand charge transfer transitions are expected in the same spectral region (at 430 nm for  $S_{4,5,6} f \sim 0.0005$  and around 415 nm for  $S_{10,11} f \sim 0.16$ , respectively, Figure 5.8 b); these excitations entail the promotion of an electron from one of the three pseudo  $t_{2g}$  orbital of the metal to a  $\pi^*$  orbital situated on one of the three ligand units.

The heteroleptic complex, named  $[\text{Ru}(\text{PT})(\text{bpy})_2]_2^+$ , shows features that are characteristic of both ligands. In particular, the band at 290 nm is easily ascribable to the two bpy ligands and the bands in the range 360-390 nm indicate the presence of the **PT** unit. The features in the visible portion of the spectrum are quite similar to those of  $[\text{Ru}(\text{PT})_3]_2^+$ , but in this case, the **PT**-centered transitions are mixed with two different kinds of MLCT

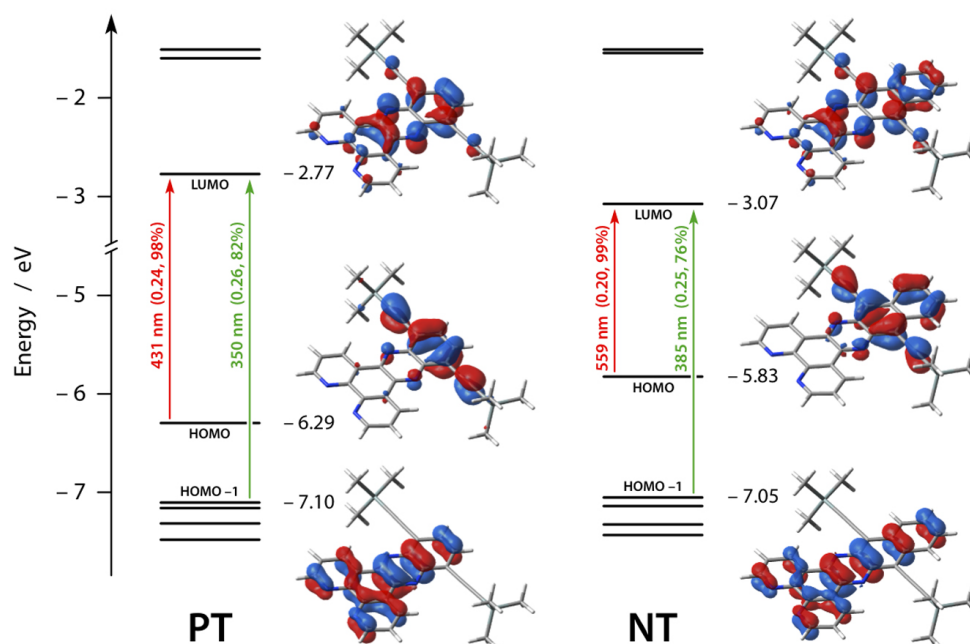


**Figure 5.7:** Energy diagram of frontier molecular orbitals of **PT** and **NT** ligands (in eV) obtained at the PCM-PBE0/6-31G(d) level of theory. The Kohn-Sham molecular orbitals involved in the  $S_0$  to  $S_1$  (red) and  $S_0$  to  $S_3$  transitions (green) are also reported for clarity (isovalue:  $0.03 e^{1/2} bohr^{-3/2}$ ).

transitions (*i.e.*, to the **PT** and **bpy** ligands). Due to the lower symmetry of this complex, a pseudo  $C_2$  point group, it is easy to have clear picture of the lowest-energy singlet transitions (Figure 5.8 c) and to represent the lowest-energy triplet excitations, which are partially allowed due to the high spin-orbit coupling with the Ru(II) metal center, which play an important role in the deactivation of the excited states. In Figure 5.9, the lowest three triplet vertical excitations of  $[Ru(PT)(bpy)_2]_2^+$  are represented in terms of couples of natural transition orbitals (NTO). In particular, the lowest triplet vertical excitation leads to a ligand-centered state ( $T_1$ ) that is placed 1.64 eV above the ground-state minimum. Several MLCT transitions can be found at higher energy, the lowest charge-transfer transition formally involves the promotion of one electron from the Ru(II) metal center to **PT** ( $S_0 \rightarrow T_2$ , 2.60 eV), while the third excitations ( $T_3$ ) is attributed to Ru  $\rightarrow$  **bpy** transition.

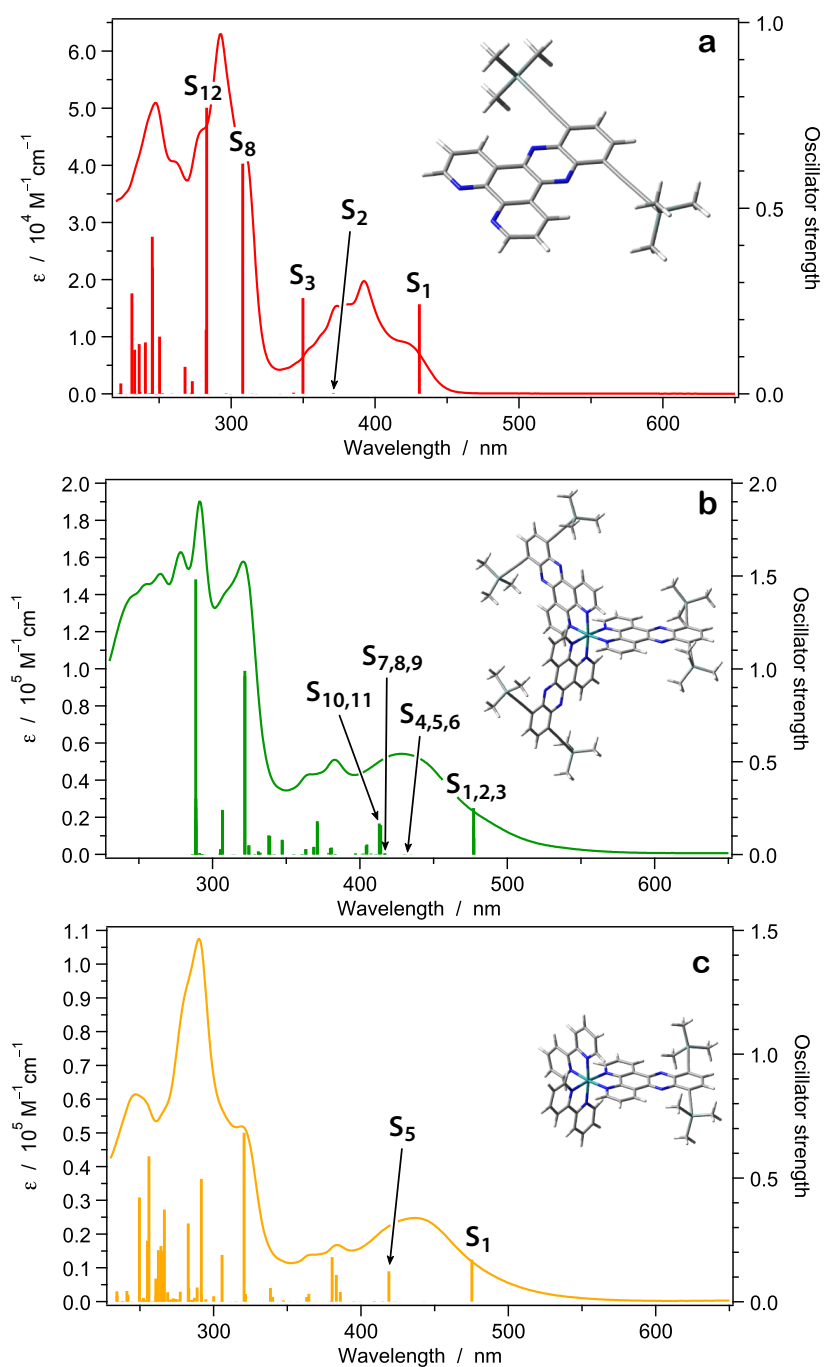


**Figure 5.8:** Singlet vertical excitations (bars) computed at the TD-PBE0/6-31G(d)&LanL2DZ(Si) or (Si,Ru) level of theory (using PCM) compared with the room-temperature experimental absorption spectrum of (a) **PT** (red line), (b)  $[\text{Ru}(\text{PT})_3]_2^+$  (green line) and (c)  $[\text{Ru}(\text{PT})(\text{bpy})_2]_2^+$  (orange line) in THF.

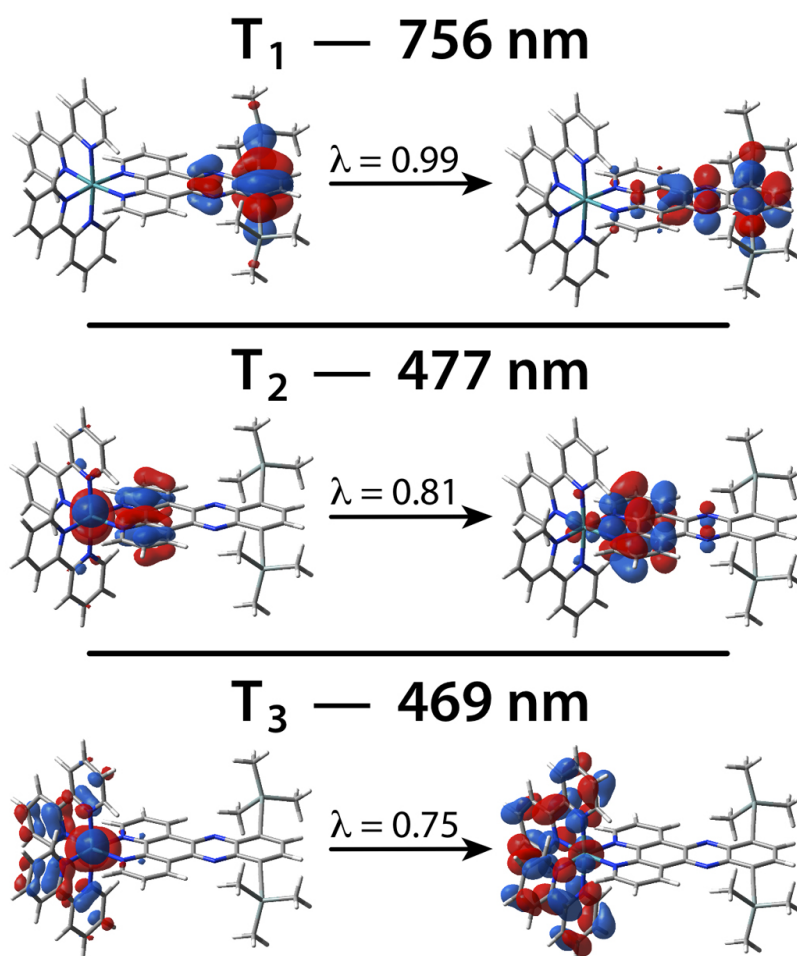


**Figure 5.9:** Calculated NTOs couples describing the three lowest singlet vertical excitations for complex  $[\text{Ru}(\text{PT})(\text{bpy})_2]_2^+$  in THF using PCM-PBE0/6-31G(d)&LANL2DZ(Ru,Si) level of theory. The  $\lambda$  value is the natural transition orbital eigenvalue associated with that NTOs couple.

Differently from similar molecule such as dppz (dipyrido[3,2-a:2',3'-c]phenazine), which is non fluorescent, the **PT** shows a relatively strong fluorescence band at  $\lambda_{max} = 480$  nm (Figure 5.10 a) with an emission quantum yield ( $\Phi$ ) of 3.4% and excited state lifetime ( $\tau$ ) of 0.8 ns. The data collected for **PT** at 77 K, exhibit both fluorescence ( $\lambda_{max} = 480$  nm) and a strongly red-shifted, highly structured and long-lived phosphorescence ( $\tau = 29$  ms) with the highest energy spectral feature placed at 658 nm (Figure 5.10 b).

The homoleptic and heteroleptic **PT**-based complexes do not show any luminescence in the VIS and NIR region in air equilibrated THF solution, while a clear luminescence band detected at 1270 nm (Figure 5.10 a). This latter is indicative of molecular singlet oxygen sensitization ( $^1O_2^*$ ) by a triplet excited state [119]. In oxygen free THF solution at 298 K, both  $[\text{Ru}(\text{PT})_3]_2^+$  and  $[\text{Ru}(\text{PT})(\text{bpy})_2]_2^+$  exhibit very similar emission bands at  $\lambda_{max} = 695$  nm, that are virtually superimposable to the phosphorescence band of **PT** at 77 K (Figure 5.10). Both complexes have poor emission quantum yields of 0.20% and 0.42% for  $[\text{Ru}(\text{PT})_3]_2^+$  and  $[\text{Ru}(\text{PT})(\text{bpy})_2]_2^+$ , respectively, while the excited state lifetime could not be measured due to weak signal. In butyronitrile rigid glass at 77 K, the emission bands of both complexes are again virtually identical to those recorded at room temperature, but more vibrationally resolved. The lifetimes are over 700 ns, suggesting a triplet nature of the transitions (Table 5.3). The lack of rigidochromic shift suggests that the emitting triplet states of both complexes are centered on the **PT** ligand and do not have an MLCT character, as corroborated by the excellent spectral matching (Figure 5.10). Thanks to the heavy atom effect of the Ru(II), which enables remarkably quicker spin forbidden triplet-singlet deactivations, the lifetime of the **PT** triplet in the complexes results greatly reduced [141]. The excitation spectra recorded at 695 nm perfectly match the absorption profiles of the complexes, corroborating the reliability of the emission signals, despite weakness (Figure 5.11).

In order to verify the experimental results of triplet-ligand centered emission the out spin-unrestricted U-DFT calculations on the lowest triplet state of both free ligand and its related Ru(II) complexes have been carried out. In Figure 5.12 are shown the spin density distribution calculated for the lowest-energy triplet state of **PT**,  $[\text{Ru}(\text{PT})_3]_2^+$  and  $[\text{Ru}(\text{PT})(\text{bpy})_2]_2^+$ . All the triplets exhibit the same behavior, suggesting that the lowest triplet state is always centered on the **PT** ligand, definitely validating the hypothesis of a  $^3\text{LC}$  emission centered on the extended ligand also in both complexes, as previously seen on similar systems [142]. The lowest triplet state is predicted at 1.73 eV (715 nm) above the ground state (adiabatic energy difference) for **PT**, a value in agreement with the experimental phosphorescence maximum at 77 K (1.88 eV, Table 5.3). In the case of  $[\text{Ru}(\text{PT})_3]_2^+$  and  $[\text{Ru}(\text{PT})(\text{bpy})_2]_2^+$ , the lowest triplet state is found at 1.60 eV and 1.61

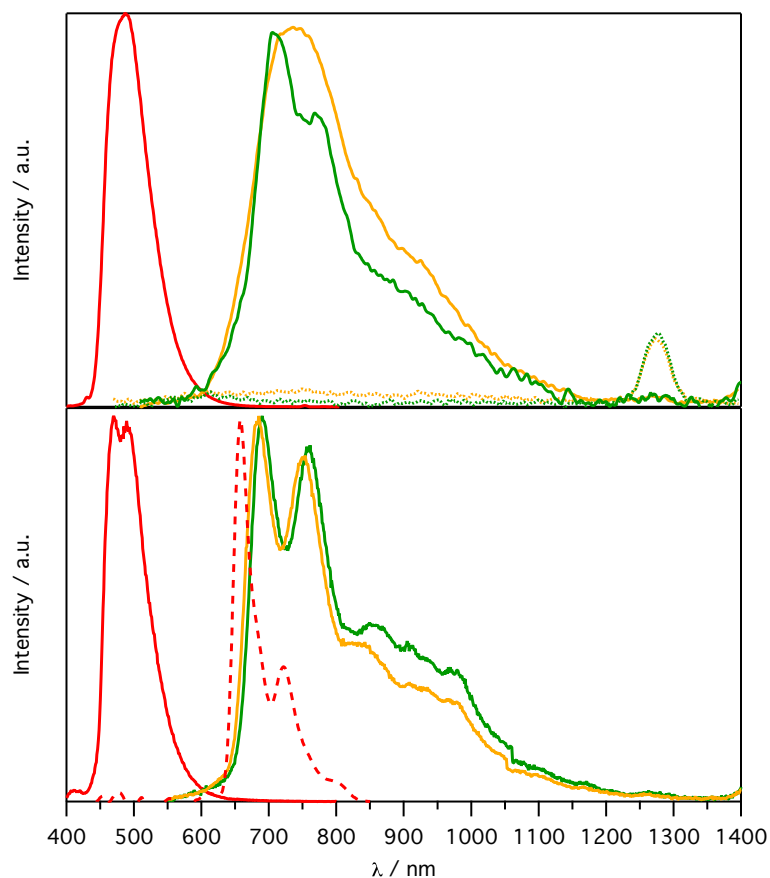


**Figure 5.10:** Emission spectra of **PT** (red, UV-Vis detector),  $[\text{Ru}(\text{PT})_3]_2^+$  (green, NIR detector) and  $[\text{Ru}(\text{PT})(\text{bpy})_2]_2^+$  (orange, NIR detector) in THF: (a) at 298 K (the dotted lines correspond to the air equilibrated solutions; (b) at 77 K (the dashed line corresponds to **PT** phosphorescence).

eV above the singlet ground state (adiabatic energy difference), respectively. These estimations are in good agreement with the experimental data since the same red shift ( $\sim 0.10$  eV) is also observed comparing **PT** phosphorescence (658 nm, 1.88 eV) with the emissions from both Ru(II) complexes at 77 K (1.80 eV, Table 5.3).

## 100 Ru(II) complexes with extended phenanthroline-based ligands

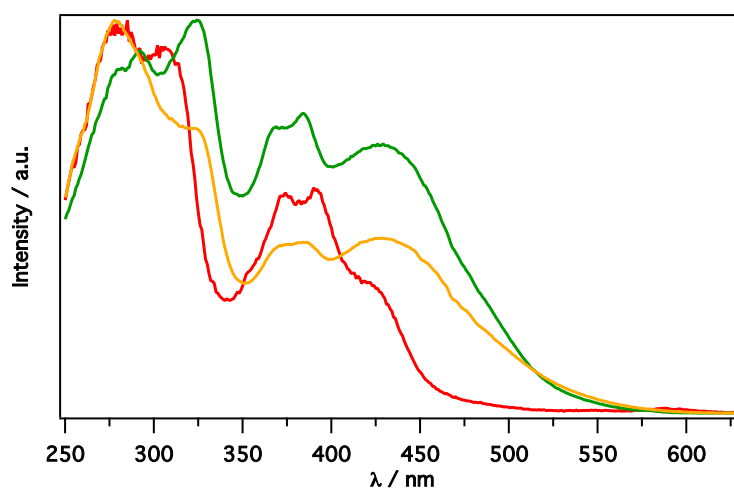


**Figure 5.11:** Excitation spectra recorded at  $\lambda_{em}$  695 nm of **PT** (red),  $[\text{Ru}(\text{PT})_3]_2^+$  (green) and  $[\text{Ru}(\text{PT})(\text{bpy})_2]_2^+$  (orange) in THF.

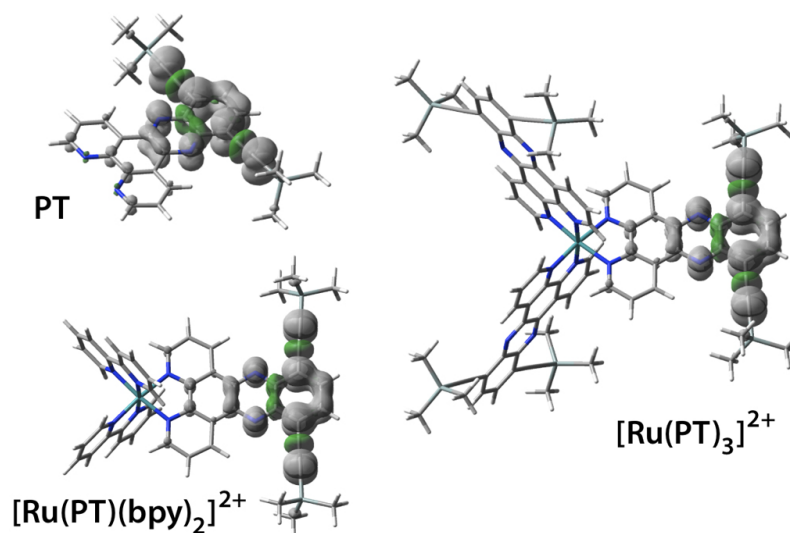


**Figure 5.12:** Spin density distribution (isovalue:  $0.002 e \text{ bohr}^{-3}$ ) of the lowest triplet state of **PT** (top, left),  $[\text{Ru}(\text{PT})_3]_2^+$  (middle, right) and  $[\text{Ru}(\text{PT})(\text{bpy})_2]_2^+$  (bottom, left).

### 5.3.2 NT series

The extension of  $\pi$ -delocalization (*i.e.*, the addition of a benzene unit to **PT**) entails the elongation of the absorption spectrum of **NT** by about 100

nm towards the red spectral region (Figure 5.13).

Therefore, the  $S_0 \rightarrow S_1$  vertical excitation that involves the lowest-energy absorption of the **NT** ligand is red shifted by about 128 nm compared to **PT** and is calculated at 559 nm. As shown in Figure 5.7, the topology of the frontier molecular orbitals of **NT** is not strongly altered by the extension of the  $\pi$ -delocalization and the main difference compared to **PT** concerns the energy. It is important to emphasize that, while the first transition is computed to have a remarkable red shift on passing from **PT** to **NT**, the  $S_0 \rightarrow S_3$  vertical excitation of **NT** is calculated to be shifted by only 31 nm toward the longer wavelength compared to **PT**. Therefore, the main difference of the absorption spectra of **PT** and **NT** in the region from 330 to 600 nm can be seen as a different superimposition of the vibronic progressions that result from the intense  $S_0 \rightarrow S_1$  and  $S_0 \rightarrow S_3$  transitions in both ligands (Figure 5.8 a and Figure 5.14). Moreover, the absorbance in the UV region of **NT** is twice as much compared to **PT** ( $\epsilon_{max} = 126,000 M^{-1}cm^{-1}$  at 334 nm).

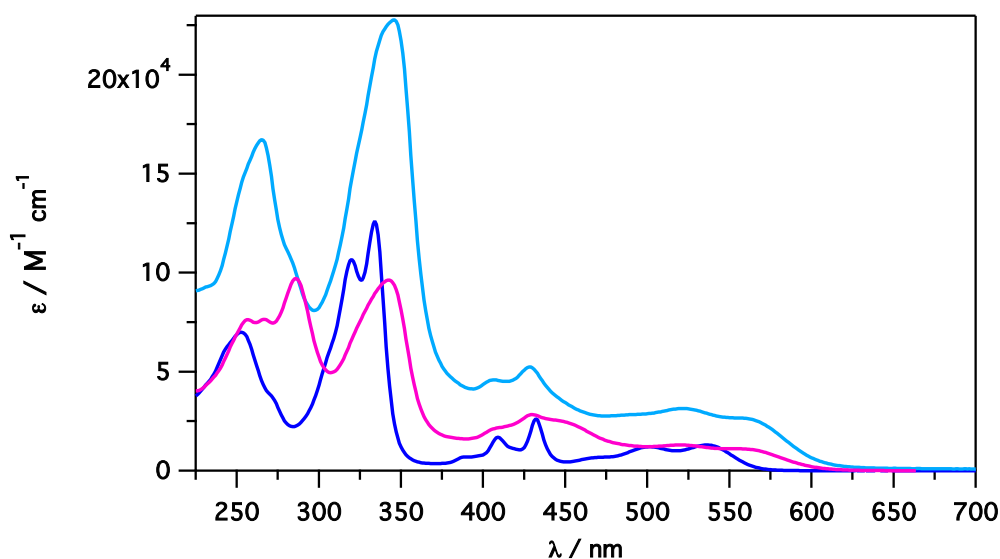


**Figure 5.13:** Absorption spectra of **NT** (blue),  $[\text{Ru}(\text{NT})_3]_2^+$  (light blue) and  $[\text{Ru}(\text{NT})(\text{bpy})_2]_2^+$  (magenta) in THF.

The absorption spectrum of  $[\text{Ru}(\text{NT})_3]_2^+$  is similar in shape to that of **NT**, but spectral features are less resolved due to the presence of both

## 102 Ru(II) complexes with extended phenanthroline-based ligands

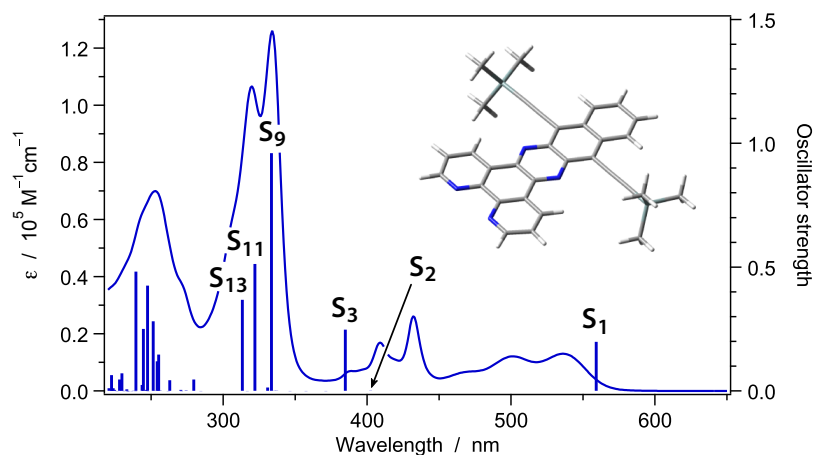


**Figure 5.14:** First 60 singlet vertical excitations (blue bars) computed at the TD-PBE0/6-31G(d) & LanL2DZ(Si) level of theory (using PCM) compared with the room-temperature experimental absorption spectrum of **NT** (blue line) in THF.

$^1$ MLCT and LC transitions, which are also responsible for the elongation of the spectrum above 570 nm. The heteroleptic complex  $[\text{Ru}(\text{NT})(\text{bpy})_2]_2^+$  shows a highly structured absorption spectrum from which it is possible to identify peculiar features related to the presence of bpy unit (*i.e.*, the peak at about 290 nm, showing  $^1$ LC character) and the shoulder at around 450 nm ascribable to  $^1$ MLCT from Ru(II) to bpy transitions. The first eight singlet vertical excitations calculated for  $[\text{Ru}(\text{NT})(\text{bpy})_2]_2^+$  display that the first one is completely centered on **NT** and is a pure HOMO  $\rightarrow$  LUMO transition centered at 623 nm (with an elevated oscillator strength  $f = 0.14$ ). Besides, the  $S_0 \rightarrow S_2$  and  $S_0 \rightarrow S_3$  transitions display  $^1$ MLCT character (Ru(II)  $\rightarrow$  NT). The first singlet excitation involving Ru(II)  $\rightarrow$  bpy  $^1$ MLCT transition is  $S_0 \rightarrow S_6$  and is calculated at 426 nm. Differently from  $[\text{Ru}(\text{PT})(\text{bpy})_2]_2^+$ , the first three triplet vertical excitations of  $[\text{Ru}(\text{NT})(\text{bpy})_2]_2^+$  always involve the **NT** ligand and are reported in Figure 5.15 in terms of natural transition orbitals (NTO) couples. The first transition has  $^3$ LC character, while both  $S_0 \rightarrow T_2$  and  $S_0 \rightarrow T_3$  are two different Ru(II)  $\rightarrow$  NT  $^3$ MLCT transitions which entail different  $\pi^*$  orbitals. While only at higher energy (at about 470 nm), Ru(II)  $\rightarrow$  bpy nature  $^3$ MLCT transitions can be found (Figure 5.16).

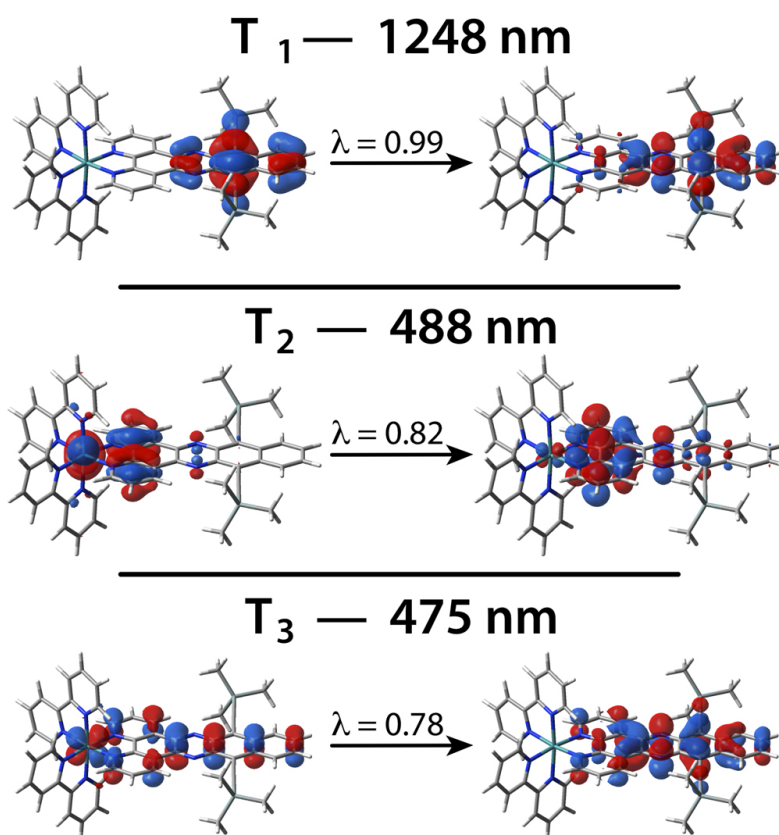


**Figure 5.15:** Calculated NTOs couples describing the three lowest triplet vertical excitations for  $[\text{Ru}(\text{NT})(\text{bpy})_2]_2^+$  in THF using the PCM-PBE0/6-31G(d)&LANL2DZ(Ru,Si) level of theory. The  $\lambda$  value is the natural transition orbital eigenvalue associated with that NTOs couple. Higher-energy transitions (up to  $S_0$  to  $T_6$ ) are reported, using the same NTO formalism, in Figure 5.16

When compared to the parent compound **dnp** (4,5,9,16-tetraazadibenzo[a,c]naphthacene) that is highly luminescent ( $\lambda_{max} = 570$  nm,  $\Phi = 33\%$  and  $\tau = 44$  ns in oxygen free  $\text{CH}_3\text{CN}$ ) [143], **NT** is an even stronger emitter, with  $\lambda_{max} = 570$  nm,  $\Phi = 62\%$  and  $\tau = 26.5$  ns in oxygen free THF (Figure 5.17).

The luminescence spectra recorded at 77K, both in the Vis and NIR spectral region, with steady state-state as well as time-resolved techniques does not exhibit any long-lived triplet emission; therefore, **NT** does not show

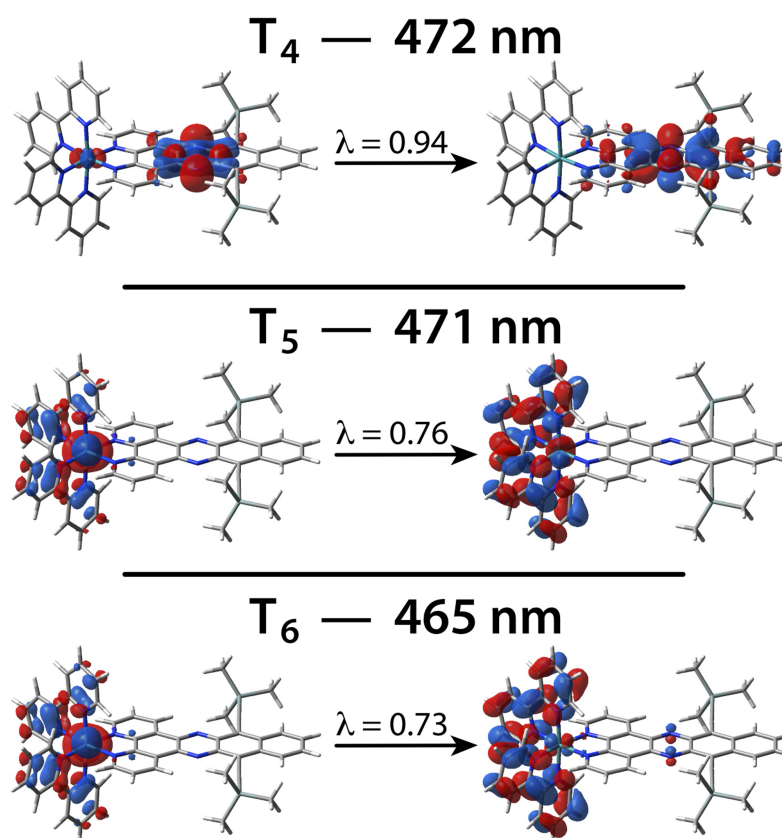


**Figure 5.16:** Calculated NTOs couples describing the triplet vertical excitations  $S_0 \rightarrow T_4$ ,  $S_0 \rightarrow T_5$  and  $S_0 \rightarrow T_6$  for  $[\text{Ru}(\text{NT})(\text{bpy})_2]_2^+$  in THF using the PCM-PBE0/6-31G(d)&LANL2DZ(Ru,Si) level of theory. The  $\lambda$  value is the natural transition orbital eigenvalue associated with that NTOs couple. Lowest-energy transitions are reported, using the same NTO formalism, in Figure 5.15.

phosphorescence. This photophysical behavior is rationalized with the aid of DFT methods. U-DFT calculations carried out on **NT** anticipate that the lowest triplet state is placed 1.08 eV above the singlet ground state (i.e.,  $\lambda$  1150 nm). Taking into account the energy gap law, such a small energy-gap between the lowest triplet state and the singlet ground state explains very fast non-radiative relaxation processes and the absence of phosphorescence.

From the literature,  $[\text{Ru}(\text{bpy})_2(\text{dppn})]_2^+$  has been found to be weakly

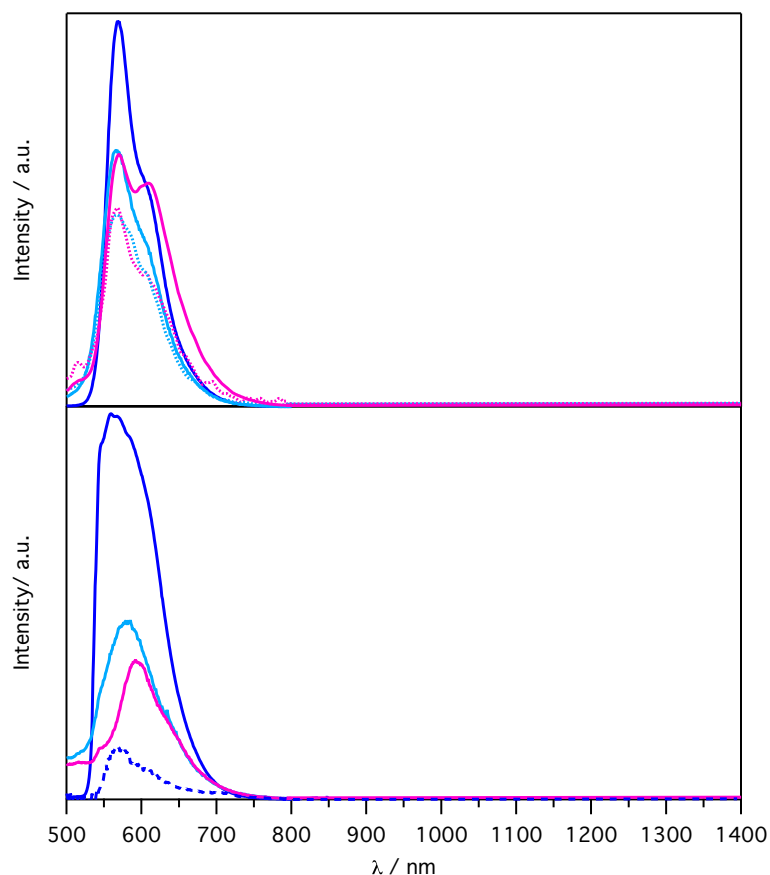


**Figure 5.17:** Emission spectra of **NT** (blue),  $[\text{Ru}(\text{NT})_3]_2^+$  (light blue) and  $[\text{Ru}(\text{NT})(\text{bpy})_2]_2^+$  (magenta) in THF: (a) at 298 K (dotted line correspond to the spectra of the air equilibrated solution; (b) and 77 K, where the dashed line corresponds to **NT** residual fluorescence after a delay of 20  $\mu\text{s}$  and shows the absence of any phosphorescence signal in the NIR spectral region.

luminescent in  $\text{CH}_3\text{CN}$  at room temperature with  $\lambda_{\text{max}} = 570$  nm and  $\Phi = 0.1\%$  [129, 143]. While at 77 K,  $[\text{Ru}(\text{bpy})_2(\text{dppn})]_2^+$  shows two emission band, one at  $\lambda_{\text{max}} = 580$  nm ascribable to a  $^3\text{MLCT}$  transition [129, 143] and another one at about 820 nm, attributed to the triplet of the **dppn** ligand [143]. Moving from **dppn** to **NT** a complete disappearance of triplet emission is found in both  $[\text{Ru}(\text{NT})(\text{bpy})_2]_2^+$  as well as in  $[\text{Ru}(\text{NT})_3]_2^+$ . However, a weak luminescence band is always detected both at 298 and 77 K; this band

## 106 Ru(II) complexes with extended phenanthroline-based ligands

has spectral position and associated lifetime (26 ns in oxygen free THF) that allows unambiguous assignment to residual **NT** fluorescence (Figure 5.17). The estimated fluorescence quantum yield is about 0.3%, suggesting that the concentration of free **NT** in both complexes is less than 0.5%.

UDFT theoretical methods predict that, as in the case of **PT**-based complexes, also the **NT**-based serie has a  $^3\text{LC}$  triplet state, centered on the  $\pi$ -region of the ligand, positioned at about 0.97 eV over the ground state for both complexes (adiabatic energy difference). Figure 5.18 shows the spin density distribution for the lowest-energy triplet state of ligand **NT** and of complexes  $[\text{Ru}(\text{NT})_3]_2^+$  and  $[\text{Ru}(\text{NT})(\text{bpy})_2]_2^+$ . All the triplets have basically the same spin density distribution, which is also not far from the topology already seen for the **PT**-based samples. The main difference compared to the previous series is that the triplet state of **NT** ligand is not emissive and, therefore, also the  $[\text{Ru}(\text{NT})_3]_2^+$  and  $[\text{Ru}(\text{NT})(\text{bpy})_2]_2^+$  complexes do not show any phosphorescence.

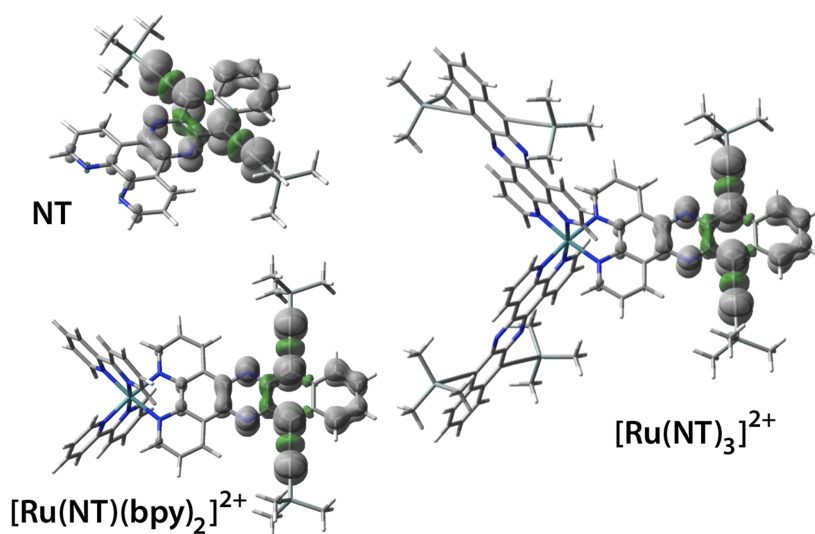


**Figure 5.18:** Spin density distribution for the lowest-energy triplet state of **NT**,  $[\text{Ru}(\text{NT})_3]_2^+$  and  $[\text{Ru}(\text{NT})(\text{bpy})_2]_2^+$  computed in THF using the PCM-PBE0/6-31G(d)&LANL2DZ(Ru,Si) level of theory.

## 5.4 Conclusion

The literature on Ru(II) complexes with extended phenanthroline ligands presents a large number of papers in which the photophysical behavior is strongly dependent on the chemical environment [126]. In this chapter, two extended phenanthroline-based ligands **PT** and **NT** have been presented, along with the related homoleptic and heteroleptic Ru(II) complexes. A complete characterization of all the compounds has been obtained comparing experimental data with DFT calculations. The theoretical study shows that the lowest electronic transitions of the homoleptic and heteroleptic complexes  $[\text{Ru}(\text{PT})_3]_2^+$ ,  $[\text{Ru}(\text{NT})_3]_2^+$  and  $[\text{Ru}(\text{PT})(\text{bpy})_2]_2^+$ ,  $[\text{Ru}(\text{NT})(\text{bpy})_2]_2^+$  are centered on **PT** and **NT**. This assignment is unambiguously confirmed by experimental evidences on the **PT**-based complexes at 77 K, which show an emission band that is virtually superimposable to the phosphorescence of the free ligand.  $[\text{Ru}(\text{PT})_3]_2^+$  and  $[\text{Ru}(\text{PT})(\text{bpy})_2]_2^+$  also exhibit weak luminescence at room temperature, also assigned to  $^3\text{LC}$  states. On the other hand, both complexes of the more extended ligand,  $[\text{Ru}(\text{NT})_3]_2^+$  and  $[\text{Ru}(\text{NT})(\text{bpy})_2]_2^+$ , do not emit under any conditions due to the location of the triplet level that is placed below 1 eV, where only non radiative processes occur for the energy gap law.

The results presented in this work confirm that Ru(II) complexes with extended phenanthroline ligands can be used to obtain long wavelength absorption materials, which are potentially interesting for the harvesting of solar energy [6]. Moreover, these complexes may exhibit long-lived excited states but, due to ligand centered origin and to the extension of the ligands beyond a certain limit, non-emissive and short-lived excited states are populated, strongly limiting the possibility to use them as photosensitizers for solar energy conversion systems. Further ligand modification are now pursued, in order to investigate the potential of these complexes as photosensitizers, while subsequent improvements of the ligands can be envisaged to obtain new luminescent sensors.



# Chapter 6

## Instrumentation

### 6.1 Steady state absorption and luminescence measurements

Absorption spectra were recorded with a Perkin-Elmer  $\lambda$ 950 UV/Vis/NIR spectrophotometer. Molar absorption values ( $\epsilon$ ) were calculated by applying the Lambert-Beer law to the absorbance spectra ( $A_{max} < 0.7$ ) of the compounds. For steady-state photoluminescence measurements, the samples were placed in a fluorimetric 1-cm path cuvettes and, when necessary, purged from oxygen by bubbling with argon. Uncorrected emission spectra were obtained with an Edinburgh FLS920 spectrometer (continuous 450 W Xe lamp) equipped with Hamamatsu R928 photomultiplier tube (185-850 nm). Steady-state NIR luminescence spectra were obtained with the same spectrophotometer fitted with Hamamatsu R5509-72 supercooled photomultiplier tube (400-1700 nm) at 193 K and a TM300 emission monochromator with NIR grating blazed at 1000 nm. The photoluminescence mapping were obtain using as excitation a 450 W Xe lamp and as detector a liquid-nitrogen-cooled germanium and preamplifier (Northcoast Scientific Corp. Model EO-817L). A Northcoastmuon filter (Model 829B) was used as an electronic signal filter; the signal was sent to a lock-in amplifier (Standford Research Systems, Inc. Model SR510) to enhance the S-N ratio of the weak NIR emission bands. Corrected spectra were obtained via a calibration curve supplied with the instrument. To record the 77K luminescence spectra, the samples were put in glass tubes (2 mm diameter) and inserted in a cold finger quartz dewar,

filled with liquid nitrogen. Experimental uncertainties are estimated to be  $\pm 2$  nm and  $\pm 5$  nm for absorption and emission peaks respectively. Luminescence quantum yields of emitting solutions were determined from the corrected emission spectra, according to the approach described by Demas and Crosby [144] using either  $[\text{Ru}(\text{bpy})_3\text{Cl}_2]$  ( $\Phi_{em} = 0.028$  in air-equilibrated water solution) as standard. The quantum yield values are indecisive up to  $\pm 20\%$  in solution, due to the experimental uncertainties.

## 6.2 Time resolved emission measurements

Emission lifetimes on the nanosecond time scale were determined with a IBH single photon counting spectrometer equipped with a series of nanoled (IBH) excitation sources ( $\lambda_{ex} = 278, 331, 373, 465$  nm). The detector was a red-sensitive (185-850 nm) Horiba Jobin Yvon (TBX-PS) photomultiplier tube. Analysis of the luminescence decay profiles against time was accomplished with the Decay Analysis Software DAS6 provided by the manufacturer. The luminophores having lifetime in the microsecond-millisecond time scale were measured using a Perkin-Elmer LS50B spectrofluorimeter equipped with a pulsed xenon lamp with variable repetition rate and elaborated with standard software fitting procedures.

## 6.3 Atomic force microscopy measurements

AFM imaging was performed using a Nanoscope Multimode 8 (Bruker, Santa Barbara, USA) equipped with a 15  $\mu\text{m}$  piezoelectric scanner. The AFM was operated in tapping mode and in peak-force tapping mode.

# Bibliography

- (1) N. Armaroli and V. Balzani, *Energy Environ. Sci.*, 2011, **4**, 3193–3222.
- (2) A. C. Dillon, *Chemical Reviews*, 2010, **110**, 6856–6872.
- (3) R. C. Haddon, *Accounts of Chemical Research*, 2002, **35**, 997–997.
- (4) J.-L. Bredas and J. R. Durrant, *Accounts of Chemical Research*, 2009, **42**, 1689–1690.
- (5) A. J. Heeger, *Advanced Materials*, 2014, **26**, 10–28.
- (6) V. Balzani, A. Credi and M. Venturi, *ChemSusChem*, 2008, **1**, 26–58.
- (7) S. Iijima, *Nature*, Nov. 1991, **354**, 56–58.
- (8) K. S. Novoselov, A. K. Geim, S. V. Morozov, D. Jiang, M. I. Katsnelson, I. V. Grigorieva, S. V. Dubonos and A. A. Firsov, *Nature*, Nov. 2005, **438**, 197–200.
- (9) R. Saito, G. Dresselhaus and M. S. Dresselhaus, *Phys. Rev. B*, 2000, **61**, 2981–2990.
- (10) L. J. Carlson and T. D. Krauss, *Accounts of Chemical Research*, 2008, **41**, 235–243.
- (11) J. W. Mintmire and C. T. White, *Phys. Rev. Lett.*, 1998, **81**, 2506–2509.
- (12) H. Kataura, Y. Kumazawa, Y. Maniwa, I. Umezu, S. Suzuki, Y. Ohtsuka and Y. Achiba, *Synthetic Metals*, 1999, **103**, International Conference on Science and Technology of Synthetic Metals, 2555–2558.
- (13) J. Holden, P. Zhou, X.-X. Bi, P. Eklund, S. Bandow, R. Jishi, K. D. Chowdhury, G. Dresselhaus and M. Dresselhaus, *Chemical Physics Letters*, 1994, **220**, 186–191.

- (14) S. M. Bachilo, M. S. Strano, C. Kittrell, R. H. Hauge, R. E. Smalley and R. B. Weisman, *Science*, 2002, **298**, 2361–2366.
- (15) C. Journet and P. Bernier, English, *Applied Physics A*, 1998, **67**, 1–9.
- (16) L. A. Girifalco, M. Hodak and R. S. Lee, *Phys. Rev. B*, 2000, **62**, 13104–13110.
- (17) A. V. Naumov, S. Ghosh, D. A. Tsyboulski, S. M. Bachilo and R. B. Weisman, *ACS Nano*, 2011, **5**, 1639–1648.
- (18) J.-S. Lauret, C. Voisin, G. Cassabois, C. Delalande, P. Roussignol, O. Jost and L. Capes, *Phys. Rev. Lett.*, 2003, **90**, 057404.
- (19) A. Hagen, M. Steiner, M. B. Raschke, C. Lienau, T. Hertel, H. Qian, A. J. Meixner and A. Hartschuh, *Phys. Rev. Lett.*, 2005, **95**, 197401.
- (20) P. H. Tan, A. G. Rozhin, T. Hasan, P. Hu, V. Scardaci, W. I. Milne and A. C. Ferrari, *Phys. Rev. Lett.*, 2007, **99**, 137402.
- (21) H. Qian, C. Georgi, N. Anderson, A. A. Green, M. C. Hersam, L. Novotny and A. Hartschuh, *Nano Letters*, 2008, **8**, 1363–1367.
- (22) H. Dai, *Accounts of Chemical Research*, 2002, **35**, 1035–1044.
- (23) E. T. Thostenson, Z. Ren and T.-W. Chou, *Composites Science and Technology*, 2001, **61**, 1899–1912.
- (24) C. Journet, W. K. Maser, P. Bernier, A. Loiseau, M. L. de la Chapelle, S. Lefrant, P. Deniard, R. Lee and J. E. Fischer, *Nature*, Aug. 1997, **388**, 756–758.
- (25) T. Guo, P. Nikolaev, A. Thess, D. Colbert and R. Smalley, *Chemical Physics Letters*, 1995, **243**, 49–54.
- (26) A. Thess, R. Lee, P. Nikolaev, H. Dai, P. Petit, J. Robert, C. Xu, Y. H. Lee, S. G. Kim, A. G. Rinzler, D. T. Colbert, G. E. Scuseria, D. Tománek, J. E. Fischer and R. E. Smalley, *Science*, 1996, **273**, 483–487.
- (27) A. Barreiro, C. Kramberger, M. Rümmeli, A. Grüneis, D. Grimm, S. Hampel, T. Gemming, B. Büchner, A. Bachtold and T. Pichler, *Carbon*, 2007, **45**, 55–61.
- (28) Z. F. Ren, Z. P. Huang, J. W. Xu, J. H. Wang, P. Bush, M. P. Siegal and P. N. Provencio, *Science*, 1998, **282**, 1105–1107.

- (29) I. W. Chiang, B. E. Brinson, A. Y. Huang, P. A. Willis, M. J. Bronikowski, J. L. Margrave, R. E. Smalley and R. H. Hauge, *The Journal of Physical Chemistry B*, 2001, **105**, 8297–8301.
- (30) B. Kitiyanan, W. Alvarez, J. Harwell and D. Resasco, *Chemical Physics Letters*, 2000, **317**, 497–503.
- (31) S. Niyogi, M. A. Hamon, H. Hu, B. Zhao, P. Bhowmik, R. Sen, M. E. Itkis and R. C. Haddon, *Accounts of Chemical Research*, 2002, **35**, 1105–1113.
- (32) J. Li, G. Jia, Y. Zhang and Y. Chen, *Chemistry of Materials*, 2006, **18**, 3579–3584.
- (33) Y. Miyata, T. Kawai, Y. Miyamoto, K. Yanagi, Y. Maniwa and H. Kataura, *The Journal of Physical Chemistry C*, 2007, **111**, 9671–9677.
- (34) Y. Miyata, T. Kawai, Y. Miyamoto, K. Yanagi, Y. Maniwa and H. Kataura, *physica status solidi (b)*, 2007, **244**, 4035–4039.
- (35) E. Joselevich, *ChemPhysChem*, 2004, **5**, 619–624.
- (36) P. Singh, S. Campidelli, S. Giordani, D. Bonifazi, A. Bianco and M. Prato, *Chem. Soc. Rev.*, 2009, **38**, 2214–2230.
- (37) S. A. Hodge, M. K. Bayazit, K. S. Coleman and M. S. P. Shaffer, *Chem. Soc. Rev.*, 2012, **41**, 4409–4429.
- (38) D. Tasis, N. Tagmatarchis, A. Bianco and M. Prato, *Chemical Reviews*, 2006, **106**, 1105–1136.
- (39) V. N. Khabashesku, W. E. Billups and J. L. Margrave, *Accounts of Chemical Research*, 2002, **35**, 1087–1095.
- (40) N. Tagmatarchis and M. Prato, *J. Mater. Chem.*, 2004, **14**, 437–439.
- (41) J. Chen, M. A. Hamon, H. Hu, Y. Chen, A. M. Rao, P. C. Eklund and R. C. Haddon, *Science*, 1998, **282**, 95–98.
- (42) M. Holzinger, J. Steinmetz, D. Samaille, M. Glerup, M. Paillet, P. Bernier, L. Ley and R. Graupner, *Carbon*, 2004, **42**, European Materials Research Society 2003, Symposium B: Advanced Multifunctional Nanocarbon Materials and Nanosystems, 941–947.

- (43) Y.-L. Zhao and J. F. Stoddart, *Accounts of Chemical Research*, 2009, **42**, 1161–1171.
- (44) M. S. Strano, V. C. Moore, M. K. Miller, M. J. Allen, E. H. Haroz, C. Kittrell, R. H. Hauge and R. E. Smalley, *Journal of Nanoscience and Nanotechnology*, 2003-02-01T00:00:00, **3**, 81–86.
- (45) L. Vaisman, H. D. Wagner and G. Marom, *Advances in Colloid and Interface Science*, 2006, **128–130**, In Honor of Professor Nissim Garti's 60th Birthday, 37–46.
- (46) Z. Xu, X. Yang and Z. Yang, *Nano Letters*, 2010, **10**, 985–991.
- (47) O. Matarredona, H. Rhoads, Z. Li, J. H. Harwell, L. Balzano and D. E. Resasco, *The Journal of Physical Chemistry B*, 2003, **107**, 13357–13367.
- (48) C. Richard, F. Balavoine, P. Schultz, T. W. Ebbesen and C. Mioskowski, *Science*, 2003, **300**, 775–778.
- (49) P. Angelikopoulos and H. Bock, *The Journal of Physical Chemistry B*, 2008, **112**, 13793–13801.
- (50) P. Angelikopoulos, A. Gromov, A. Leen, O. Nerushev, H. Bock and E. E. B. Campbell, *The Journal of Physical Chemistry C*, 2010, **114**, 2–9.
- (51) S. Utsumi, M. Kanamaru, H. Honda, H. Kanoh, H. Tanaka, T. Ohkubo, H. Sakai, M. Abe and K. Kaneko, *Journal of Colloid and Interface Science*, 2007, **308**, 276–284.
- (52) L. Vaisman, H. D. Wagner and G. Marom, *Advances in Colloid and Interface Science*, 2006, **128–130**, In Honor of Professor Nissim Garti's 60th Birthday, 37–46.
- (53) S. Lin and D. Blankschtein, *The Journal of Physical Chemistry B*, 2010, **114**, 15616–15625.
- (54) S. Ghosh, S. M. Bachilo and R. B. Weisman, *Nat Nano*, June 2010, **5**, 443–450.
- (55) W. Wang, K. A. S. Fernando, Y. Lin, M. J. Meziani, L. M. Veca, L. Cao, P. Zhang, M. M. Kimani and Y.-P. Sun, *Journal of the American Chemical Society*, 2008, **130**, 1415–1419.

- (56) T. Hasobe, S. Fukuzumi and P. V. Kamat, *Journal of the American Chemical Society*, 2005, **127**, 11884–11885.
- (57) G. M. A. Rahman, D. M. Guldi, S. Campidelli and M. Prato, *J. Mater. Chem.*, 2006, **16**, 62–65.
- (58) R. J. Chen, Y. Zhang, D. Wang and H. Dai, *Journal of the American Chemical Society*, 2001, **123**, 3838–3839.
- (59) L. Hu, Y.-L. Zhao, K. Ryu, C. Zhou, J. Stoddart and G. Grüner, *Advanced Materials*, 2008, **20**, 939–946.
- (60) D. M. Guldi, E. Menna, M. Maggini, M. Marcaccio, D. Paolucci, F. Paolucci, S. Campidelli, M. Prato, G. M. A. Rahman and S. Schergna, *Chemistry – A European Journal*, 2006, **12**, 3975–3983.
- (61) C. Ehli, G. M. A. Rahman, N. Jux, D. Balbinot, D. M. Guldi, F. Paolucci, M. Marcaccio, D. Paolucci, M. Melle-Franco, F. Zerbetto, S. Campidelli and M. Prato, *Journal of the American Chemical Society*, 2006, **128**, 11222–11231.
- (62) J. Mohanraj and N. Armaroli, *The Journal of Physical Chemistry Letters*, 2013, **4**, 767–778.
- (63) K. Yanagi, K. Iakoubovskii, H. Matsui, H. Matsuzaki, H. Okamoto, Y. Miyata, Y. Maniwa, S. Kazaoui, N. Minami and H. Kataura, *Journal of the American Chemical Society*, 2007, **129**, 4992–4997.
- (64) Y. Kang and T. A. Taton, *Journal of the American Chemical Society*, 2003, **125**, 5650–5651.
- (65) S. Meuer, L. Braun and R. Zentel, *Macromolecular Chemistry and Physics*, 2009, **210**, 1528–1535.
- (66) H. S. Woo, R. Czerw, S. Webster, D. L. Carroll, J. Ballato, A. E. Strevens, D. O'Brien and W. J. Blau, *Applied Physics Letters*, 2000, **77**, 1393–1395.
- (67) S. A. Curran, P. M. Ajayan, W. J. Blau, D. L. Carroll, J. N. Coleman, A. B. Dalton, A. P. Davey, A. Drury, B. McCarthy, S. Maier and A. Strevens, *Advanced Materials*, 1998, **10**, 1091–1093.
- (68) B. Gigliotti, B. Sakizzie, D. S. Bethune, R. M. Shelby and J. N. Cha, *Nano Letters*, 2006, **6**, 159–164.

- (69) H. Cathcart, S. Quinn, V. Nicolosi, J. M. Kelly, W. J. Blau and J. N. Coleman, *The Journal of Physical Chemistry C*, 2007, **111**, 66–74.
- (70) D. A. Heller, E. S. Jeng, T.-K. Yeung, B. M. Martinez, A. E. Moll, J. B. Gastala and M. S. Strano, *Science*, 2006, **311**, 508–511.
- (71) C. Lee, S. Shin, J. Mun, S.-S. Han, I. So, J.-H. Jeon, T. Kang, S. Kim, P. Whitten, G. Wallace, G. Spinks and S. Kim, *Angewandte Chemie International Edition*, 2009, **48**, 5116–5120.
- (72) M. Zheng, A. Jagota, E. D. Semke, B. A. Diner, R. S. Mclean, S. R. Lustig, R. E. Richardson and N. G. Tassi, *Nat Mater*, May 2003, **2**, 338–342.
- (73) M. Zheng, A. Jagota, M. S. Strano, A. P. Santos, P. Barone, S. G. Chou, B. A. Diner, M. S. Dresselhaus, R. S. Mclean, G. B. Onoa, G. G. Samsonidze, E. D. Semke, M. Usrey and D. J. Walls, *Science*, 2003, **302**, 1545–1548.
- (74) M. S. Arnold, S. I. Stupp and M. C. Hersam, *Nano Letters*, 2005, **5**, 713–718.
- (75) S. Srinivasan, V. Praveen, R. Philip and A. Ajayaghosh, *Angewandte Chemie International Edition*, 2008, **47**, 5750–5754.
- (76) T. Fujigaya and N. Nakashima, *Polym. J*, July 2008, **40**, 577–589.
- (77) O. V. Kharissova, B. I. Kharisov and E. G. de Casas Ortiz, *RSC Adv.*, 2013, **3**, 24812–24852.
- (78) S. Meuer, L. Braun and R. Zentel, *Macromolecular Chemistry and Physics*, 2009, **210**, 1528–1535.
- (79) P. Bilalis, D. Katsigiannopoulos, A. Avgeropoulos and G. Sakellariou, *RSC Adv.*, 2014, **4**, 2911–2934.
- (80) J. Z. Nguendia, W. Zhong, A. Fleury, G. De Grandpré, A. Soldera, R. G. Sabat and J. P. Claverie, *Chemistry – An Asian Journal*, 2014, **9**, 1356–1364.
- (81) J. Cui, W. Wang, Y. You, C. Liu and P. Wang, *Polymer*, 2004, **45**, 8717–8721.
- (82) E. Pavoni, E. Bandini, M. Benaglia, J. K. Molloy, G. Bergamini, P. Ceroni and N. Armaroli, *Polym. Chem.*, 2014, **5**, 6148–6150.

- (83) G. Moad, E. Rizzardo and S. H. Thang, *Australian Journal of Chemistry*, 2005, **58**, 379–410.
- (84) M. Benaglia, A. Alberti, L. Giorgini, F. Magnoni and S. Tozzi, *Polym. Chem.*, 2013, **4**, 124–132.
- (85) J. Chiefari, Y. K. B. Chong, F. Ercole, J. Krstina, J. Jeffery, T. P. T. Le, R. T. A. Mayadunne, G. F. Meijs, C. L. Moad, G. Moad, E. Rizzardo and S. H. Thang, *Macromolecules*, 1998, **31**, 5559–5562.
- (86) A. Llanes-Pallas, C.-A. Palma, L. Piot, A. Belbakra, A. Listorti, M. Prato, P. Samorì, N. Armaroli and D. Bonifazi, *Journal of the American Chemical Society*, 2009, **131**, 509–520.
- (87) M. J. O’Connell, S. M. Bachilo, C. B. Huffman, V. C. Moore, M. S. Strano, E. H. Haroz, K. L. Rialon, P. J. Boul, W. H. Noon, C. Kittrell, J. Ma, R. H. Hauge, R. B. Weisman and R. E. Smalley, *Science*, 2002, **297**, 593–596.
- (88) M. Gubitosi, J. V. Trillo, A. Alfaro Vargas, N. V. Pavel, D. Gazzoli, S. Sennato, A. Jover, F. Meijide and L. Galantini, *The Journal of Physical Chemistry B*, 2014, **118**, 1012–1021.
- (89) S. Nanot, E. H. Hároz, J.-H. Kim, R. H. Hauge and J. Kono, *Advanced Materials*, 2012, **24**, 4977–4994.
- (90) W. Yang, P. Thordarson, J. Gooding, S. Ringer and F. Braet, *Nanotechnology*, 2007, **18**.
- (91) R. H. Baughman, A. A. Zakhidov and W. A. de Heer, *Science*, 2002, **297**, 787–792.
- (92) A. J. Ferguson, J. L. Blackburn and N. Kopidakis, *Materials Letters*, 2013, **90**, 115–125.
- (93) D. Tasis, N. Tagmatarchis, A. Bianco and M. Prato, *Chemical Reviews*, 2006, **106**, 1105–1136.
- (94) C. Wu, J. Wei, D. Tian, Y. Feng, R. H. Miller and Y. Wang, *Journal of Medicinal Chemistry*, 2008, **51**, 6682–6688.
- (95) Z.-K. Chen, H. Meng, Y.-H. Lai and W. Huang, *Macromolecules*, 1999, **32**, 4351–4358.

- (96) D. A. M. Egbe, H. Tillmann, E. Birckner and E. Klemm, *Macromolecular Chemistry and Physics*, 2001, **202**, 2712–2726.
- (97) Z.-K. Chen, H. Meng, Y.-H. Lai and W. Huang, *Macromolecules*, 1999, **32**, 4351–4358.
- (98) B. Wang and M. R. Wasielewski, *Journal of the American Chemical Society*, 1997, **119**, 12–21.
- (99) U. Caruso, M. Casalbani, A. Fort, M. Fusco, B. Panunzi, A. Quatela, A. Roviello and F. Sarcinelli, *Optical Materials*, 2005, **27**, 1800–1810.
- (100) W. Zhang, S. Oya, M.-P. Kung, C. Hou, D. L. Maier and H. F. Kung, *Journal of Medicinal Chemistry*, 2005, **48**, 5980–5988.
- (101) C. Lu, Y. Guo, J. Yan, Z. Luo, H.-B. Luo, M. Yan, L. Huang and X. Li, *Journal of Medicinal Chemistry*, 2013, **56**, 5843–5859.
- (102) C.-H. Andersson and H. Grennberg, *European Journal of Organic Chemistry*, 2009, **2009**, 4421–4428.
- (103) R. B. Weisman and S. M. Bachilo, *Nano Letters*, 2003, **3**, 1235–1238.
- (104) H. Peng, L. B. Alemany, J. L. Margrave and V. N. Khabashesku, *Journal of the American Chemical Society*, 2003, **125**, 15174–15182.
- (105) D. M. Guldi, M. Marcaccio, D. Paolucci, F. Paolucci, N. Tagmatarchis, D. Tasis, E. Vázquez and M. Prato, *Angewandte Chemie International Edition*, 2003, **42**, 4206–4209.
- (106) B. Ballesteros, G. de la Torre, C. Ehli, G. M. Aminur Rahman, F. Agulló-Rueda, D. M. Guldi and T. Torres, *Journal of the American Chemical Society*, 2007, **129**, 5061–5068.
- (107) D. Baskaran, J. W. Mays, X. P. Zhang and M. S. Bratcher, *Journal of the American Chemical Society*, 2005, **127**, 6916–6917.
- (108) M. Granstrom, K. Petritsch, A. C. Arias, A. Lux, M. R. Andersson and R. H. Friend, *Nature*, Sept. 1998, **395**, 257–260.
- (109) J. J. M. Halls, C. A. Walsh, N. C. Greenham, E. A. Marseglia, R. H. Friend, S. C. Moratti and A. B. Holmes, *Nature*, Aug. 1995, **376**, 498–500.
- (110) P. Peumans, S. Uchida and S. R. Forrest, *Nature*, Sept. 2003, **425**, 158–162.

- (111) D. M. Guldi, *The Journal of Physical Chemistry B*, 2005, **109**, 11432–11441.
- (112) J. Peet, J. Y. Kim, N. E. Coates, W. L. Ma, D. Moses, A. J. Heeger and G. C. Bazan, *Nat Mater*, July 2007, **6**, 497–500.
- (113) C. N. Hoth, P. Schilinsky, S. A. Choulis and C. J. Brabec, *Nano Letters*, 2008, **8**, 2806–2813.
- (114) K. Vandewal, K. Tvingstedt, A. Gadisa, O. Inganäs and J. V. Manca, *Nat Mater*, Nov. 2009, **8**, 904–909.
- (115) A. K. Burrell, D. L. Officer, P. G. Plieger and D. C. W. Reid, *Chemical Reviews*, 2001, **101**, 2751–2796.
- (116) J. S. Lindsey and R. W. Wagner, *The Journal of Organic Chemistry*, 1989, **54**, 828–836.
- (117) M. Maggini, G. Scorrano and M. Prato, *Journal of the American Chemical Society*, 1993, **115**, 9798–9799.
- (118) S. Giordani, J.-F. Colomer, F. Cattaruzza, J. Alfonsi, M. Meneghetti, M. Prato and D. Bonifazi, *Carbon*, 2009, **47**, 578–588.
- (119) F. Wilkinson, P. W. Helman and A. B. Ross, *J. Phys. Chem. Ref. Data*, 1993, **22**, 113–262.
- (120) J. L. Bahr, D. Kuciauskas, P. A. Liddell, A. L. Moore, T. A. Moore and D. Gust, *Photochemistry and Photobiology*, 2000, **72**, 598–611.
- (121) D. Kuciauskas, S. Lin, G. R. Seely, A. L. Moore, T. A. Moore, D. Gust, T. Drovetskaya, C. A. Reed and P. D. W. Boyd, *The Journal of Physical Chemistry*, 1996, **100**, 15926–15932.
- (122) F. Monti, U. Hahn, E. Pavoni, B. Delavaux-Nicot, J.-F. Nierengarten and N. Armaroli, *Polyhedron*, 2014, **82**, Molecular Materials for Solar Energy Conversion, 122–131.
- (123) P. G. Sammes and G. Yahiolu, *Chem. Soc. Rev.*, 1994, **23**, 327–334.
- (124) G. Accorsi, A. Listorti, K. Yoosaf and N. Armaroli, *Chem. Soc. Rev.*, 2009, **38**, 1690–1700.
- (125) R. Faust and S. Ott, *J. Chem. Soc., Dalton Trans.*, 2002, 1946–1953.

- (126) A. E. Friedman, J. C. Chambron, J. P. Sauvage, N. J. Turro and J. K. Barton, *Journal of the American Chemical Society*, 1990, **112**, 4960–4962.
- (127) C. Goze, C. Leiggener, S.-X. Liu, L. Sanguinet, E. Levillain, A. Hauser and S. Decurtins, *ChemPhysChem*, 2007, **8**, 1504–1512.
- (128) M.-J. Kim, R. Konduri, H. Ye, F. M. MacDonnell, F. Puntoriero, S. Serroni, S. Campagna, T. Holder, G. Kinsel and K. Rajeshwar, *Inorganic Chemistry*, 2002, **41**, 2471–2476.
- (129) Y. Sun, L. E. Joyce, N. M. Dickson and C. Turro, *Chem. Commun.*, 2010, **46**, 2426–2428.
- (130) Q.-X. Zhou, W.-H. Lei, J.-R. Chen, C. Li, Y.-J. Hou, X.-S. Wang and B.-W. Zhang, *Chemistry – A European Journal*, 2010, **16**, 3157–3165.
- (131) S. L. H. Higgins, T. A. White, B. S. J. Winkel and K. J. Brewer, *Inorganic Chemistry*, 2011, **50**, 463–470.
- (132) A. J. McConnell, M. H. Lim, E. D. Olmon, H. Song, E. E. Dervan and J. K. Barton, *Inorganic Chemistry*, 2012, **51**, 12511–12520.
- (133) D. Jain, A. Saha and A. A. Marti, *Chem. Commun.*, 2011, **47**, 2246–2248.
- (134) B. R. Spencer, B. J. Kraft, C. G. Hughes, M. Pink and J. M. Zaleski, *Inorganic Chemistry*, 2010, **49**, 11333–11345.
- (135) B. D. Lindner, J. U. Engelhart, M. Märken, O. Tverskoy, A. L. Appleton, F. Rominger, K. I. Hardcastle, M. Enders and U. H. F. Bunz, *Chemistry – A European Journal*, 2012, **18**, 4627–4633.
- (136) S. Miao, S. M. Brombosz, P. v. R. Schleyer, J. I. Wu, S. Barlow, S. R. Marder, K. I. Hardcastle and U. H. F. Bunz, *Journal of the American Chemical Society*, 2008, **130**, 7339–7344.
- (137) E. Dulière, M. Devillers and J. Marchand-Brynaert, *Organometallics*, 2003, **22**, 804–811.
- (138) A. Juris, V. Balzani, F. Barigelletti, S. Campagna, P. Belser and A. von Zelewsky, *Coordination Chemistry Reviews*, 1988, **84**, 85–277.
- (139) R. Parr and Y. Weitao, *Oxford University Press*, 1989, **Oxford, U.K.**

- 
- (140) S. Campagna, F. Puntoriero, F. Nastasi, G. Bergamini and V. Balzani, English, in *Photochemistry and Photophysics of Coordination Compounds I*, ed. V. Balzani and S. Campagna, Springer Berlin Heidelberg, 2007, vol. 280, pp. 117–214.
- (141) E. C. Constable, M. Neuburger, P. Rösel, G. E. Schneider, J. A. Zampese, C. E. Housecroft, F. Monti, N. Armaroli, R. D. Costa and E. Ortí, *Inorganic Chemistry*, 2013, **52**, 885–897.
- (142) G. Pourtois, D. Beljonne, C. Moucheron, S. Schumm, A. Kirsch-De Mesmaeker, R. Lazzaroni and J.-L. Brédas, *Journal of the American Chemical Society*, 2004, **126**, 683–692.
- (143) Q. Zhou, W. Lei, Y. Chen, C. Li, Y. Hou, B. Zhang and X. Wang, *Chemistry – A European Journal*, 2012, **18**, 8617–8621.
- (144) G. A. Crosby and J. N. Demas, *The Journal of Physical Chemistry*, 1971, **75**, 991–1024.



# Acknowledgement

This thesis is based on few experimental results obtained within the project FIRB “SUPRACARBON” SUPRAMolecularly Templated Synthesis of Homochiral CARBON Nanotubes for Photovoltaic Devices (contract number: RBFR10DAK6). My sincere thanks to all the partners of the project for their synchronized and efficient collaboration.

“**E. Pavoni**, E. Bandini, M. Benaglia, J. K. Molloy, G. Bergamini, P. Ceroni and N. Armaroli “*A tailored RAFT copolymer for the dispersion of single walled carbon nanotubes in aqueous media*”, *Polym. Chem.*, 2014, 5, 6148-6150.” Reproduced by permission of The Royal Society of Chemistry

Thanks to Elsevier for “F. Monti, U. Hahn, **E. Pavoni**, B. Delavaux-Nicot, J.-F. Nierengarten and N. Armaroli, “*Homoleptic and heteroleptic Ru(II) complexes with extended phenanthroline-based ligands*”, *Polyhedron*, 2014, 82, 122-131, Special Issue on Molecular Materials for Solar Energy Conversion”.

A deep gratitude to my supervisors Nicola Armaroli and Paola Ceroni and to all my colleagues. Thanks for tutoring me in this years and for the patience shown.



# List of publications and Posters presentation

## Publication:

- **E. Pavoni**, E. Bandini, M. Benaglia, J. K. Molloy, G. Bergamini, P. Ceroni and N. Armaroli “*A tailored RAFT copolymer for the dispersion of single walled carbon nanotubes in aqueous media*”, *Polym. Chem.*, 2014, 5, 6148-6150.
- F. Monti, U. Hahn, **E. Pavoni**, B. Delavaux-Nicot, J.-F. Nierengarten and N. Armaroli, “*Homoleptic and heteroleptic Ru(II) complexes with extended phenanthroline-based ligands*”, *Polyhedron*, 2014, 82, 122-131, Special Issue on Molecular Materials for Solar Energy Conversion.
- F. Monti, **E. Pavoni**, N. Armaroli “*Nanomaterials for Lighting and Solar Energy Conversion*”, NATO Science for Peace and Security Series B: Physics and Biophysics. “*Nano-Structures for Optics and Photonics*”, B. Di Bartolo, J. Collins, L. Silvestri (Eds.), *Springer* (Berlin), 2015, 373-414.

## Poster presentation:

- **E. Pavoni**, E. Bandini, M. Benaglia, J. K. Molloy, G. Bergamini, P. Ceroni and N. Armaroli “*Physical Modification of SWCNTs using an Amphiphilic RAFT Copolymer*”, **Italian Photochemistry Meeting 2014**, Universit di Milano, November 27 – 29<sup>th</sup> 2014.
- **E. Pavoni**, F. Monti, U. Hahn, B. Delavaux-Nicot, J.-F. Nierengarten and N. Armaroli, “*Homoleptic and heteroleptic Ru(II) complexes with extended phenanthroline-based ligands*”, 15<sup>th</sup> **IUPAC Symposium on Photochemistry**, CNRS Bordeaux (FR), July 13 – 18<sup>th</sup> 2014.
- **E. Pavoni**, E. Bandini, M. Benaglia, J. K. Molloy, G. Bergamini, P. Ceroni and N. Armaroli “*SWCNTs Dispersion via Amphiphilic Polymer*”, **National Supramolecular Chemistry Congress**, Universit di Padova, September 24 – 27<sup>th</sup> 2013